UNIVERSIDAD DE CHILE
FACULTAD DE CIENCIAS FÍSICAS Y MATEMÁTICAS
DEPARTAMENTO DE ASTRONOMÍA

THE Hα LUMINOSITY FUNCTION OF GALAXIES AT $z \sim 4.5$

TESIS PARA OPTAR AL GRADO DE
MAGÍSTER EN CIENCIAS, MENCIÓN ASTRONOMÍA

MARÍA VICTORIA BOLLO DOIZI

PROFESOR GUÍA:
VALENTINO GONZÁLEZ CORVALÁN

MIEMBROS DE LA COMISIÓN:
SEBASTIÁN LÓPEZ MORALES
MÓNICA RUBIO LÓPEZ
MAURO STEFANON

SANTIAGO DE CHILE
2022

RESUMEN DE LA TESIS PARA OPTAR AL GRADO DE
MAGÍSTER EN CIENCIAS, MENCIÓN ASTRONOMÍA
POR: MARÍA VICTORIA BOLLO DOIZI
FECHA: 2022
PROF. GUÍA: VALENTINO GONZÁLEZ CORVALÁN

LA FUNCIÓN DE LUMINOSIDAD DE Hα EN GALAXIAS A $z \sim 4.5$

La Función de Luminosidad (LF) es un observable fundamental para estudiar galaxias; además, elegir un trazador de luminosidad que se correlacione fuertemente con la Tasa de Formación Estelar (SFR) es crucial para estudiar la evolución de la formación estelar. Por lo tanto, la relación entre la luminosidad y la SFR debe ser lo más directa y precisa posible. La luminosidad Utravioleta (UV) traza directamente la SFR, pero es muy sensible al polvo, cuyas correcciones son grandes e inciertas. Una mejor alternativa es usar líneas de emisión de Hα a 6563Å, que es uno de los estimadores más utilizados de SFR en galaxias hasta $z \lesssim 3$. Sin embargo, espectroscopía de la emisión de Hα en galaxias a alto redshift ($z \gtrsim 4$) solo estará disponible con los primeros datos del telescopio espacial James Webb (JWST).

A pesar de las dificultades observacionales, se puede utilizar un método indirecto basado en fotometría profunda de Spitzer/IRAC para estimar el flujo de Hα a $z > 3$. En redshifts específicos, Hα contribuye al flujo medido en la banda [3.6] de IRAC, mientras que las otras bandas miden estrictamente el continuo. Este desplazamiento de color se utiliza para estimar el flujo de Hα. Sin embargo, aunque este método se ha utilizado durante casi una década, aún no existe un estudio sistemático de la función de luminosidad de Hα a alto redshift ($z \sim 4.5$).

Esta tesis presenta la función de luminosidad de Hα (Hα LF) derivada de una gran muestra de Lyman Break Galaxies a $z \sim 4.5$. Se utilizan las imágenes más profundas obtenidas hasta la fecha de Spitzer/IRAC en las bandas [3.6] y [4.5] del programa GOODS Re-ionization Era wide-Area Treasury from Spitzer (GREATS). El flujo de Hα se deriva de la diferencia entre el flujo del continuo, estimado del mejor ajuste de la distribución espectral de energía (SED), y la fotometría observada en IRAC [3.6]. Además, se estudia la evolución de la Hα LF obteniendo las mejores restricciones de esta propiedad a alto redshift.

Los resultados indican que las SFRs derivadas de Hα son mayores las de la luminosidad UV para galaxias con baja SFR, pero ocurre lo contrario para las altas SFRs. Esto podría explicarse porque las galaxias de baja masa (también baja SFR) tienen, en promedio, historias de formación estelar (SFHs) ascendentes, mientras que para las de alta masa, las SFHs pueden estar disminuyendo. También podría explicarse por las diferentes escalas de tiempo en que Hα y el UV trazan la SFR. La función de SFR es más pronunciada a mayor redshift y la densidad de la SFR estimada a partir de Hα es mayor que la estimada de la luminosidad UV. Comparando con trabajos previos, las parametrizaciones de la función de Schechter para la Hα LF muestran que a mayor redshift el factor de normalización Φ^* decrece, que la luminosidad característica L^* se hace más brillante, y que no hay evolución significativa en la pendiente del extremo de bajas luminosidades α.

RESUMEN DE LA TESIS PARA OPTAR AL GRADO DE
MAGÍSTER EN CIENCIAS, MENCIÓN ASTRONOMÍA
POR: MARÍA VICTORIA BOLLO DOIZI
FECHA: 2022
PROF. GUÍA: VALENTINO GONZÁLEZ CORVALÁN

THE Hα LUMINOSITY FUNCTION OF GALAXIES AT $z \sim 4.5$

The Luminosity Function (LF) is one of the most fundamental observables to study galaxies; moreover, choosing a luminosity tracer that strongly correlates with the Star Formation Rate (SFR) allows us to study the evolution of star formation across cosmic time. Thus, the relationship between luminosity and SFR must be as direct and reliable as possible. The UV luminosity is a direct tracer of SFR but it is very sensitive to dust, so corrections are large and uncertain. A better alternative is to use the rest-frame optical Hα emission line at 6563 Å, which is one of the most used SFR estimators up to $z \lesssim 3$. However, Hα emission spectroscopy at high redshift ($z \gtrsim 4$) will only be available with the first data from the James Webb Space Telescope (JWST).

Despite the existing observational difficulties, it is possible to use an indirect method based on deep *Spitzer*/IRAC near-infrared photometry to determine the Hα flux at $z > 3$. The redshifted Hα emission contributes to the flux measured in one of the IRAC bands at specific redshifts, while the other bands sample strictly the stellar continuum. This color offset can be used to estimate the flux of the Hα line. However, even though this method has been used for almost a decade, a systematic study of the Hα luminosity function at high redshift ($z \sim 4.5$) is still lacking.

In this thesis, we present the Hα Luminosity Function (Hα LF) derived from a large sample of Lyman Break Galaxies at $z \sim 4.5$. This study makes use of the deepest *Spitzer*/IRAC [3.6] and [4.5] imaging to date from the GOODS Re-ionization Era wide-Area Treasury from Spitzer (GREATS) program, reaching up to 250 hrs of integration. The Hα flux is derived from the offset between the continuum flux estimated from the best-fit Spectral Energy Distribution (SED), and the observed photometry in IRAC [3.6]. Moreover, we study the evolution of the Hα LF providing the best constraints at high redshift.

We find that SFRs derived from Hα are higher than those derived from rest-frame UV for low SFR galaxies but the opposite happens for the highest SFRs. This could be explained by lower mass galaxies (also lower SFR) having, on average, rising star formation histories (SFHs), while at the highest masses the SFHs may be declining. It could also be explained by the different timescales of SFR that Hα and UV luminosities trace. The SFR function is steeper and the star formation rate density estimated from Hα is higher than the previous estimates based on UV luminosities. Compared with previous works at lower redshifts, the Schechter parameterizations of the Hα LF show a decreasing normalization factor Φ^* with redshift, the characteristic luminosity L^* becoming brighter at higher redshifts, and no significant evolution in the faint-end slope α at high-z.

A mi gran Luz.

Y a través de ella,
a todas las grandes mujeres
que me preceden.

"We have a hunger of the mind
which asks for knowledge of all around us,
and the more we gain, the more is our desire;
the more we see, the more we are capable of seeing."

– Maria Mitchell

Agradecimientos

Culmina un proceso profundamente significativo y mi corazón desborda gratitud. Quiero agradecer a todas las personas que han contribuido a que este arduo camino fuese mucho más ameno. A mi mamá, por apoyarme siempre para cumplir mis sueños, aunque dudara de mi decisión de ser astrónoma, siempre confió en que lo lograría. Gracias por su inmenso amor, por hacer todo lo posible por protegerme, por ser un ejemplo de fortaleza y perseverancia ante toda adversidad. A mi hermana Andrea, por su cariño y empatía, por facilitarme apoyo emocional y alegrarse genuinamente de mis triunfos. Gracias por escucharme, por contenerme, y estar pendiente de mis necesidades. A mi hermano Mariano, por su apoyo, por sus detalles y gestos de cariño cuando me comparte dulces, por tantas risas que hemos compartido. Agradezco nuestra complicidad y buena voluntad para ayudarnos siempre que podemos. A todas las energías que me cuidan y protegen desde el más allá, en especial a mi papá y a mi abuela. A mi madrina y su familia, por su preocupación, su apoyo y por alegrarse de mis logros. A mi familia extendida, por prestarme apoyo cuando lo he necesitado. A Francesca, por tantos aprendizajes juntas, por su alegría, por su dulzura, por contenerme en momentos de frustración, por su cariño, su apoyo, y su auténtico entusiasmo al verme alcanzar mis metas. A Alex, por su honesta y verdadera amistad, por escucharme, por estar pendiente de mí y ser un profundo apoyo motivacional. A Stefano, por su cariñosa amistad, por su compañía en largos días de estudio, por apoyarme, y por traer música alegre a mi vida con sus canciones e instrumentos.

Agradezco a todos los profesores que me han acompañado en este proceso. A la profesora Mónica Rubio, mi primera profesora guía en pregrado. Gracias por su apoyo, sus consejos, su confianza, y por ser una gran inspiración. Al profesor Valentino González, mi profesor guía durante el magíster. Agradezco su buena voluntad para enseñarme y alentarme a ser una investigadora independiente, por su confianza en mi trabajo, su gran apoyo y sus buenos consejos. A todos los miembros del comité, cuyos comentarios me permitieron llegar a una mejor versión de mi tesis, gracias por su tiempo y dedicación. A todos los estudiantes que he tenido la oportunidad de apoyar, en especial a quienes conocí por el programa TIP. Agradezco estas instancias de docencia por la satisfacción que me produce enseñar.

Me siento profundamente agradecida de los múltiples aprendizajes y experiencias. Agradezco haber tenido la oportunidad de conocerme a mí misma, de reafirmar mis objetivos, y tener la voluntad de salir adelante ante la frustración. Es un nuevo punto de inflexión y espero seguir cultivando esta pasión por aprender.

Table of Content

1. Introduction **1**
- 1.1. Motivation . . . 1
- 1.2. The Luminosity Function . . . 3
- 1.3. High-redshift Galaxies . . . 7
- 1.4. Star Formation Rate tracers . . . 10
- 1.5. This work . . . 13

2. Data **15**
- 2.1. Sample Selection and HST data . . . 15
- 2.2. GREATS Spitzer/IRAC Photometry . . . 16

3. The sample for Hα measurements at $z \sim 4.5$ **18**
- 3.1. IRAC Photometry . . . 18
- 3.2. Redshifts . . . 18
  - 3.2.1. Spectroscopic Sample . . . 19
  - 3.2.2. Photometric Redshift Sample . . . 20
  - 3.2.3. Spectroscopic Sample vs. Photometric Sample . . . 20

4. Hα measurements **22**
- 4.1. Spectral Energy Distribution Modeling . . . 22
- 4.2. Hα flux measurements . . . 23
- 4.3. Detection Limit . . . 25
- 4.4. Alternative Hα measurements . . . 26
  - 4.4.1. Modeling the Nebular Emission with CIGALE . . . 29

5. The Hα Luminosity Function **30**
- 5.1. The Faint-end of the Hα Luminosity Function . . . 34
- 5.2. Schechter Parameters . . . 34

6. Star Formation Rate Functions **38**
- 6.1. Dust Corrections . . . 38
- 6.2. Star Formation Rates . . . 39
- 6.3. Star Formation Rate Function at $z \sim 4.5$ . . . 40

6.4. The SFRD evolution 43

7. Discussion **46**

7.1. Evolution of the Hα Equivalent Width 46

7.2. Evolution of the Hα Luminosity Function 47

7.3. Differences between SFR(Hα) and SFR(UV) 50

7.4. Cosmic Star Formation Rate Density History 52

8. Summary and Conclusions **55**

Bibliography **57**

Table Index

3.1. Summary of Sample Selection for Hα measurements 20
5.1. Correction factors $f_q \times f_z$ per field [a] 33
5.2. Values of the Hα LF at $z \sim 4.5$ 35
5.3. Schechter parameters of the Hα LF 35
6.1. Values of the SFR Function at $z \sim 4.5$ 41
6.2. Schechter parameters of the SFR Function 45

Figure Index

1.1. The Cosmic Star Formation Rate Density evolution extracted from Madau & Dickinson (2014) (Figure 9 of their article). They compiled FUV+IR rest-frame measurements (see references in their article). The solid curve is the best-fit to the data. 2

1.2. The UV Luminosity function extracted from Bouwens et al. (2021). The stepwise determinations are shown as solid circles in different colors for each redshift range. The best-fit Schechter LFs are shown with solid lines in the same color code of its corresponding redshift range. 5

1.3. The evolution of the Schechter parameters from the best-fits presented in Figure 1.2, extracted from Bouwens et al. (2021). The evolution of the faint-end slope α, the characteristic luminosity M^*, and the normalization ϕ^* with redshift in the top, middle and bottom panels, respectively. For all panels the solid red circles are from Bouwens et al. (2021) and Oesch et al. (2018b). The compilation of the measurements also includes estimations at $z \sim 0.055$ from Wyder et al. (2005), at $z \sim 0.2 - 0.1$ from Arnouts et al. (2005), and the ranges $z = 0.3 - 0.45$, $z = 0.6 - 0.9$, $z = 0.9 - 1.3$, and $z = 1.3 - 1.8$ from Moutard et al. (2020). The light and dark red contours show their 68% and 95% constraints on the evolution of the faint-end slope α, M^*, and $\log_{10}\phi^*$ inferred from the fit to their LF results. 6

1.4. Extracted from Dickinson (1998), illustrates the Lyman Break Technique applied in the Hubble Deep Field (HDF). *Top*: model spectrum of a star forming galaxy observed at $z = 3$. The roughly flat continuum is truncated at 912Å limit, which is redshifted between the U and B filters (transmission curves are shown below the spectrum). The effects of intergalactic neutral hydrogen further suppress the continuum in the $U-$ and $B-$bands. *Bottom*: Imaging of an HDF galaxy in the 4 filters. It is visible in the $I-$, $V-$, and $B-$bands, but it vanishes in the $U-$band image. This galaxy has been spectroscopically confirmed to have $z = 2.8$. 9

1.5. *Left*: Extracted from Stark et al. (2013), shows the bands in which Hα and other emission lines can be detected as a function of redshift. The Hα emission line can be isolated and detected at $3.8 \lesssim z \lesssim 5$. *Right*: Broad-band *HST*+IRAC photometry in black points and the estimated spectral energy distribution of the continuum in the light blue line. The redshifted wavelength of Hα is shown with the vertical dotted line, which falls in the measurement range of the IRAC [3.6] band, whose wavelength coverage is shown by the shaded area and reference filter transmission curves are shown at the bottom. The observed photometry in IRAC [3.6] seems to be boosted by the presence of the Hα emission line, while the other bands sample strictly the stellar continuum. 12

2.1. Demonstration of how to overcome the confusion limit in IRAC photometry, extracted from Labbé et al. (2015), the black dashed aperture shows the location where the flux is to be measured in all panels. *Top left*: shows the IRAC 3.6 μm mosaic along with the 2.5σ isophote above the background as red contours, implying that the point spread function (PSF) wings contaminate $\sim 70\%$ of the background. *Top right*: Deep *HST*/WFC3 imaging of the same position on the sky. *Bottom left*: The model constructed after the convolution of each WFC3 detected source to approximate a high quality IRAC PSF to account for the PSF wings. *Bottom right*: The residual image after modeling and subtraction shows that source confusion is impressively reduced. 17

3.1. Comparison between the redshift selected samples at $3.86 < z < 4.94$ (blue histogram) and the parent sample of $B-$ and $V-$dropouts (black histogram). The selected sample includes $B-$ and $V-$ drop, according to their lack of brightness in the B_{435} and V_{606} bands, respectively, and the redshifted Hα emission falls in the measurement range of the 3.6μm band. The median redshift of the sample is $z \sim 4.3$, taking into account the spec$-z$ and photo$-z$ sample. The selection criteria that assess the quality of data are the same in both samples (see Chapter 3) related to reliable IRAC photometry (e.g., cuts based on IRAC S/N, quality of the SED fit) and accurate redshifts. 19

3.2. Comparison of the observational properties of our photo$-z$ sample (filled blue histograms) and our spec$-z$ sample (purple histograms) for the redshift selected sample at $z \sim 4.5$, both samples are normalized to the total number of objects in each category, so the integral of the area under the curve is 1. *Top left:* the UV-continuum slope β, defined as $f_\lambda \propto \lambda^\beta$, shows a similar distribution in both samples, with a median of -1.94 ($\sigma = 0.38$) for the photo$-z$ sample, and -1.92 ($\sigma = 0.36$) for the spec$-z$ sample. *Top right:* The redshift distribution of the two samples show differences, the median value of the spec$-z$ sample of 4.15 ($\sigma = 0.31$) is slightly less than the median value 4.30 ($\sigma = 0.19$) of the photo$-z$ sample. *Bottom left:* The $H_{160} - [4.5]$ color show a median value of 0.36 ($\sigma = 0.55$) for the photo$-z$ sample, and 0.25 ($\sigma = 0.66$) for the spec$-z$ sample. *Bottom right:* The distribution of stellar masses for the photo$-z$ and spec$-z$, with median values of 8.86 dex ($\sigma = 0.48$) and 8.95 dex ($\sigma = 0.48$) in $\log_{10} M_\star/M_\odot$, respectively. Despite these differences, there does not seem to be any significant bias between both the photometric and spectroscopic samples at $z \sim 4.5$. 21

4.1. Broadband *HST*+IRAC photometry with their respective best-fit stellar population models for 2 sources in our sample. In each panel, the broadband observations are shown with filled symbols, except for the IRAC [3.6] band that is ignored in the fit to avoid the possible nebular contribution, which is an open symbol. Downward pointing arrows are 2σ upper limits. The top panel is a source with known spectroscopic redshift and the bottom panel is an example from the photometric sample. The redshifted wavelength of Hα is shown with the vertical dotted line, which falls in the range of the [3.6] IRAC band, whose wavelength range is shown by the shaded area (reference filter transmission curves are shown at the bottom of each panel). These two cases show a clear excess in the observed photometry compared to the underlying continuum of the best-fit model. This excess is primarily due to the contribution of the Hα line to the observed flux. 24

4.2. Hα rest-frame equivalent width distribution for the sample at $z \sim 4.5$ (blue shaded histogram) normalized to the total number of sources in the sample, so the integral of the area under the curve is 1. A 6% of the sample corresponds to negative values. Among the positive values with $S/N > 1$, the mean value is 388 Å (shown by the dotted vertical line). 26

4.3. *Left*: The SED of a galaxy in the redshift range $3.0 < z < 3.7$ where no contribution of the Hα emission line is expected to be measured in the IRAC [3.6] band. The magenta point illustrates the estimation of the predictive model proposed and the gray transparent curve shows the level of the continuum estimated by CIGALE. The predictive model consistently estimates the flux measured at [3.6] as well as the continuum level estimated by CIGALE at that wavelengths. *Right*: The SED of a galaxy in the sample at $3.86 < z < 4.94$ is shown for comparison, where the [3.6] is affected by the presence of the Hα emission. After training the model, the continuum is estimated on this sample, obtaining the magenta point, then this offset allows us to measure Hα almost independently of the SED fitting. 27

4.4. Hα fluxes derived from the predictive model vs. the fiducial estimates used throughout, based on the offset between the observed photometry and the best-fit SED. Blue points have 2σ significance, and the rest of the gray points have less than 2σ significance, but they still follow the same trend as the other points. Both methods are consistent on average, with a scatter of 0.13 dex (see text) that is comparable to the typical uncertainties. This shows that the Hα flux estimates used throughout do not depend strongly on the details of the SED fitting procedure. 28

4.5. Comparison between our fiducial Hα fluxes and the ones derived from SED modeling with CIGALE including nebular emission. Color code represents the value of χ^2 in the [3.6] band from where we estimate the Hα flux. This quantity reveals how well the best-fit model reproduces actual photometry in each band. 29

5.1. UV Luminosity function for the selected sample at $3.96 < z < 4.94$ with 1299 objects (blue filled points), corresponding to the UV LF recovered after adjusting correction factors for the given volume. The solid gray line is the original UV LF at $z \sim 4$ with 5712 sources, and the solid green line is the original curve at $z \sim 5$ that contains 1862 sources from Bouwens et al. (2015). 31

5.2. Hα Luminosity Function for the sample at $z \sim 4.5$ represented with blue points. The vertical dashed line show the detection limit derived as explained Section 4.3. It can be noticed that below the detection limit the Hα LF decreases due to the incompleteness of the measurements in the faint end. We correct this incompleteness in Section 5.1. 32

5.3. *Top*: The relationship between Hα Luminosity and $M_{\rm UV}$. Black points (measurements) and blue symbols with arrows (2σ upper limits) are used to fit a Bayesian linear regression. The outliers and the intrinsic scatter were also considered in the modeling. The red line corresponds to the maximum a posteriori and the shaded region represents the intrinsic scatter. *Bottom*: The Hα LF derived from the V_{max} method (blue points), from the Monte Carlo (MC) empirical sampling (blue histogram), and from the analytical derivation of the faint-end slope using the linear regression described above (magenta solid line). The detection limit is shown by the vertical dashed line. 36

5.4. Hα LF found for the sample at $z \sim 4.5$, derived from dust-corrected luminosities (see Section 6.1 for further details about dust corrections). Schechter parameterization of the data with the α parameter fixed is done. The parameters Φ^* and L^* are allowed to vary and are shown in Table 5.3. 37
6.1. Hα luminosities dust-corrected using CIGALE best fit model compared to the fiducial Hα luminosities used throughout which are based on the (Meurer et al. 1999a) relation. CIGALE-based corrections result in Hα luminosities on average 1.3× higher. 40
6.2. Star formation rate derived from the Hα luminosity in the y axis vs. those derived from UV luminosity in the x axis. Both luminosities were dust-corrected using the Calzetti et al. (2000) attenuation law and the IRX-β relation (Meurer et al. 1999b). The dashed black line is the one-to-one relation, and the blue solid line shows the Bayesian linear regression (including possible outliers) and intrinsic scatter (equation shown in the bottom right). 41
6.3. Star Formation Rate function at $z \sim 4.5$ derived following the procedure described in Section 6.3. The SFR function is based on Hα luminosity function and we assume Kennicutt (1998a) conversion from Hα to SFR with a correction for a Chabrier (2003) IMF. It was calculated from the stepwise dust-corrected SFR function with the analytical solution for the Schechter function (Smit et al. 2012). Schechter function was fitted with the least-square method considering the errors associated with each measurement and with a fixed value of the faint-end slope derived from the Hα Luminosity Function. Also, the SFR function derived from the UV at $z \sim 4$ by Smit et al. (2016) is shown as reference. . . . 42
6.4. The 68% and 95% confidence intervals on the Schechter parameters Φ^* and SFR^* we derive for the SFR function at $z \sim 4.5$. As the faint-end slope α was fixed, it is not possible to build the contours with the other parameters. 43
6.5. Cosmic evolution of the star formation rate density (SFRD). Our Hα-based estimate at $z \sim 4.5$ is shown by the solid blue circle. For comparison, we also show rest-UV based estimates for our sample (open circles). For context, we show $z \lesssim 2.5$, Hα-based SFRD estimates by Sobral et al. (2013) ($z = 0.08, 0.4, 0.84, 1.47, 2.23$). At $z > 2.5$ there are mainly UV-based SFRDs so here we show estimates from Bouwens et al. (2015) at $z = 3.8, 4.9, 5.9, 6.8, 7.9$. Also Asada et al. (2021) present estimations based on the rest UV to optical using SED fitting at $z \sim 4.5$, and at $z \sim 7.8$ Asada & Ohta (2022) measure the SFRD from the Hα luminosity function. All SFRD estimates are made considering galaxies brighter than $M_{\rm UV} = -17$, except for the case of Sobral et al. (2013) the integration is consistent with $M_{\rm UV} = -18$. The figure also shows the functional fit for the cosmic evolution of the SFRD reported by Madau & Dickinson (2014) converted into the Chabrier IMF, which is primarily based on UV and IR estimates (gray solid line). Our fit to the Hα-based SFRD estimates is shown in red. 44

7.1. Evolution of EW(Hα) with redshift. The filled blue point represents our median EW(Hα) measurements for the sample at $z \sim 4.5$. Results from other Hα studies are shown for comparison (Fumagalli et al. 2012, Mármol-Queraltó et al. 2016, Rasappu et al. 2016, Shim et al. 2011, Smit et al. 2016, Sobral et al. 2013, Stark et al. 2013, Stefanon et al. 2022). The dotted lines show the evolution of this quantity proposed by Fumagalli et al. (2012), for the stellar masses range given by $10^{10-10.5}$ and $S/N > 3$ data of their work (light blue curve), and by Mármol-Queraltó et al. (2016) (red curve). 47
7.2. Our Hα LF (Schechter fits) at $z \sim 4.5$ compared to the Hα LF by Sobral et al. (2013) at $z \sim 2.2$. The Hα LF at $z = 0.2$ presented by Stroe & Sobral (2015) is shown as a representative reference of the local universe. There is a clear evolution of the normalization factor of the LF, also the "knee" of the function changes according to redshift, and the faint-end slope does not show a clear evolution. 48
7.3. The evolution of the Schechter best-fit parameters for the Hα LF since $z \sim 4.5$. Top panel: the evolution of Φ^* shows a decrease with redshift from $z \sim 1$. Middle panel: the evolution of $L^*_{\mathrm{H}\alpha}$ shows a consistent increase up to $z \sim 4.5$. Bottom panel: the faint-end slope shows a fairly flat behavior as a function of redshift. 49
7.4. Star formation rate derived from the Hα luminosity vs. those derived from UV luminosity. Color coded by the range of stellar mass indicated in the legend. The dashed black line is the one-to-one relation, and the blue solid line shows the Bayesian linear regression (including possible outliers) and intrinsic scatter (equation shown in the bottom right). This figure is the same as the Figure6.2 but color coded by ranges of stellar mass 51
7.5. Cosmic evolution of the Star Formation Rate Density (SFRD) with the luminosities corrected by dust from the extinction derived by CIGALE instead of the fiducial result presented previously, based on the (Meurer et al. 1999a) relation. This is equivalent to Figure 6.5 but with the alternative dust corrections. The final result does not depend strongly on the choice between these two dust corrections. 54

Chapter 1

Introduction

1.1. Motivation

Estimating the star formation rate (SFR) of galaxies is key to understanding their formation and evolution across cosmic time. Thanks to the latest imaging and spectroscopic surveys, this field has seen great progress, extending the study of galaxy evolution all the way to $z \sim 11$, when the Universe was only ~ 400 Myr old (Bouwens et al. 2015, 2016, Brammer et al. 2012, Eyles et al. 2005, Finkelstein et al. 2012, González et al. 2012, 2010, Grogin et al. 2011, Hasinger et al. 2018, Jiang et al. 2021, Kashikawa et al. 2011, Koekemoer et al. 2011, Kriek et al. 2015, Labbé et al. 2010, Oesch et al. 2018a, 2016, 2015, Ono et al. 2018, Skelton et al. 2014, Stark et al. 2009, Trenti et al. 2011, van Dokkum et al. 2013, Vanzella et al. 2008, 2005, 2006, 2009, Verma et al. 2007, Windhorst et al. 2011, Yabe et al. 2009). Along with the new data, theoretical models and cosmological simulations of galaxy formation have also seen important advances (e.g., Crain et al. 2015, Davé et al. 2019, 2017, García et al. 2017, Katsianis et al. 2015, Pillepich et al. 2018, Schaye et al. 2015, Tescari et al. 2014, Vogelsberger et al. 2013). Combining both approaches, it is possible to shed light on the galaxy formation and evolution processes in different environments and different cosmic epochs.

One particularly fundamental observational description of the galaxy population as a whole is the Cosmic Star Formation Rate Density (CSFRD): the total co-moving space density of star formation in the Universe (Lilly et al. 1996, Madau et al. 1996). By modeling galaxy emission at ultraviolet (UV), optical, and infrared (IR) wavelengths, we can unravel crucial information about the formation and evolution of galaxies, such as the history of mass assembly in galaxies across time and the role of galaxies in the reionization of the Universe (when the neutral intergalactic medium was ionized by the emergence of the first luminous sources, at $z \gtrsim 6$).

The latest review of SFRD estimations was the comprehensive compilation by Madau & Dickinson (2014) which includes different SFR indicators. Figure 1.1, extracted from Madau & Dickinson (2014), shows the cosmic SFRD from UV, optical, and IR data along with a

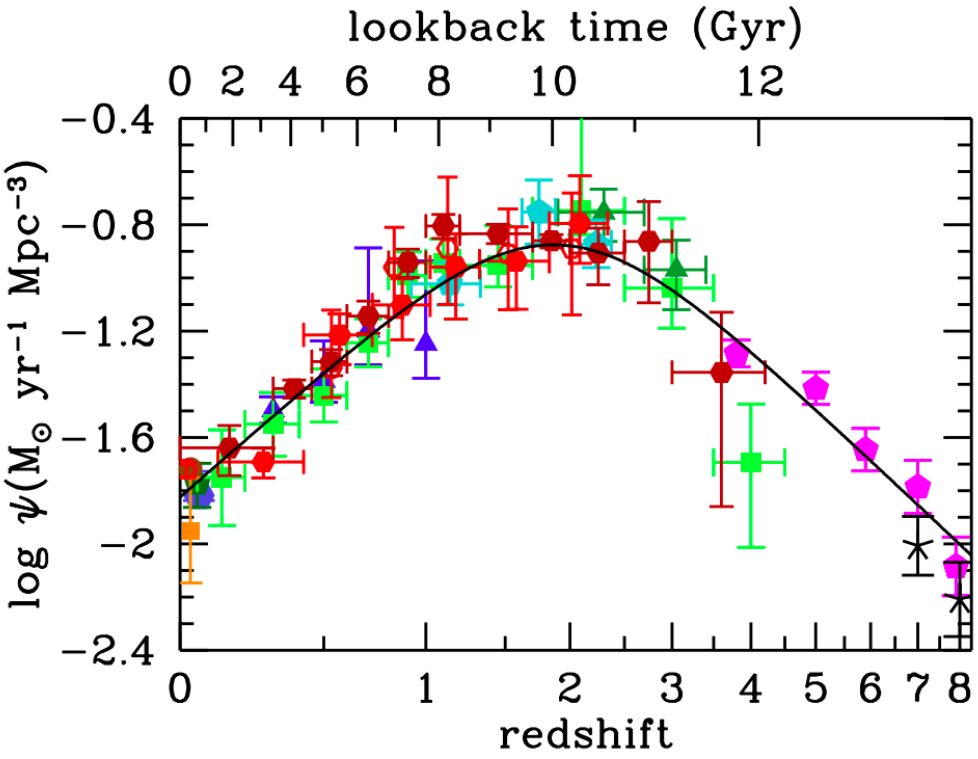

Figure 1.1: The Cosmic Star Formation Rate Density evolution extracted from Madau & Dickinson (2014) (Figure 9 of their article). They compiled FUV+IR rest-frame measurements (see references in their article). The solid curve is the best-fit to the data.

best-fitting function. The evolution of the SFRD is characterized by a rising phase with redshift, scaling from the present day as $\psi(z) \propto (1+z)^{2.7}$, reaching a peak at between $z = 1.5$ and 2 ($\sim$ 3.5 Gyr after the Big Bang), and a slower decline with redshift (but faster with time) as $\psi(z) \propto (1+z)^{-2.9}$ at $3 \lesssim z \lesssim 8$. This suggests that half of the stellar mass observed today was formed before $z = 1.3$, about 25% formed before the peak, and another 25% formed after $z = 0.7$ (roughly over the last half of the history of the Universe). Furthermore, today's CSFRD is the same as what we had at $z \sim 7$, or $\sim$ 750 Myr of the age of the Universe.

One interesting feature that was highlighted by Madau & Dickinson (2014), is the variety of random and systematic uncertainties associated with the different estimates. These uncertainties may play a significant role in the scatter seen in the relation. For instance, from Figure 1.1, the main uncertainties around the peak of star formation are introduced by faint sources in the IR luminosities and the corrections by dust in the UV luminosities.

Theoretical models have tried to reproduce the evolution of the SFRD but they show discrepancies with observations, particularly at high redshifts. The evolution of the SFRD has been studied by both semi-analytic models and hydrodynamical simulations (e.g., Davé et al. 2011, Fontanot et al. 2012, Gruppioni et al. 2015, Katsianis et al. 2017b, Tescari et al.

2014), and according to the authors, the lack of proper numerical implementation of feedback processes is the main factor explaining the differences. Because of the complexity of the feedback processes, further research with better physics and higher resolution simulations is needed. This is especially important for high redshift galaxies, which are more limited in terms of resolution and volume.

To better constrain the evolution of the SFRD we need direct observations at different cosmic epochs. Due to cosmic expansion, the light received by a remote observer from any given galaxy has a longer wavelength than emitted, i.e., is redshifted. This provides us with the great advantage of probing different cosmic epochs by just selecting galaxies at different redshifts.

This thesis aims to determine the luminosity function at high redshift ($z \sim 4.5$) from the Hα luminosity, which due to observational constraints, its estimation has represented a great challenge. From the Hα luminosity function, we can derive the star formation rate and estimate the star formation rate density, providing key constraints in the evolution of galaxies. To understand the relevance of the present work we will briefly review some prominent conceptions to keep in mind in the further analysis of our results.

1.2. The Luminosity Function

The Luminosity Function (LF) measures the volume density as a function of luminosity. It is typically derived for the rest-frame UV luminosity, the rest-frame optical and NIR luminosity, and for the rest-frame mid-IR and bolometric luminosities (Bouwens et al. 2020, 2010, 2015, Steidel et al. 1999 Blanton et al. 2003, Marchesini et al. 2007, Shapley et al. 2001, Sobral et al. 2013), Caputi et al. 2007, Khusanova et al. 2021, Le Floc'h et al. 2005, Reddy et al. 2008, Shapley 2011). All of them provide key insights into different processes that drive the evolution of galaxies.

The Luminosity Function (LF) (Schmidt 1968) is defined as

$$dn = \Phi(L)\mathrm{d}L \tag{1.1}$$

where $\mathrm{d}n(L)$ is the number of galaxies per unit volume with luminosities in the range $(L, L + \mathrm{d}L)$. A galaxy with a luminosity L will only be part of the observed sample if it is located within a maximum luminosity distance d_{max} corresponding to a redshift z_{max} and a comoving volume V_{max}, therefore, the galaxy could have been anywhere inside this volume. An estimation of the comoving number density of all the galaxies with luminosities in the range $(L, L + \mathrm{d}L)$ is

$$\Phi(L)\mathrm{d}L = \sum_i \frac{1}{V_{max}(L_i)}. \tag{1.2}$$

The luminosity function can also be derived from stepwise determinations which is a binned description of the LF. This method consists in maximizing the total probability for the whole galaxy sample given the model parameters, also known as the likelihood.

A common parameterization of the LF that has shown to be a good representation of the galaxy population up to very high redshift is the Schechter function (Schechter 1976), given by

$$\Phi(L) = \Phi^*(L/L^*)^\alpha \exp(-L/L^*) \tag{1.3}$$

where Φ^* is the normalization factor, α is the index that represents the faint-end slope, and L^* is the characteristic luminosity, also known as the "knee" of the luminosity function. For faint luminosities ($L < L^*$) the Schechter function approaches a power law, while at high luminosities ($L > L^*$) the luminosity distribution drops exponentially. These three parameters could change according to the cosmic epoch and the environment of the selected galaxies, and figuring this out is one of the purposes of the present work.

While this thesis is primarily focused on the Hα luminosity function, the UV LF is considered an important benchmark because of the great progress achieved in the study of its evolution. A number of studies have provided robust determinations of UV LF from the local to the high-redshift Universe up to $z \sim 10$ (Beckwith et al. 2006, Bouwens et al. 2004, 2006, 2010, 2015, 2021, Bunker et al. 2004, Dickinson 2000, Ford et al. 2003, Lehnert & Bremer 2003, Lorenzoni et al. 2011, Oesch et al. 2018b, Ouchi et al. 2004, Steidel et al. 1999, Yan & Windhorst 2004). Here we briefly review and summarize the main findings of the latest comprehensive compilation of the UV LF at high redshift, from $z \sim 2-10$, reviewed by Bouwens et al. (2021). Figure 1.2, extracted from Bouwens et al. (2021), shows the estimated UV LFs in filled points, and the Schechter fits as solid lines, each color represents a different redshift range from $z \sim 2$ to $z \sim 10$ (for further details about the redshift selection, see Figure 3 of their article). They estimate stepwise constraints on the UV LF for the range $z = 2-9$, and the UV LF at $z \sim 10$ from Oesch et al. (2018b) is also shown.

Figure 1.3 shows the evolution of the Schechter parameters α, M^*, and ϕ^* with redshift in the top, middle, and bottom panel, respectively. The solid red circles are from Bouwens et al. (2021) and Oesch et al. (2018b), and the light and dark red contours show their 68% and 95% constraints on the evolution of the faint-end slope α, $M^\star$, and $\log_{10}\phi^\star$ inferred from the fit to their LFs.

In terms of the Schechter function parameters, the evolution in Figure 1.3 revealed that

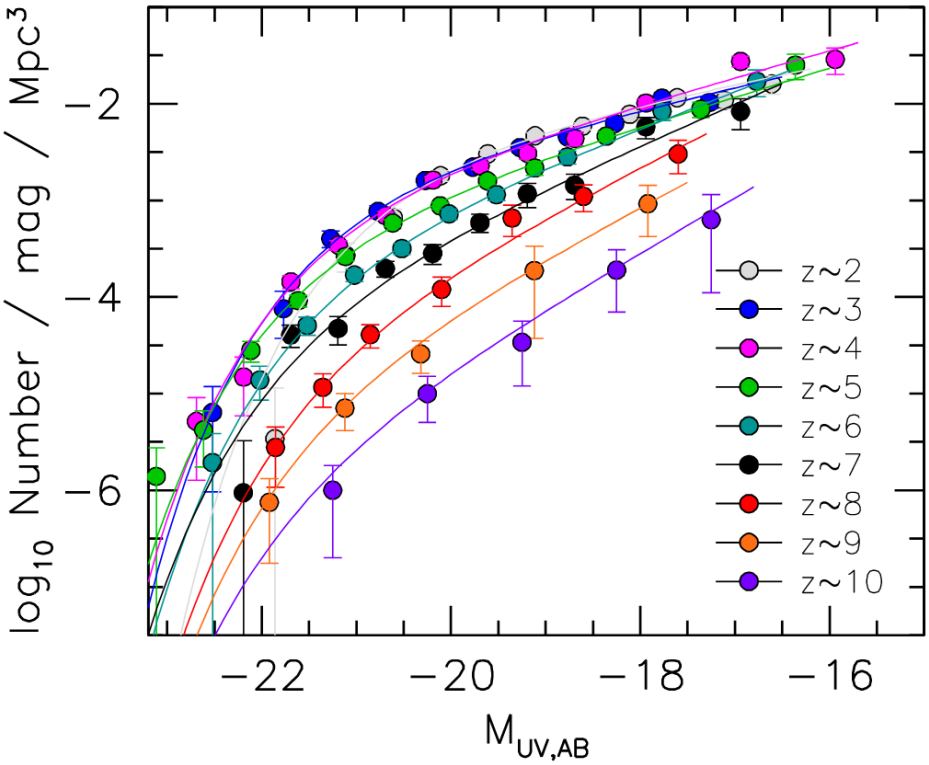

Figure 1.2: The UV Luminosity function extracted from Bouwens et al. (2021). The stepwise determinations are shown as solid circles in different colors for each redshift range. The best-fit Schechter LFs are shown with solid lines in the same color code of its corresponding redshift range.

the faint-end slope, α, steepens towards high redshift at a roughly constant rate with redshift. The characteristic luminosity, M^*, shows a fairly flat evolution in the range $z = 3 - 8$, with a value of $M^* = -21.02$, and becomes fainter at $z \lesssim 2.5$ when quenching becomes important (e.g. Peng et al. 2010, Scannapieco et al. 2005), while at $z > 3$ the exponential cut-off is explained by the presence of dust extinction (e.g. Bouwens et al. 2009, Reddy et al. 2010). The normalization factor, ϕ^*, decreases systematically towards high redshift and can be well described by a quadratic relationship in redshift being flatter at $z < 7$ than for $z > 7$.

Bouwens et al. (2021) reports that the evolution in the UV LF (from $z \sim 10$ to $z \sim 2.5$ at least) is strongly linked to the evolution of the dark matter halos with a simple fixed star formation efficiency model (Oesch et al. 2018b, Tacchella et al. 2018). Then, the evolution of the UV LF at high redshifts allows us to link the SFR to the growth rate of the dark matter halos.

The rest-frame UV luminosity of a galaxy is well correlated with its SFR. The UV LF, then, can inform us about the SFR activity in galaxies at different redshifts. In particular, the integral of the UVLF is closely linked to the CSFRD that we will discuss in Chapter 6.

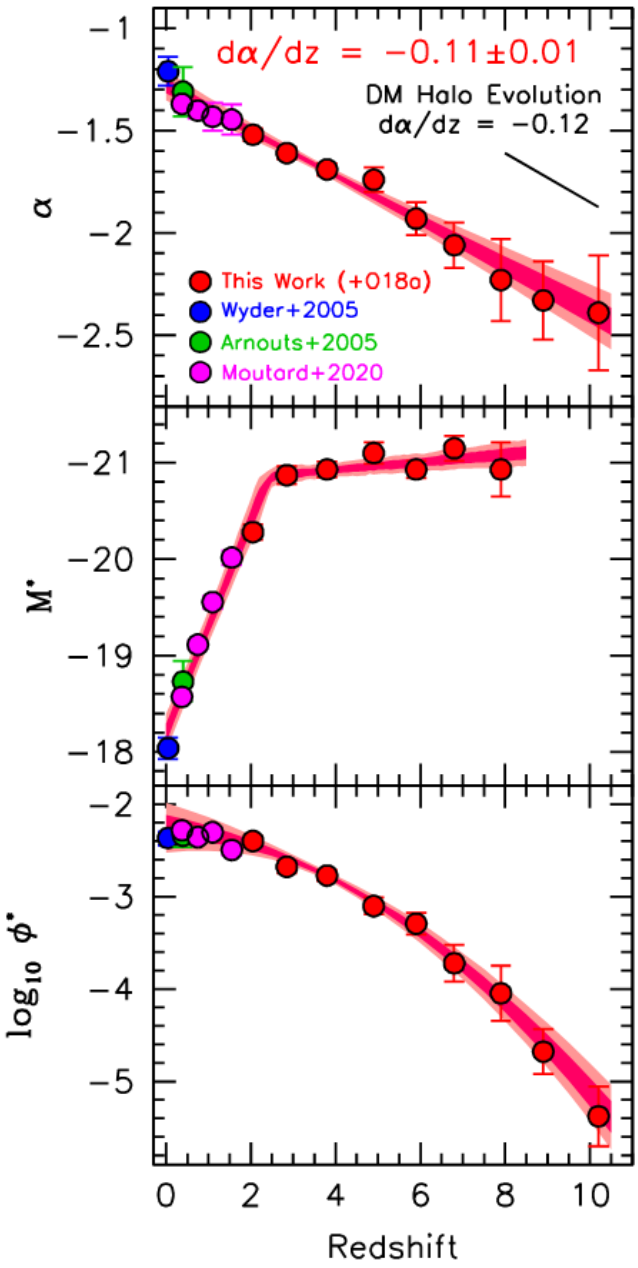

Figure 1.3: The evolution of the Schechter parameters from the best-fits presented in Figure 1.2, extracted from Bouwens et al. (2021). The evolution of the faint-end slope α, the characteristic luminosity M^*, and the normalization ϕ^* with redshift in the top, middle and bottom panels, respectively. For all panels the solid red circles are from Bouwens et al. (2021) and Oesch et al. (2018b). The compilation of the measurements also includes estimations at $z \sim 0.055$ from Wyder et al. (2005), at $z \sim 0.2 - 0.1$ from Arnouts et al. (2005), and the ranges $z = 0.3 - 0.45$, $z = 0.6 - 0.9$, $z = 0.9 - 1.3$, and $z = 1.3 - 1.8$ from Moutard et al. (2020). The light and dark red contours show their 68% and 95% constraints on the evolution of the faint-end slope α, M^*, and $\log_{10} \phi^*$ inferred from the fit to their LF results.

1.3. High-redshift Galaxies

This thesis makes use of data from very distant galaxies also known as high-redshift galaxies, which reveal information about the early epochs of cosmic evolution providing crucial constraints to characterize the evolution of galaxies. Due to their distance and small intrinsic size, high-z galaxies show very faint fluxes. Nevertheless, high-redshift galaxies have been studied with a variety of novel techniques in an increasing number of deep multiwavelength imaging surveys, such as Great Observatories Origins Deep Surveys (GOODS; Giavalisco et al. 2004), Cosmic Assembly Near-infrared Deep Extragalactic Legacy Survey (CANDELS; Grogin et al. 2011, Koekemoer et al. 2011), 3D-Hubble Space Telescope (HST, Brammer et al. 2012, Momcheva et al. 2016, Skelton et al. 2014, van Dokkum et al. 2011), Cosmological Evolution Survey (COSMOS; Scoville et al. 2007), Canada-France-Hawaii Telescope Legacy Survey (CFHTLS; Astier et al. 2005), Hyper-SuprimeCam Subaru Strategic Program (HSC-SSP; Aihara et al. 2018), VISTA Deep Extragalactic Observations Survey (VIDEO; Jarvis et al. 2013), the Hubble Deep, Ultradeep, and Extremely deep field (HDF/HUDF/XDF; Beckwith et al. 2006, Illingworth et al. 2013, Williams et al. 1996). In particular, the *Hubble Space Telescope* (HST) and *Spitzer Space Telescope* together with ground-based facilities have played an important role in collecting information about the high-redshift Universe. The HST Wide Field Camera 3 (WFC3) camera has significantly improved NIR sensitivity compared with several ground-based imaging, but it only samples optical rest-frame light until $z < 3$. *Spitzer*, with the Infra-Red Array Camera (IRAC), provides access to rest-frame optical at $z > 3 - 4$, key in constraining stellar mass.

The selection of high-redshift galaxies is usually based on photometric surveys as a first approach since it is extremely time-consuming to obtain spectra of faint galaxies even in the most sensitive telescopes available. Several techniques have been developed to progress in this field, either using broad-band or narrow-band photometry.

Broad-band based methods are aimed to obtain a low-spectral resolution ($R \sim 3.5$) spectral energy distribution (SED) of the galaxy. Several authors have applied techniques based on broad-band colors to select and classify galaxies by their mass, star formation rates, and dust obscuration levels (e.g., Bouwens et al. 2007, 2010, Daddi et al. 2004, Franx et al. 2003, Oesch et al. 2010, Ouchi et al. 2004, Steidel et al. 1996, van Dokkum et al. 2013). By using the shift of characteristic spectral features as a function of redshift, a rough estimation of the redshift can be made, the so-called photometric redshift. A major advantage is that photometric redshifts (z_{phot}) can be estimated much faster and cheaper than spectroscopic redshifts (z_{spec}), although they are less reliable. The reliability and accuracy of the photometric redshifts depend on the number and the widths of the filter bands used, and also on whether the bands contiguously cover the wavelength range where we expect the main features. One of the most important galaxy surveys estimating photometric redshifts with HST is the Cosmic Assembly Near-infrared Deep Extragalactic Legacy Survey (CANDELS) (Grogin et al. 2011,

Koekemoer et al. 2011) which is divided into two layers. The CANDELS/Deep survey covers ~ 125 arcmin^2 reaching a 5σ point-source limit $H = 27.7$ mag within Great Observatories Origins Deep Survey (GOODS)-N and GOODS-S, while the CANDELS/Wide survey reaches a 5σ point-source limit of $H = 27.0$ mag.

Another method to select high-z galaxies uses narrow-band photometry to select Lyα emitters (LAEs). When the Lyα emission line (1216Å) shifts to the optical range, LAEs can be selected at $z \gtrsim 3$. The confirmation of the presence of the Lyα is needed with follow-up spectroscopy of the candidates (e.g., Partridge & Peebles 1967). This technique is highly sensitive to star-forming galaxies, but not all of them feature Lyα emission due to dust extinction effects. Therefore, the LAE selection is biased toward star-forming galaxies with low dust levels.

One of the most common techniques used to select high-redshift galaxies, and the most relevant for this work, is the Lyman Break Galaxy (LBG) technique, which leverages a prominent spectral break expected in the rest-frame UV. All star-forming galaxies show a break in their Spectral Energy Distribution (SED) at 912Å also known as the Lyman limit. Beyond the Lyman limit, the spectrum is truncated due to the absorption of the neutral hydrogen, which may be located in the interstellar medium of galaxies, or along the intergalactic sightline between the observer and the source. Also, the intergalactic and circumgalactic gas of the Lyα forest removes light below 1216Å introducing an additional spectral break shortward of Lyman α. At higher redshift ($z \gtrsim 3$), this flux suppression is increasingly strong as the Lyα forest thickens. The Lyman break technique can be thought of as a simple form of photometric redshift that selects star-forming galaxies and takes advantage of spectral signatures.

Figure 1.3 (top and bottom), extracted from Dickinson (1998), shows a Lyman break galaxy at $z = 3$ almost disappearing from the near-ultraviolet band U, while the $B-V$ color in the optical range is still blue or fairly flat, and the $U-V$ color is extremely red. LBGs are identified in a specific redshift range from the color indices, so they occupy distinct areas in suitable color-color diagrams. Thus, for galaxies at $z \sim 3$ the rest-frame Lyman limit shifts between bandpasses U_{300} and B_{450}, and the galaxy "drops-out" when viewed through the bluer filter because of the suppression of its flux.

To date, many studies have taken advantage of this technique at much higher redshifts. For instance, at $z \sim 4-5$ galaxies fade from the $B-$band but they are still detected in the $V-$band. The major disadvantage of the LBG technique is that it selects preferentially galaxies that are relatively unobscured and with active ongoing star formation. Therefore, it is not sensitive to passive galaxies or high dust-reddening, and they would be missed by this UV technique. Despite these possible biases, the LBG selection criterion is of great value due to the lack of abundant spectroscopic surveys. It consists of a simple set of selection criteria that can be easily applied, e.g. to models, so they enable accurate comparisons while

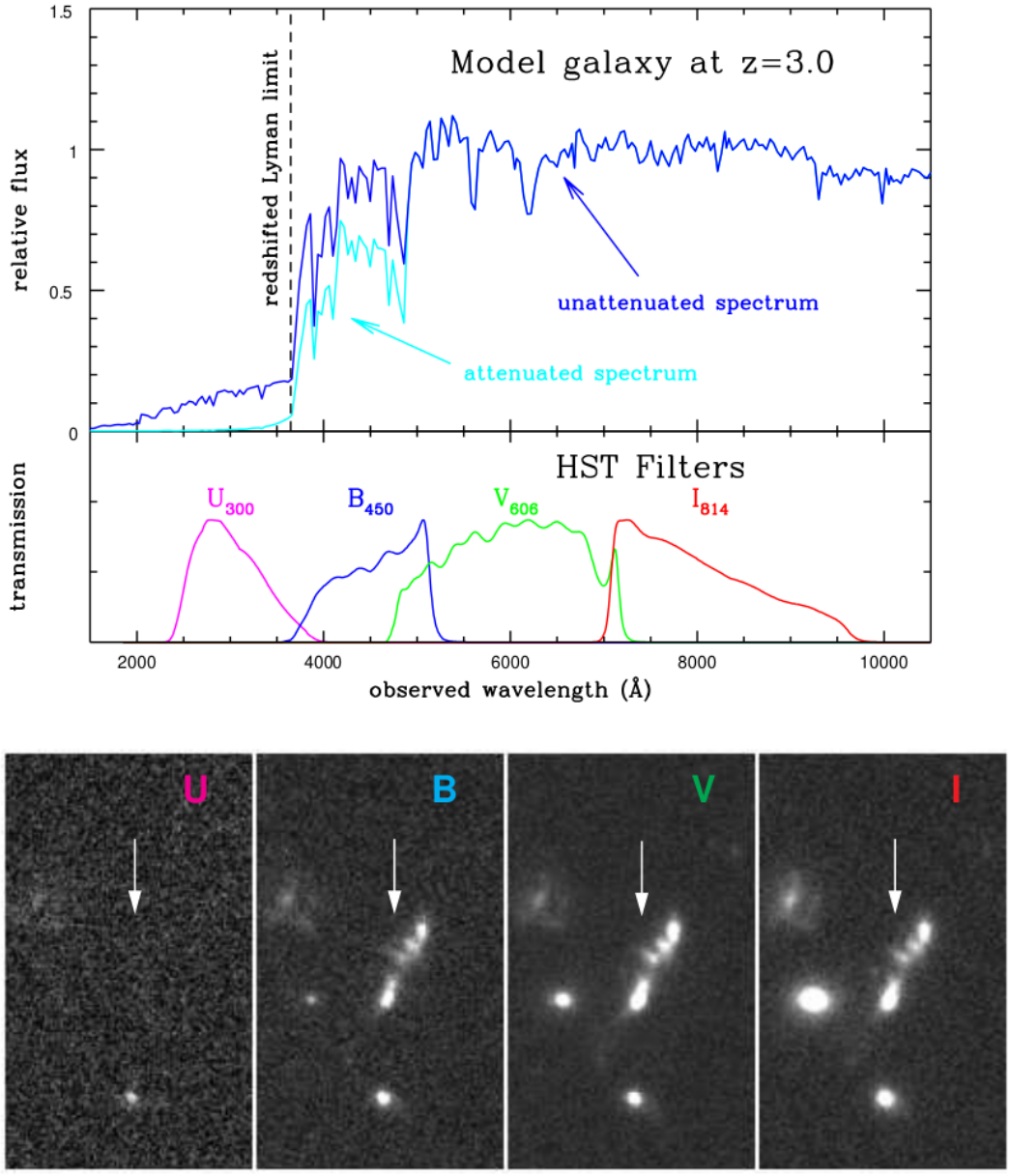

Figure 1.4: Extracted from Dickinson (1998), illustrates the Lyman Break Technique applied in the Hubble Deep Field (HDF). *Top*: model spectrum of a star forming galaxy observed at $z = 3$. The roughly flat continuum is truncated at 912Å limit, which is redshifted between the U and B filters (transmission curves are shown below the spectrum). The effects of intergalactic neutral hydrogen further suppress the continuum in the $U-$ and $B-$bands. *Bottom*: Imaging of an HDF galaxy in the 4 filters. It is visible in the $I-$, $V-$, and $B-$bands, but it vanishes in the $U-$band image. This galaxy has been spectroscopically confirmed to have $z = 2.8$.

photo$-z$ selections can strongly depend on the adopted template set. It also guarantees large numbers of galaxies, allowing us to obtain robust statistical results and has been effectively used to characterize the luminosity distribution of galaxies.

1.4. Star Formation Rate tracers

Given the wavelength coverage of our data, the present work is mainly focused on the UV and Hα luminosity as star formation rate tracers. The Hα line at 6563Å is the rest-frame optical emission originated because young, massive stars ($> 10 M_{\odot}$) produce ionizing photons that ionize the surrounding gas. Then, it provides an estimate of the star formation rate over timescales of ~ 10 Myr and has the advantage of being up to $\times$ 3 times less affected by dust extinction than UV wavelengths. On the other hand, the UV-continuum emission is mainly produced by very young, massive stars (~ 3 $M_{\odot}$), OB spectral type. It allows us to trace star formation rate on timescales roughly homogeneous over $100 - 300$ Myr. As reviewed previously, at high redshift ($z \gtrsim 4$) the UV emission from galaxies has been carefully studied obtaining determinations of the luminosity function up to $z \sim 10$. However, the majority of star formation takes place in dusty environments where UV photons are reprocessed by dust into IR emission, therefore, the UV emission could be significantly affected by dust extinction.

Kennicutt (1998b) determined transformation coefficients into SFR from the UV luminosity, over the wavelength range $1500 - 2800$Å, and the Hα luminosity at 6563Å. As these indicators are sensitive to the presence of massive stars, it is necessary to assume a particular form of the initial mass function (IMF) to extrapolate these values down to the low stellar masses to obtain the total SFR. Some authors have estimated the shape of the IMF with the main differences at low masses (e.g., Chabrier 2003, Kroupa 2001, Salpeter 1955, Scalo 1986). The most commonly used IMF at high redshift, in the last few years, has been the Chabrier (2003) IMF.

Figure 1.1 shows data following a clear trend, but there is also a significant scatter. A much debated question is how the different SFR tracers contribute to the observed scatter in the SFRD evolution, whether there are systematic offsets between different ways to estimate SFR or if it is something intrinsic. Moreover, an increasing numbers of authors have reported a discrepancy between the SFRs inferred by different methodologies (e.g., Boquien et al. 2014, Davies et al. 2016, 2017, Fumagalli et al. 2014, Katsianis et al. 2017b, Utomo et al. 2014). In this thesis, we particularly investigate the differences between UV and Hα as SFR tracers.

The comparison between UV and Hα-based SFRs could be informative about the Star Formation Histories (SFHs) of galaxies. Understanding the origin of these differences represents a major challenge at all redshifts (Emami et al. 2019, Katsianis et al. 2017b, Kennicutt & Evans 2012, Madau & Dickinson 2014, Smit et al. 2016), and it is one of the main goals of the present work. Short-time variations in the SFR also called "burstiness", can be investigated by comparing SFR(Hα) and SFR(UV), since they trace different timescales. While the Hα nebular emission traces SFR over ~ 10 Myr, the UV continuum traces SFR over ~ 100 Myr. In the case of a constant star formation, the ratio between these two indicators will

be close to unity after 100 Myr, whereas deviations are to be expected for rapidly varying (burst) star formation. For the same burst period, the SFR(Hα) will undergo changes in a shorter period of time than the SFR(UV). Therefore, if a burst of instantaneous star formation occurs within a 10 Myr period, the SFR(Hα) will increase before the SFR(UV) and the ratio SFR(Hα)/SFR(UV) will be > 1. After the burst, the UV emission will remain high even ~ 100 Myr after the burst happened because lower mass stars live longer, whereas the Hα emission fades within 10 Myr, leading to SFR(Hα)/SFR(UV) < 1.

Many authors have investigated the differences between both SFR(Hα) and SFR(UV) as possible changes in their SFHs (Atek et al. 2022, Emami et al. 2019, Faisst et al. 2019, Guo et al. 2016, Smit et al. 2016, Weisz et al. 2012). For instance, Atek et al. (2022) show that low mass galaxies at $0.7 < z < 1.5$ tend to have SFR(Hα) elevated compared to SFR(UV) which they interpret as burstiness. Similar differences have also been found in other studies, as Katsianis et al. (2017a,b) reported, suggesting that they may be more prominent at higher redshifts. Shivaei et al. (2015), however, investigate the SFR(Hα) and SFR(UV) at $z \sim 2$ and conclude that they are roughly consistent when using a Calzetti et al. (2000) dust attenuation curve, i.e., the comparison between SFR(Hα) and SFR(UV) is sensitive to dust corrections. These differences may due to different ranges of stellar mass, while the galaxies from Atek et al. (2022) are in the range of $M_\star \sim 10^8 - 10^{10} M_\odot$, the sample from Shivaei et al. (2015) have $M_\star \sim 10^{9.5} - 10^{11.5} M_\odot$, which could have a major impact on the intensity of the Hα flux.

Shivaei et al. (2015) investigate the impact of dust by using different attenuation recipes to test how the relationship between UV- and Hα-based SFRs at $z \sim 2$. They used the Galactic reddening curve from Cardelli et al. (1989), the extinction curve from the Small Magellanic Cloud (SMC) proposed by Gordon et al. (2003), and the Calzetti et al. (2000) attenuation curve, and concluded that the latter provides a better agreement between SFR(Hα) and SFR(UV).

A further source of uncertainty in the SFR(Hα) and SFR(UV) comparison comes from the color excess of the ionized gas compared to the stellar continuum. It has been reported that $E(B-V)_{nebular} = 0.4 E(B-V)_{continuum}$ (Calzetti 1997, Calzetti et al. 2000). This would be because nebular emission lines from dense HII regions tend to be more obscured than the stellar continuum light. However, the factor 0.4 was derived as an average value of a wide variety of galaxy populations in the local Universe, and some authors claim that a factor close to unity seems to better balance both tracers, SFR(UV) and SFR(Hα), e.g., at $z \sim 2$ Shivaei et al. (2015). This is also true at higher redshift ($z \sim 4$), where the assumption of larger color excess for the nebular lines than stellar continuum further deepens the difference between SFR(Hα) and SFR(UV) (Smit et al. 2016).

Most of the uncertainties associated with the estimation of SFR come from the correction by dust extinction. While the UV luminosity is the most commonly used SFR estimator at

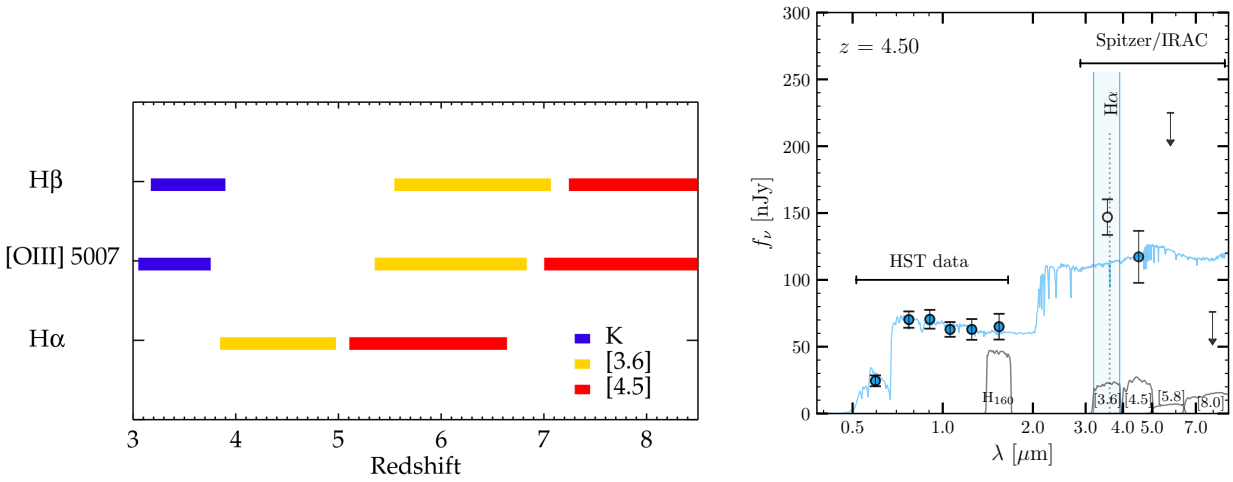

Figure 1.5: *Left*: Extracted from Stark et al. (2013), shows the bands in which Hα and other emission lines can be detected as a function of redshift. The Hα emission line can be isolated and detected at $3.8 \lesssim z \lesssim 5$. *Right*: Broad-band *HST*+IRAC photometry in black points and the estimated spectral energy distribution of the continuum in the light blue line. The redshifted wavelength of Hα is shown with the vertical dotted line, which falls in the measurement range of the IRAC [3.6] band, whose wavelength coverage is shown by the shaded area and reference filter transmission curves are shown at the bottom. The observed photometry in IRAC [3.6] seems to be boosted by the presence of the Hα emission line, while the other bands sample strictly the stellar continuum.

high redshift ($z > 3$), the Hα luminosity is a more direct SFR indicator and less uncertain. This advantage has been exploited by many studies in galaxies up to $z \lesssim 2.8$ (Coughlin et al. 2018, Erb et al. 2006, Förster Schreiber et al. 2009, Geach et al. 2008, Hanish et al. 2006, Hayes et al. 2010, Ly et al. 2011, Weisz et al. 2012). In particular, Sobral et al. (2013) investigate the evolution of the Hα luminosity function, suggesting a fairly flat evolution in the faint-end slope α, increasing evolution with redshift of the characteristic luminosity L^*, and a decreasing evolution with redshift of the normalization parameter ϕ^* from $z = 0.84$ to $z = 2.2$. They take advantage of the redshifted Hα line up to $z = 2.2$, where Hα can still be detected by the $K-$band.

Unfortunately, at higher redshifts ($z \gtrsim 3$) the Hα line is no longer detected in the $K-$band, as the left panel of Figure 1.5 shows. For this reason, most SFR estimates at $z > 3$ tend to be based exclusively on the rest-frame UV luminosity. Compared to what we know about the UV LF, our knowledge of the evolution of the Hα LF at high$-z$ is much more limited. Despite this, there are redshift windows that can be exploited to estimate the Hα flux at high redshift, in particular, using deep *Spitzer*/IRAC photometry. As the left panel of Figure 1.5 shows, at specific redshifts, strong nebular lines in the rest-frame optical contribute to the flux measured in one of the IRAC bands, for example, we can detect Hα in the IRAC [3.6] band in the redshift range $3.8 \lesssim z \lesssim 5.0$. The right panel of figure 1.5 shows the data

coverage of the present work (*HST*+IRAC photometry), and illustrates that the IRAC [3.6] band is affected by the presence of the redshifted Hα emission line, shown in the dotted vertical line, while the other bands sample strictly the stellar continuum, shown by the blue curve. This color offset can be used to estimate the flux of the nebular lines. Several studies have taken advantage of this offset to infer the intensity of nebular emission lines at $z > 3$ (Caputi et al. 2017, De Barros et al. 2019, Faisst et al. 2017, Mármol-Queraltó et al. 2016, Rasappu et al. 2016, Shim et al. 2011, Shivaei et al. 2015, Smit et al. 2016, Stark et al. 2013) and even at $z \sim 8$ (Stefanon et al. 2022). In this work, we make use of this technique to estimate the Hα flux of galaxies selected at $z \sim 4.5$.

1.5. This work

In this thesis, we present novel estimates of the Hα Luminosity Function at $z \sim 4.5$, where Hα spectroscopy is not available yet. New determinations of Hα LF will provide valuable information to reconstruct the evolutionary history of galaxies in rest-frame optical wavelengths, where the light is less affected by dust corrections than in the UV. We take advantage of the photometric excess in the IRAC [3.6] band where the redshifted Hα line falls for galaxies at $3.8 \lesssim z \lesssim 5.0$ to estimate the Hα luminosities. We have also tested multiple methods to estimate the Hα fluxes, and we make use of the spectral energy distribution (SED) modeling.

The SED modeling of the galaxies arises from the necessity to estimate physical properties, such as the stellar mass, the star formation rate, dust extinction, stellar age, and metallicity. The observed photometry is compared with synthetic galaxy spectra to derive quantitative information. A wide variety of numerical codes have been developed to produce synthetic spectra, which are used to predict the spectral continuum, luminosities, and color indices of stellar systems (e.g., Boquien et al. 2019, Bruzual & Charlot 2003, Fioc & Rocca-Volmerange 2019). These predictions are obtained by varying the input parameters until the synthetic spectra match the observed spectra. In this thesis, we use CIGALE (Boquien et al. 2019) with different combinations that will be detailed later.

The ability to estimate the contribution of nebular emission lines to *Spitzer*/IRAC photometry, depends strongly on the depth of the IRAC imaging. In this work, we take advantage of the new, full-depth *Spitzer*/IRAC imaging from the GOODS Re-ionization Era wide-Area Treasury from Spitzer (GREATS) program (PI: I. Labbé, Stefanon et al. 2021), reaching up to 250 hrs of integration. The GREATS program provides the deepest Spitzer/IRAC observation available to date, extending the ultradeep coverage in the [3.6] and [4.5] bands reaching a 1σ sensitivity of 28.7 and 28.3, respectively. The available coverage in the [5.8] and [8.0] bands is shallower, reaching a 1σ depth of 26.0 and 25.8.

We exploit the redshift window shown in Figure 1.5 in which we can isolate the contri-

bution of the Hα line and estimate the Hα luminosity function at $z \sim 4.5$, with the best constraints provided by unique data in IRAC [3.6] and [4.5]. We explore standard corrections for dust attenuation to estimate intrinsic luminosities, needed to derive the SFR(Hα), which are significantly less sensitive to the assumptions used compared to dust corrections for UV luminosities. Finally, we determine the SFR function and its integral: the cosmic star formation rate density at $z \sim 4.5$ from Hα, offering an important contribution to the current understanding of the cosmic star formation history of the Universe presented in Figure 1.1.

This thesis is organized as follows. In Chapter 2, we describe the data that has been used, and in Chapter 3 how the final sample of spectroscopic and photometric redshift galaxies was selected. Chapter 4 is concerned with the methodology used to measure the Hα flux, describing the methods used to derive it and their limitations. In Chapter 5 we derive the Hα Luminosity Function (Hα LF) and its best-fit Schechter parameterization. In Chapter 6 we derive star formation rates from the Hα fluxes and the UV luminosities and compare them. We also derive the star formation rate function at $z \sim 4.5$. In Chapter 7 we discuss our findings, and compare them with previous studies and other SFR tracers commonly used at high-redshift. A summary and conclusions of the main results are presented in Chapter 8. Throughout this thesis, we use $H_0 = 70$ kms^{-1} Mpc^{-1}, $\Omega_m = 0.3$, and $\Omega_\Lambda = 0.7$. Magnitudes are quoted in the AB systems (Oke & Gunn 1983). A Chabrier (2003) initial mass function (IMF) is assumed for stellar mass $M_\star$ and SFR measurements. Abbreviations of the *HST* bands F435W, F606W, F775W, F850LP, F105W, F125W, F140W and F160W are as follows B_{435}, V_{606}, i_{775}, z_{850}, Y_{105}, J_{125}, JH_{140} and H_{160}.

Chapter 2

Data

2.1. Sample Selection and HST data

This work is based on the Lyman break galaxy (LBG) selection by Bouwens et al. (2015), focusing in particular on the sources at $z \sim 4$ and $z \sim 5$ ($B-$ and $V-$dropouts, respectively) found over the GOODS fields (Giavalisco 2002). Their selection makes use of ultradeep, wide-area observations obtained as part of the CANDELS program (Grogin et al. 2011, Koekemoer et al. 2011) over the GOODS-North, GOODS-South fields, the ERS field (Windhorst et al. 2011), and the UDF/XDF (Beckwith et al. 2006, Illingworth et al. 2013) field. The available photometry from *HST* includes the B_{435}, V_{606}, i_{775}, I_{814}, z_{850}, J_{125}, JH_{140} and H_{160} bands, reaching 5σ depths between 26.2 and 28 in the CANDELS fields, between 26.4 and 27.7 in the ERS field, and ranging from 29.2 to 30 in the XDF field. The total search area corresponds to ~ 300 arcmin^2 where Bouwens et al. (2015) identified 7574 star-forming galaxy candidates selected as $B-$ or $V-$dropouts are expected to have $z \geq 3$.

The samples at $z \sim 4$ and $z \sim 5$ were selected by Bouwens et al. (2015) (see Figure 1 of their article) using the following LBG criteria:

- At $z \sim 4$:

$$(B_{435} - V_{606} > 1) \wedge (i_{775} - J_{125} < 1) \wedge$$
$$(B_{435} - V_{606} > 1.6(i_{775} - J_{125}) + 1) \wedge$$
$$(\text{not in } z \sim 5 \text{ selection})$$

- At $z \sim 5$:

$$(V_{606} - i_{775} > 1.2) \wedge (z_{850} - H_{160} < 1.3) \wedge$$
$$(V_{606} - i_{775} > 0.8(z_{850} - H_{160}) + 1.2) \wedge$$
$$(S/N(B_{435}) < 2) \wedge (\text{not in } z \sim 6 \text{ selection})$$

The most significant source of contamination in the sample are lower-redshift galaxies that spuriously satisfy the color-color criteria due to the effect of photometric noise (see Section 3.5.5 in Bouwens et al. 2015). However, this represents minimal contamination since it was carefully estimated by adding noise to real observations, providing a direct and robust estimate. Overall, the contamination rates produced by stars, transient sources, lower redshift objects, extreme emission lines galaxies (EELGs), and spurious sources were estimated to be a total level of contamination of just $\sim 2\%$ and $\sim 3\%$ for the $z \sim 4$ and $z \sim 5$ samples, respectively.

Our initial sample contains 5712 $B-$dropouts at $z \sim 4$ and 1862 $V-$dropouts at $z \sim 5$.

2.2. GREATS Spitzer/IRAC Photometry

In this work, we will measure Hα fluxes based on the impact that the line has on broad-band photometry. As the right panel of Figure 1.5 shows, at $z > 3.8$ this require *Spitzer*/IRAC imaging at 3.6μm and 4.5μm. Here we take advantage of new full-depth Spitzer/IRAC 3.6μm and 4.5μm imaging from the *GOODS Re-ionization Era wide-Area Treasury from Spitzer* (GREATS) program (PI: I. Labbé, Stefanon et al. 2021) over the GOODS-N and GOODS-S fields.

The GREATS dataset extends the ultradeep coverage in the [3.6] and [4.5] bands with $>$ 150hr of deep data (corresponding to a 1σ sensitivity of 28.7 and 28.3 mag in the [3.6] and [4.5] bands) across $\sim$ 150 arcmin^2 ($\sim$ 1/2 total area of the GOODS fields). The GREATS mosaics reach an impressive 250 hr coverage in a small $\sim 5-10$ arcmin^2 region in each field in the [3.6] and [4.5] bands. The available coverage in the [5.8] and [8.0] bands is shallower. In the GOODS-N field, the maximum coverage is $\sim$ 90 hr, corresponding to a 1σ depth of 26.0 and 25.8 for the [5.8] and [8.0] bands. For the GOODS-S field, the maximum depth is $\sim$ 40 hr, corresponding to 1σ limits of 25.6 and 25.4 in the [5.8] and [8.0] bands.

The deep imaging and slightly low-resolution of the [3.6] and [4.5] mosaics create source blending issues that may limit our ability to perform photometry (the confusion limit). The present work makes use of MOPHONGO (Labbé et al. 2015), a source deblending software that exploits the high-resolution imaging available from *HST* on the same fields to model the light profile of all sources in the field and remove possible contamination from nearby sources. A demonstration of the confusion limit and how it is solved by this method is shown in Figure 2.1, extracted from Labbé et al. (2015), where the prior-based IRAC photometry can recover the full depth of the IRAC data (see Section 4 from Labbé et al. 2015 for details).

To test the performance of the code on our data, Stefanon et al. (2021) performed Monte Carlo simulations that consist of injecting synthetic point sources at random positions. Then, their flux densities were measured with MOPHONGO and corrected to total using the bright-

ness profile of each source on the low-resolution image and the Point Spread Function (PSF) reconstructed at the specific locations of each source. They showed that the code recovers the fluxes of the synthetic sources within the expected noise independent of luminosity, with only a small fraction ($\lesssim 10\%$) of sources deviating appreciably ($> 5\sigma$) from the true flux. Therefore, source confusion in the deep IRAC imaging can be reliably mitigated even in the faintest regimes (see Stefanon et al. 2021 for details).

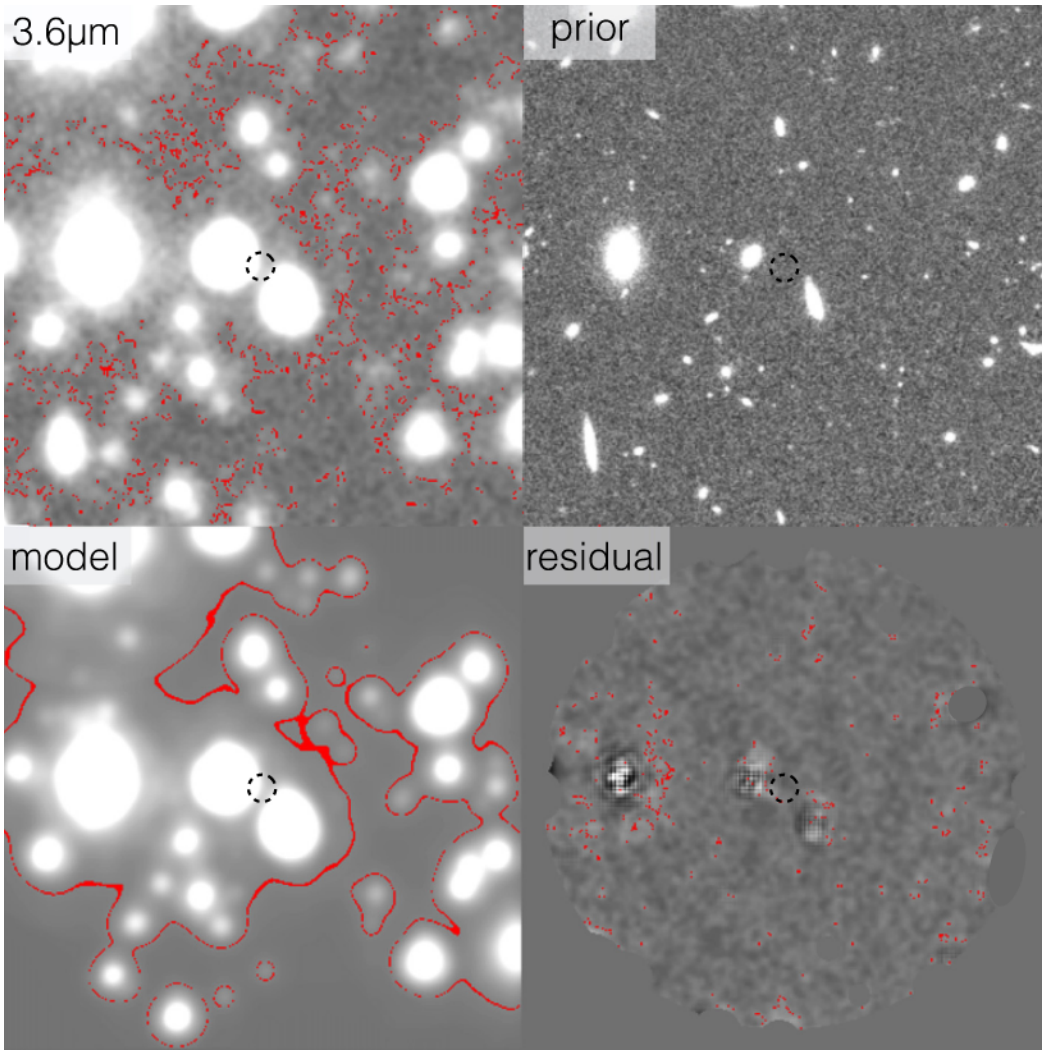

Figure 2.1: Demonstration of how to overcome the confusion limit in IRAC photometry, extracted from Labbé et al. (2015), the black dashed aperture shows the location where the flux is to be measured in all panels. *Top left*: shows the IRAC 3.6 μm mosaic along with the 2.5σ isophote above the background as red contours, implying that the point spread function (PSF) wings contaminate $\sim 70\%$ of the background. *Top right*: Deep *HST*/WFC3 imaging of the same position on the sky. *Bottom left*: The model constructed after the convolution of each WFC3 detected source to approximate a high quality IRAC PSF to account for the PSF wings. *Bottom right*: The residual image after modeling and subtraction shows that source confusion is impressively reduced.

Chapter 3

The sample for Hα measurements at $z \sim 4.5$

The ability to estimate the contribution of the Hα line to *Spitzer*/IRAC in the [3.6] μm band depends strongly on the depth of IRAC imaging and on the redshift selection. Starting from the original sample of $B-$ and $V-$dropouts, we have imposed restrictions on the quality of the IRAC photometry and the redshifts to estimate Hα on a reliable sub-sample.

3.1. IRAC Photometry

As described above, MOPHONGO mitigates the problem of source confusion in deep IRAC images. The code automatically flags poor neighbor subtraction but we have also chosen to inspect by eye all the residual images, discarding the sources with strong residuals in the area where we perform aperture photometry. Since this criterion depends primarily on the ability to model the neighboring sources, it is not expected that it will introduce any significant biases in the sample.

As will be discussed later (see Chapter 4), our method to estimate Hα from broadband photometry relies on accurately estimating the stellar continuum flux in the rest–frame optical, near the wavelength of Hα. This requires an appropriate *signal-to-noise* ratio in both IRAC bands. We have imposed a S/N > 2 in the IRAC [3.6] and [4.5] bands simultaneously. To ensure a good performance of the spectral energy distribution we also imposed $\chi^2_{\rm SED} < 10$. We reduced the parent sample for $B-$dropouts from 5712 to 2967 and for $V-$dropouts from 1862 to 899.

3.2. Redshifts

At redshifts $3.86 < z < 4.94$, the Hα line contributes flux to the IRAC [3.6] band while the IRAC [4.5] probes the continuum free from significant line emission (see the right panel of Figure 1.5). Accurate redshifts are important to ensure that Hα is at the right redshifted

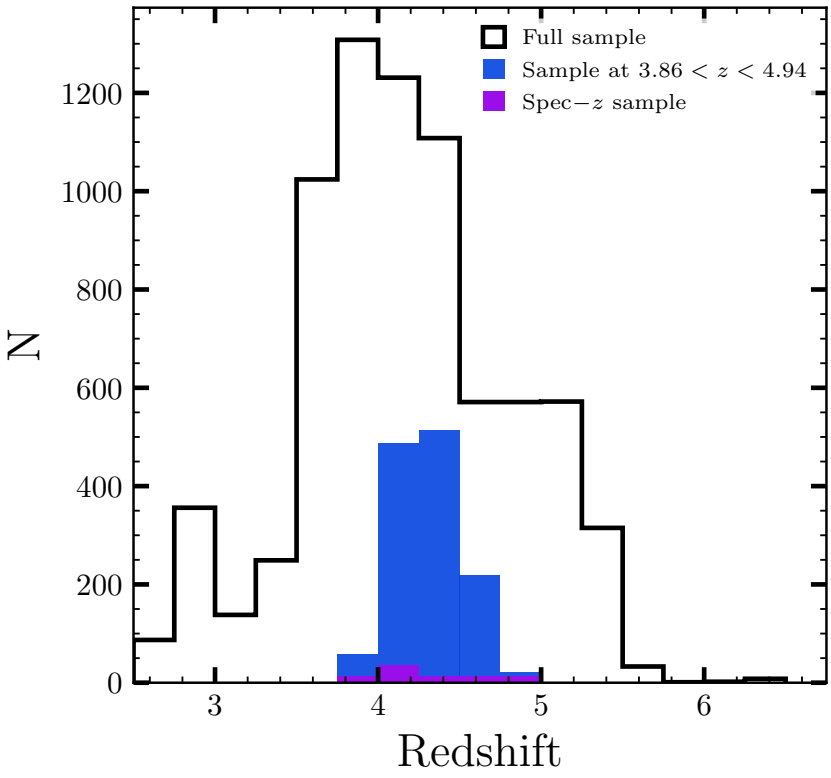

Figure 3.1: Comparison between the redshift selected samples at $3.86 < z < 4.94$ (blue histogram) and the parent sample of $B-$ and $V-$dropouts (black histogram). The selected sample includes $B-$ and $V-$ drop, according to their lack of brightness in the B_{435} and V_{606} bands, respectively, and the redshifted Hα emission falls in the measurement range of the 3.6μm band. The median redshift of the sample is $z \sim 4.3$, taking into account the spec$-z$ and photo$-z$ sample. The selection criteria that assess the quality of data are the same in both samples (see Chapter 3) related to reliable IRAC photometry (e.g., cuts based on IRAC S/N, quality of the SED fit) and accurate redshifts.

wavelength so our work makes use of spectroscopic redshifts when available, but it also uses photometric redshifts for which we can find the line with high confidence.

3.2.1. Spectroscopic Sample

We match our $B-$ and $V-$dropout catalogs with the spectroscopic samples by Herenz et al. (2017), Oyarzún et al. (2017), Oyarzún et al. (2016), Shim et al. (2011), Stark et al. (2013), Vanzella et al. (2005), Vanzella et al. (2006), Vanzella et al. (2008), Vanzella et al. (2009), and Balestra et al. (2010) over the GOODS-South and GOODS-North fields. Redshifts in these works are mainly derived from prominent features such as Lyα in emission but there are also redshifts based on UV absorption features. As a result, we have found 69 $B-$dropouts and 21 $V-$dropouts with spectroscopic redshift between $z = 3.96 - 4.94$.

3.2.2. Photometric Redshift Sample

Our fiducial estimates of Hα fluxes make use of SED fitting, which, in the case of sources without spectroscopic redshift, includes fitting for the best redshift. For the SED fitting we use the code CIGALE (Boquien et al. 2019; more details in Section 4.1), which can estimate the probability distribution function (pdf) for the redshift (marginalizing over all other parameters of the fit and assuming a flat prior). We model the photometric redshift excluding the IRAC bands with potential nebular emission contamination. We select sources that have at least 80% probability of being at the desired redshift range. This results in 1209 sources with a reliable photo$-z$ at $z = 3.86 - 4.94$, for which Hα contributes flux to the [3.6] band. A summary of all the selection criteria applied to the original LBG sample to obtain our reduced sample for Hα measurements is shown in Table 3.1.

Table 3.1: Summary of Sample Selection for Hα measurements

Selection Criteria	N°
Full Sample	7574
Clean Sample	3866
$S/N_{3.6}$, $S/N_{4.5} > 2$	
$\chi^2_{SED} < 10$	
Redshift Sample	1299
$\mathbb{P}(3.86 < z < 4.94) > 80\%$	
photo$-z$	1209
spec$-z$	90

3.2.3. Spectroscopic Sample vs. Photometric Sample

Figure 3.1 shows the redshift distribution of the parent sample of $B-$ and $V-$dropouts as well as the spectroscopic and photometric redshift samples that in total add up to 1299. Figure 3.2 further compares the spectroscopic and photometric redshift samples at $z \sim 4.5$. The differences in redshift distribution, shown in the top panel of Figure 3.2, are most likely explained by the selection function and the sizes of the parent samples of the different studies included in the spectroscopic sample. The UV-continuum slope, β, was determined to fit all the fluxes between the Lyman break and the Balmer break (z_{850}, J_{125}, JH_{140}, and H_{160}) with a power law $f_\lambda \propto \lambda^\beta$. The top left panel of Figure 3.2 shows that both samples have very similar rest-UV colors, with median β values of -1.92 and -1.94 for the spectroscopic and photometric samples, respectively. The bottom left panel shows the distribution of the UV-to-optical color, $H_{160} - [4.5]$, indicating slightly bluer colors in the spec$-z$ sample, probably indicative of slightly younger ages. The bottom right panel suggests no significant differences between the stellar masses of the spec$-z$ sample and the photo$-z$ sample.

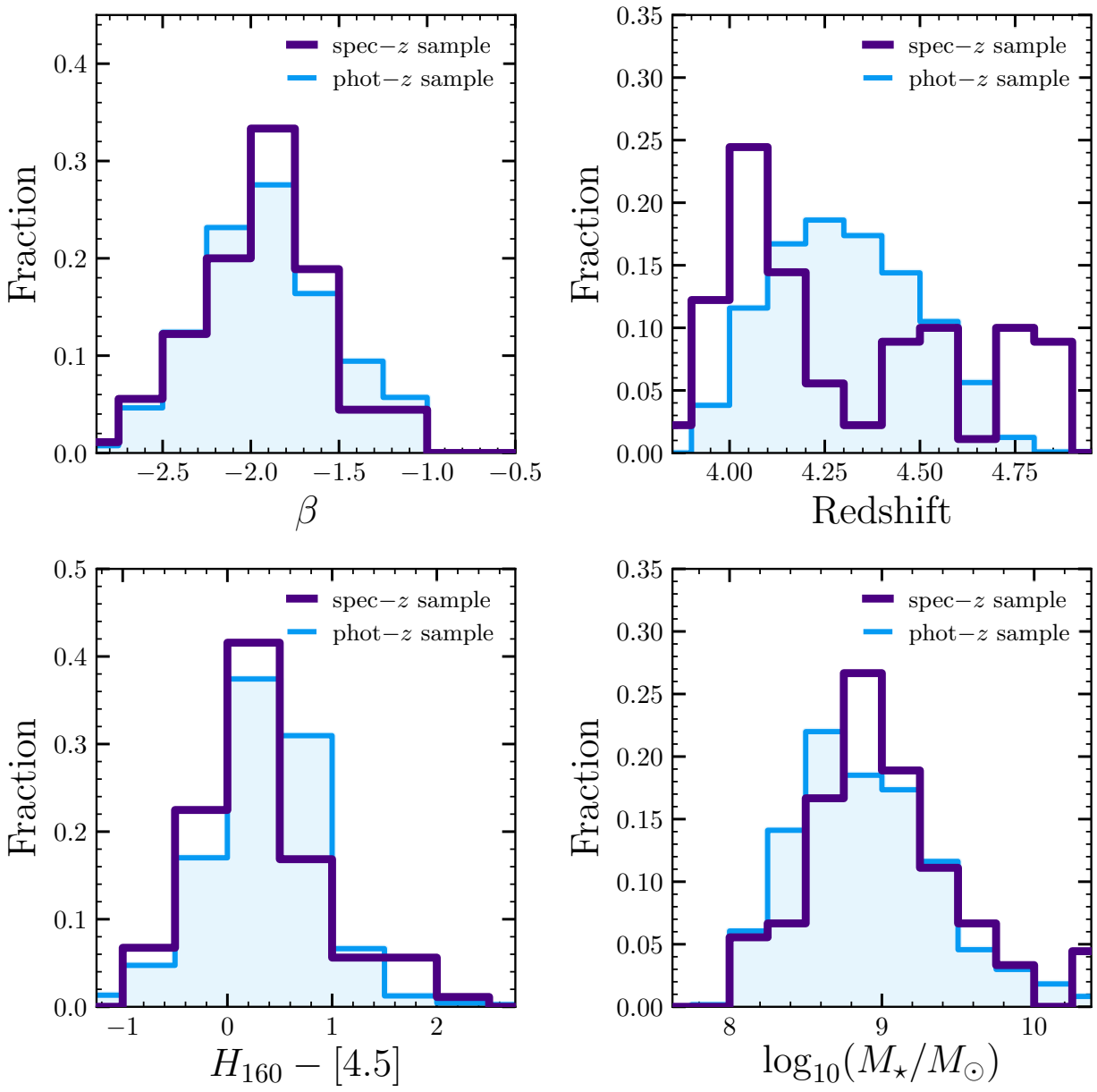

Figure 3.2: Comparison of the observational properties of our photo$-z$ sample (filled blue histograms) and our spec$-z$ sample (purple histograms) for the redshift selected sample at $z \sim 4.5$, both samples are normalized to the total number of objects in each category, so the integral of the area under the curve is 1. *Top left:* the UV-continuum slope β, defined as $f_\lambda \propto \lambda^\beta$, shows a similar distribution in both samples, with a median of -1.94 ($\sigma = 0.38$) for the photo$-z$ sample, and -1.92 ($\sigma = 0.36$) for the spec$-z$ sample. *Top right:* The redshift distribution of the two samples show differences, the median value of the spec$-z$ sample of 4.15 ($\sigma = 0.31$) is slightly less than the median value 4.30 ($\sigma = 0.19$) of the photo$-z$ sample. *Bottom left:* The $H_{160} - [4.5]$ color show a median value of 0.36 ($\sigma = 0.55$) for the photo$-z$ sample, and 0.25 ($\sigma = 0.66$) for the spec$-z$ sample. *Bottom right:* The distribution of stellar masses for the photo$-z$ and spec$-z$, with median values of 8.86 dex ($\sigma = 0.48$) and 8.95 dex ($\sigma = 0.48$) in $\log_{10} M_\star/M_\odot$, respectively. Despite these differences, there does not seem to be any significant bias between both the photometric and spectroscopic samples at $z \sim 4.5$.

Chapter 4

Hα measurements

The key to measuring the Hα flux through broadband photometry is to estimate independently the level of the underlying continuum. In the sections below we present the standard method that uses the excess between the best-fit spectral energy distribution and the flux measured from the photometry (Labbé et al. 2010, Mármol-Queraltó et al. 2016, Rasappu et al. 2016, Schaerer & de Barros 2009, Shim et al. 2011, Shivaei et al. 2015, Smit et al. 2016, Stark et al. 2013). As a check, we have also applied alternative methods to estimate the Hα flux. The first method interpolates the underlying continuum based on a sample of sources at a slightly lower redshift ($3.0 < z < 3.7$) for which IRAC colors are unaffected by line emission. The second method uses CIGALE to model the continuum and the nebular emissions to determine the flux of the Hα flux.

4.1. Spectral Energy Distribution Modeling

To estimate the stellar continuum at the wavelength of Hα, we use the code CIGALE (Code Investigating GAlaxy Emission Boquien et al. 2019) which models the spectral energy distribution of galaxies and estimates their physical properties. This code builds a composite stellar population from simple stellar populations and calculates the emission from gas ionised by massive stars based on the energy balance principle, i.e., the absorbed energy is re-emitted by dust in the mid− and far−infrared. We use CIGALE to fit synthetic stellar population models to the observed rest-frame UV to optical photometry. We excluded the [3.6] band photometry because of the potential contribution from nebular emission to ensure that what we estimate is the underlying continuum only. Figure 4.1 shows two samples selected in the redshift range $z = 3.86 - 4.94$, where the redshifted Hα emission line boosts the observed flux in the IRAC [3.6] band.

We performed SED fitting using fairly flexible star formation histories to accurately interpolate the stellar continuum flux at the wavelength of Hα. Briefly, we use the simple stellar population models from Bruzual & Charlot (2003) with a Chabrier (2003) IMF and we fixed the metallicity at $0.2Z_{\odot}$. The star formation histories (SFHs) were set to a double exponen-

tial with e-folding times of $\tau_{\rm main} = 150$ Gyr (essentially a constant SFH), and $\tau_{\rm burst} = 10$ Myr. The relative mass fraction of the late burst to the older population is allowed to vary between 0 and 0.95, and the ages of each exponential SFH are varied between 30 Myr and the age of the universe at the lowest redshift in the grid. This allows us to simultaneously fit fairly evolved (old) stellar populations as well as recent bursts. For internal reddening we used the Calzetti et al. (2000) attenuation curve, with the dust extinction allowed to vary between $E(B-V) = 0$ and $E(B-V) = 0.6$. To estimate the uncertainty of the flux at the wavelength of Hα, we run a set of 100 realizations, in which the input photometric measurements are perturbed according to their uncertainties.

Finally, the redshift grid is allowed to vary between $z = [2.5 - 5.5]$ for $B-$dropouts and between $z = [3.5 - 6.5]$ for $V-$dropouts. From these, we selected galaxies in the redshift window of $3.86 < z_{\rm phot} < 4.94$ (the $z \sim 4.5$ sample) for which the redshifted Hα falls in the measurement range of IRAC [3.6] band. Figure 3.1 shows a histogram of the redshifts for the $z \sim 4.5$ sample (blue). Figure 4.1 shows two SED examples with their respective best fits for an spec$-z$ sample (top) and a photo$-z$ sample (bottom). As explained above, open points are ignored in the SED fitting process to avoid nebular lines influencing our pure stellar fits.

4.2. Hα flux measurements

To estimate the Hα flux we compare the observed broadband photometry, which includes nebular emission, with that expected from the best-fit models produced by CIGALE in the [3.6] band using templates without nebular emission. We compare the observed photometry with the synthetic photometry from the models finding a systematic excess in the samples as shown in Figure 4.1. We determine the flux of a single gaussian at the wavelength of Hα that would reproduce the observed excess. In practice, the excess could also be produced with important contributions from [NII] and [SII] for which we will apply a correction later. To estimate uncertainties on the Hα fluxes, we perturb the observed photometry within error bars and adjusted the continuum level, we repeat the process 100 times, reporting the standard deviation as the 1σ uncertainty.

The flux excess measured in the [3.6] band at $z \sim 4.5$ is dominated by the contribution from Hα, [NII], and in some cases from [SII]. Adopting the ratios tabulated by Anders & Fritze-v. Alvensleben (2003) (see Table 1) for subsolar metallicity ($0.2Z_{\odot}$), we estimate the fraction of the total flux that corresponds to Hα. The $z \sim 4.5$ sample includes both $B-$ and $V-$dropouts, with different redshift distributions that determine which lines contribute to the broadband flux. For the $B-$dropouts, all three lines contribute to the [3.6] band, with Hα accounting for 84% of the flux, consistent with the value derived by Smit et al. (2016). $V-$dropouts, are at a higher redshift and we estimate that for $\sim$ 75% of them [SII] falls outside the [3.6] band (with an 80% confidence level). For the $V-$dropouts, then, we have only applied corrections considering the [NII] contribution to the [3.6] flux excess. In this

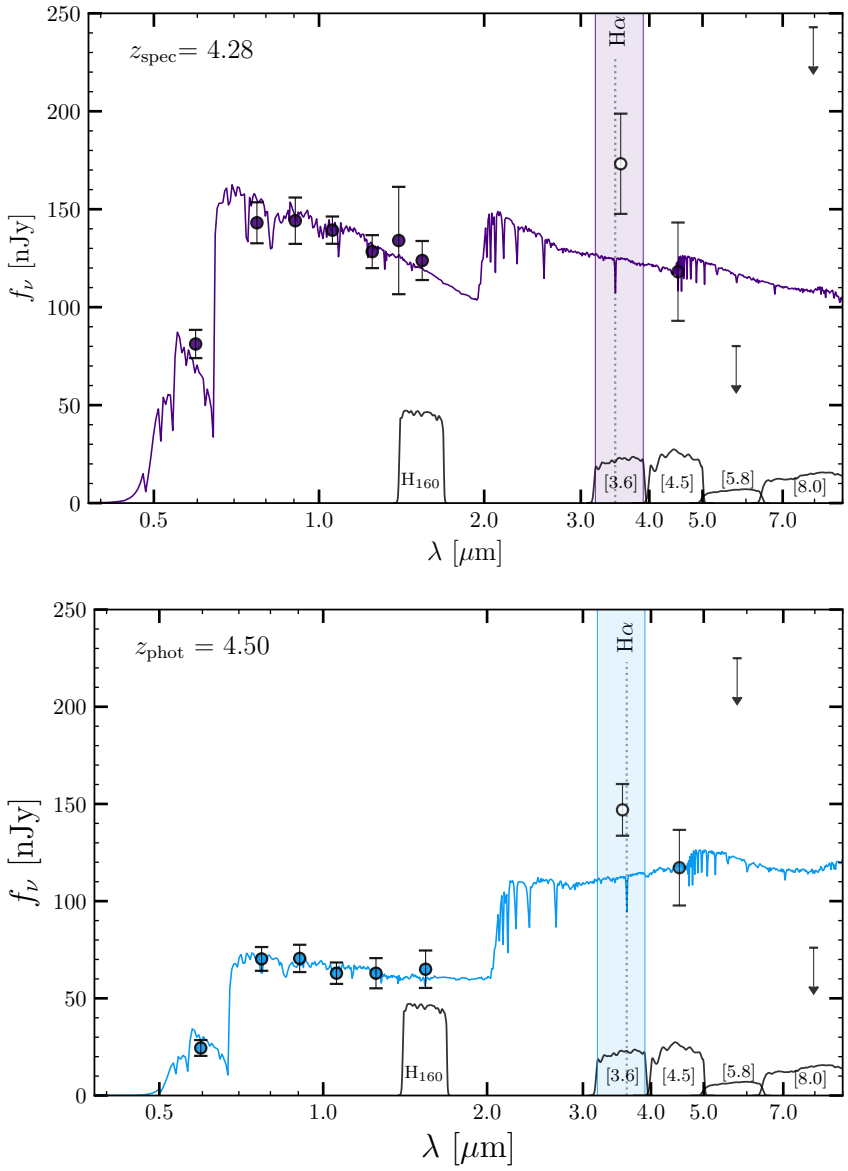

Figure 4.1: Broadband *HST*+IRAC photometry with their respective best-fit stellar population models for 2 sources in our sample. In each panel, the broadband observations are shown with filled symbols, except for the IRAC [3.6] band that is ignored in the fit to avoid the possible nebular contribution, which is an open symbol. Downward pointing arrows are 2σ upper limits. The top panel is a source with known spectroscopic redshift and the bottom panel is an example from the photometric sample. The redshifted wavelength of Hα is shown with the vertical dotted line, which falls in the range of the [3.6] IRAC band, whose wavelength range is shown by the shaded area (reference filter transmission curves are shown at the bottom of each panel). These two cases show a clear excess in the observed photometry compared to the underlying continuum of the best-fit model. This excess is primarily due to the contribution of the Hα line to the observed flux.

case, Hα accounts for 92% of the flux.

We convert the Hα flux into Hα Luminosity by the following equation:

$$L_{\mathrm{H}\alpha} = 4\pi \cdot D_l^2(z) \cdot F_{\mathrm{H}\alpha} \tag{4.1}$$

where D_l^2 is the luminosity distance, and $F_{\mathrm{H}\alpha}$ is the flux of the line. The luminosity distance was set according to the median redshift of the sample.

The equivalent width of the Hα line is estimated by dividing the Hα flux derived from the procedure described above by the continuum flux density at the wavelength of the Hα line,

$$\mathrm{EW}_0 = \frac{F_{\mathrm{H}_\alpha}}{(1+z) f_\lambda^{\mathrm{cont}}}, \tag{4.2}$$

where F_{H_α} is the flux of the line in and f_λ^{cont} is the flux density of the continuum at the wavelength of the redshifted Hα emission line. The distribution of the Hα rest-frame equivalent widths (EW$_0$(Hα)) are shown in Figure 4.2.

$\sim 41\%$ of the sample at $z \sim 4.5$ has observed IRAC photometry that is consistent with the synthetic best-fit SED photometry within $1\,\sigma$, i.e., they either do not have emission lines or their emission lines are too weak to be detected given the photometric uncertainties (see Section 4.3). A further 6% has observed photometry at [3.6] fainter than the continuum level by more than 1σ. Finally, $\sim 53\%$ of galaxies are detected at $> 1\sigma$ in F(Hα) for the $z \sim 4.5$ sample. We will call the estimates obtained by this method our fiducial Hα flux estimates.

4.3. Detection Limit

The median uncertainty in the [3.6] photometry corresponds to 5.63×10^{-22} [erg/s/Hz/cm^2]. When the flux excess between the observed photometry and the estimated underlying continuum is comparable to this uncertainty, it is impossible to reliably estimate the Hα flux. We derive a detection limit based on how faint the Hα flux of an object can be and still be detected by this indirect method.

Our method is as follows: we create synthetic photometry from perturbations of the best-fit SED model of each galaxy; then we add synthetic Hα lines to the photometry with fluxes, $F_{\mathrm{H}\alpha}$, logarithmically spaced ranging from 1.694×10^{-20} [erg/s/cm^2] to 1.694×10^{-15} [erg/s/cm^2]. The synthetic photometry that includes these emission lines with known fluxes is put through our pipeline to estimate Hα fluxes the same way it is done for the real sources. Finally, we compare the input Hα flux with the estimated value. The process is repeated 50 times per galaxy SED. We find that when $F_{\mathrm{H}\alpha} > 6.401 \times 10^{-18}$ [erg/s/cm^2] we recover the Hα flux with at least a 2σ significance 60% of the time. This is almost independent of the UV luminosity of the galaxy so we have adopted these as our reference detection limits.

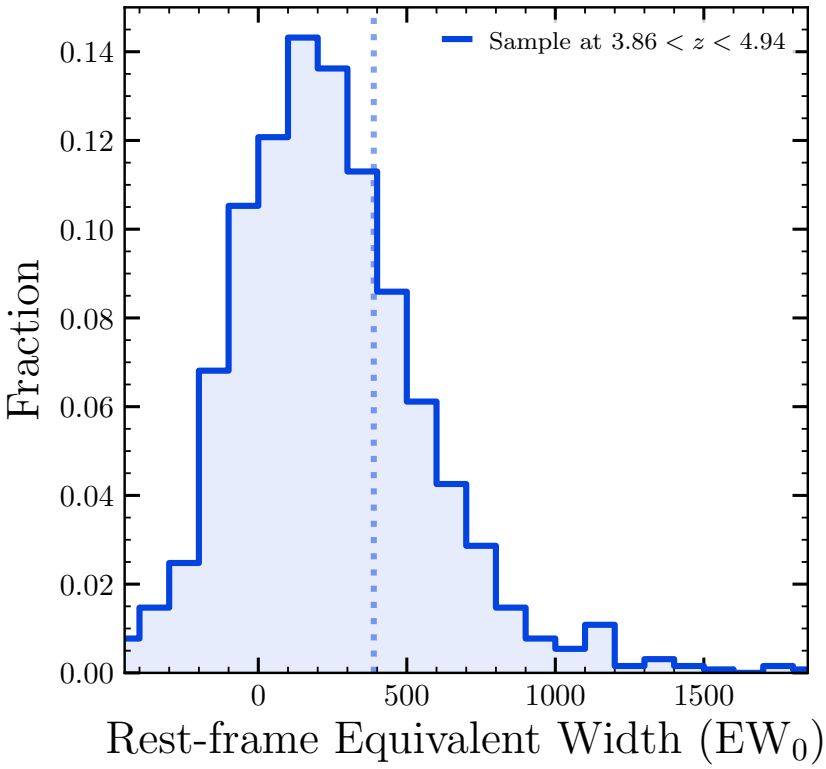

Figure 4.2: Hα rest-frame equivalent width distribution for the sample at $z \sim 4.5$ (blue shaded histogram) normalized to the total number of sources in the sample, so the integral of the area under the curve is 1. A 6% of the sample corresponds to negative values. Among the positive values with $S/N > 1$, the mean value is 388 Å (shown by the dotted vertical line).

4.4. Alternative Hα measurements

We propose a new method to derive the Hα flux from broad-band photometry that is independent of the SED modeling. The main idea of the method is to build a predictive model to estimate the rest-frame continuum level at 6563Å.

To estimate the continuum level we use, as a reference, galaxies whose redshift is in the range $3.0 \leq z \leq 3.7$, for which the IRAC 3.6μm measures the stellar continuum flux without a significant contribution from nebular emission, as left panel of Figure 4.4 shows. We select 279 sources with photometric redshift in this range (with $> 80\%$ probability). Based on these galaxies we train a model to predict the continuum level at 6563Å. The rest-frame optical SED is fairly flat and the redshift range is very close to the sample at $3.86 < z < 4.94$ as the right panel of Figure 4.4, so this is an appropriate reference. In essence, this model interpolates the stellar continuum at 6563Å using as reference a sample of galaxies at similar redshift without relying on SED fitting, as the magenta point of Figure 4.4 shows.

We then apply the model to the sample of galaxies for which [3.6] does include Hα contri-

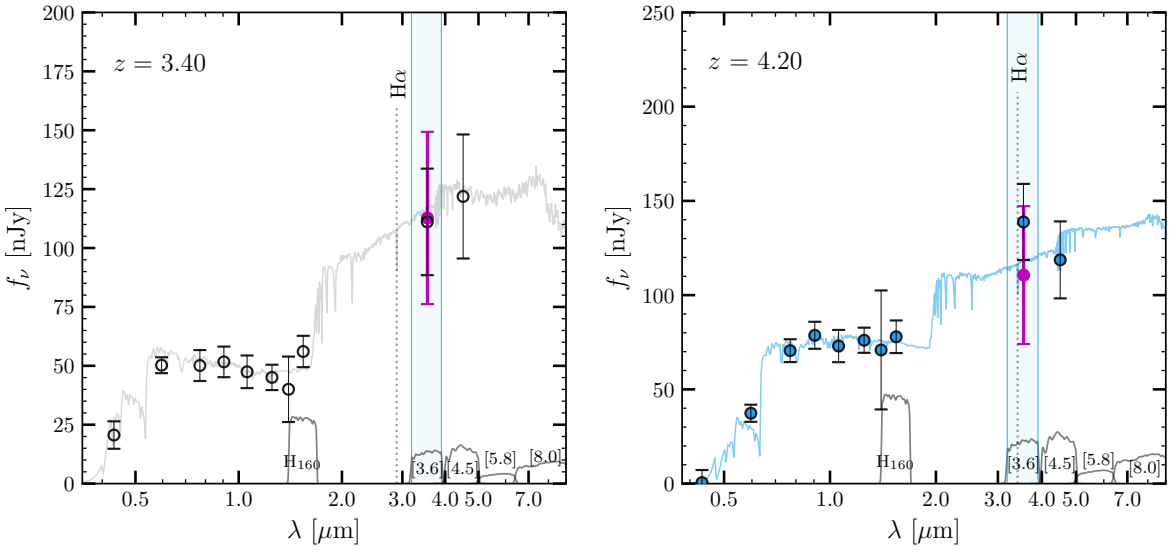

Figure 4.3: *Left*: The SED of a galaxy in the redshift range $3.0 < z < 3.7$ where no contribution of the Hα emission line is expected to be measured in the IRAC [3.6] band. The magenta point illustrates the estimation of the predictive model proposed and the gray transparent curve shows the level of the continuum estimated by CIGALE. The predictive model consistently estimates the flux measured at [3.6] as well as the continuum level estimated by CIGALE at that wavelengths. *Right*: The SED of a galaxy in the sample at $3.86 < z < 4.94$ is shown for comparison, where the [3.6] is affected by the presence of the Hα emission. After training the model, the continuum is estimated on this sample, obtaining the magenta point, then this offset allows us to measure Hα almost independently of the SED fitting.

bution and we measure the observed excess flux at [3.6] compared with the model prediction, as the right panel of Figure 4.4 shows in the magenta point. The following model is proposed:

$$f_{3.6}(f_{4.5}, f_{\rm UV}, \beta) = A \cdot \frac{f_{4.5}^2}{f_{\rm UV}} + B \cdot \beta \cdot f_{4.5} + C \cdot f_{\rm UV} \cdot f_{4.5} + D \cdot f_2 \tag{4.3}$$

Where $f_{3.6}$ is the flux density at 3.6μm which we want to predict, $f_{4.5}$ is the observed flux density at 4.5μm, $f_{\rm UV}$ is the rest-frame flux at 1600Å, and β is the UV-continuum slope from the fit $f_\lambda \propto \lambda^\beta$. A, B, C, & D are the free parameters of the model.

We train the predictive model with 80% of the clean sample and then we test the value of the flux at [3.6] with the remaining 20%. To estimate the error of the model we iterate this procedure 100 times, perturbing the parameters within their associated uncertainties.

We use the flux excess at [3.6] for galaxies at $3.86 < z < 4.94$ and repeat the same procedure to calculate the Hα as described in Section 4.2, including the same corrections to account for [NII] and [SII] in the [3.6] band.

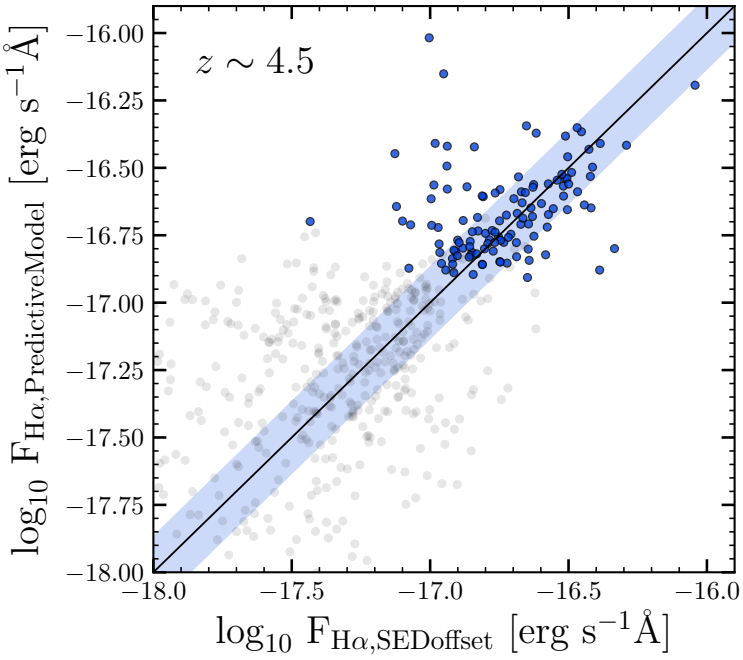

Figure 4.4: Hα fluxes derived from the predictive model vs. the fiducial estimates used throughout, based on the offset between the observed photometry and the best-fit SED. Blue points have 2σ significance, and the rest of the gray points have less than 2σ significance, but they still follow the same trend as the other points. Both methods are consistent on average, with a scatter of 0.13 dex (see text) that is comparable to the typical uncertainties. This shows that the Hα flux estimates used throughout do not depend strongly on the details of the SED fitting procedure.

Figure 4.4 shows the comparison between the fiducial estimates used in this work (based on the stellar continuum estimated with CIGALE, horizontal axis), and the method described above (vertical axis). The black line is identity for reference. Only sources detected with $> 2\sigma$ significance are shown as filled blue points, and the rest of the grey points have $< 2\sigma$. We find no systematic offsets between the two estimates but there is considerable scatter. Focusing only on sources with $> 2\sigma$ Hα fluxes, the scatter of the relation is 0.13 dex (median absolute deviation), with 14.3% of outliers ($> 2\times$ MAD). This scatter is comparable to the mean uncertainty of our Hα estimates. These results suggest that the Hα flux estimates used throughout do not depend strongly on the details of the SED fitting procedure and that the uncertainties are not significantly underestimated. The success of the proposed predictive model makes use of characteristic properties that may present some levels of correlation for galaxies selected as LBGs, and cannot be extrapolated for galaxies based on other selection methods.

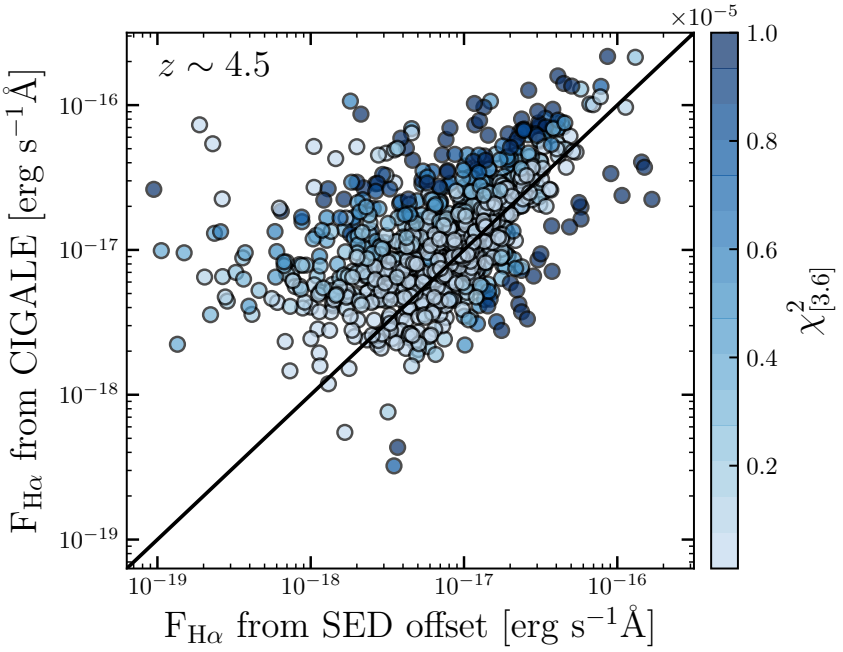

Figure 4.5: Comparison between our fiducial Hα fluxes and the ones derived from SED modeling with CIGALE including nebular emission. Color code represents the value of χ^2 in the [3.6] band from where we estimate the Hα flux. This quantity reveals how well the best-fit model reproduces actual photometry in each band.

4.4.1. Modeling the Nebular Emission with CIGALE

CIGALE can also produce models that include the nebular emission (both continuum and lines, Stark et al. 2013) so we also produced SED fits that use all the photometry and fits synthetic models with nebular emission. These models can directly output the best-fit Hα flux for each galaxy. We consider an ionization parameter $\log \mathrm{U} = [-3.5, -2.0]$ in steps of 0.1, and all other parameters in the grid of models are identical as in the previous fits.

Figure 4.5 compares our fiducial Hα flux estimates used throughout with those produced by CIGALE using models that include nebular emission. Overall, the comparison shows significant scatter and a systematic offset such that CIGALE estimates produce slightly higher Hα fluxes. Interestingly, the bigger the discrepancy, the higher the χ^2 of the best-fit model (as shown by the color-coding of the points in Figure 4.5). This probably suggests that most of the discrepancy is a result of the difficulty of the models to reproduce the Hα EWs suggested by the broad-band photometry.

Chapter 5

The Hα Luminosity Function

The luminosity function (LF) is one of the most direct observables to study galaxies since it measures the volume density as a function of luminosity. It allows us to explore how evolves the abundance and luminosity distribution of galaxies over cosmic time. To characterize the star formation rate of galaxies at $z \sim 4.5$ we will make use of Hα as a tracer of star formation. This is similar to what can be done with the UV luminosity function (UV LF) at this redshift (Bouwens et al. 2015) but since dust grains preferentially absorb more light at shorter wavelengths, Hα should be a more direct estimate, less sensitive to the uncertainties associated with dust extinction.

The parent sample of this thesis was used to derive the UV LF at $z \sim 4$ and $z \sim 5$, using the V_{max} method of Avni & Bahcall (1980) for independent samples, based on Schmidt (1968) which assigns a representative volume to each galaxy. We adopted the comoving volumes of Bouwens et al. (2015) which already consider the incompleteness in UV detection due to the fact that faint galaxies may sometimes be lost in the image noise. Under this method, the luminosity function is calculated according to the following equation:

$$\Phi(M) \cdot \mathrm{d}M = \sum_i \frac{1}{V_i} = \frac{\Delta N}{\Delta V}. \tag{5.1}$$

To estimate the Hα LF, we start with the same V_{max} volumes associated with each galaxy to estimate the UV LF. This volume depends only on their M_{UV} and redshift. Because we have made extra cuts to the sample (e.g., cuts based on IRAC S/N, quality of the SED fit), we need to correct the V_{max} volumes used. We rescale the volumes by the ratio between the number of sources in our sample and that in the parent sample by Bouwens et al. (2015), so even after all the cuts, we recover the same UV LF. If the cuts made to the sample were homogeneously distributed in UV luminosity, we should be able to recover the same UV LFs with our final sample (with larger uncertainties due to using fewer objects). However, we could also expect certain cuts to have a significant impact on the luminosity distribution. For example, fainter sources may have more uncertain redshifts and be more affected by our

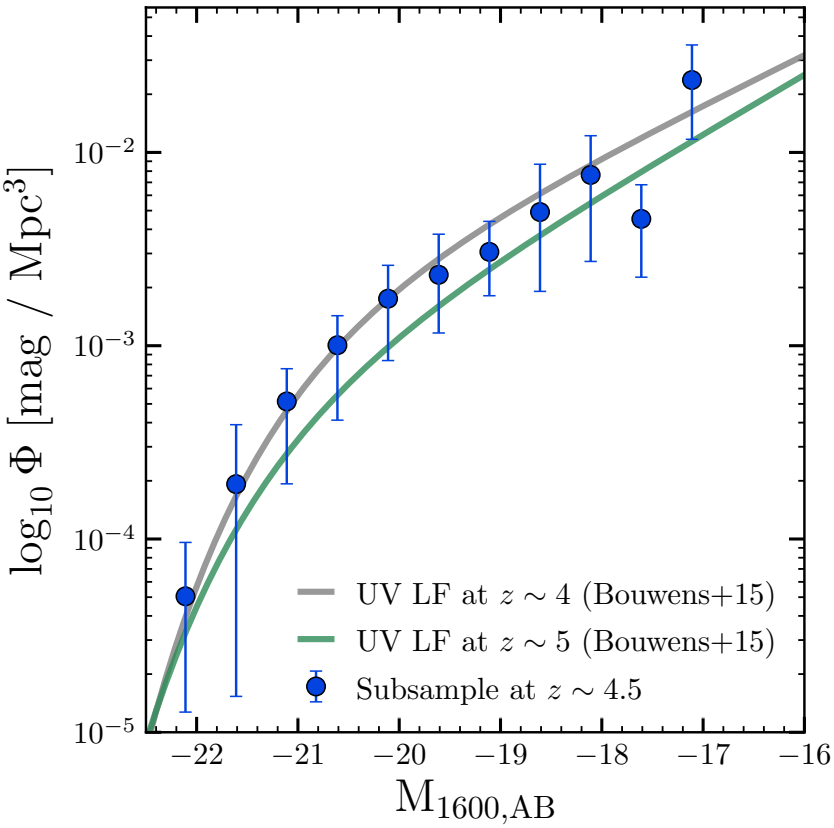

Figure 5.1: UV Luminosity function for the selected sample at $3.96 < z < 4.94$ with 1299 objects (blue filled points), corresponding to the UV LF recovered after adjusting correction factors for the given volume. The solid gray line is the original UV LF at $z \sim 4$ with 5712 sources, and the solid green line is the original curve at $z \sim 5$ that contains 1862 sources from Bouwens et al. (2015).

redshift cut.

We have verified that our final sub-sample reproduces the UV LFs by Bouwens et al. (2015) at $z \sim 4$ and $z \sim 5$. To do this, we have split our sub-samples according to their selection as either $B-$ or $V-$dropouts. While applying the $V_{\rm max}$ method, we have adjusted the volumes in each magnitude bin to correct for the cuts made in the analysis (see Chapter 3). We assume that all missing objects in the same magnitude bin cover the same volume in every field. We do this separately for the photometric quality cuts and for the redshift cuts. As a result, the V_{max} method is modified to account for these corrections as follows:

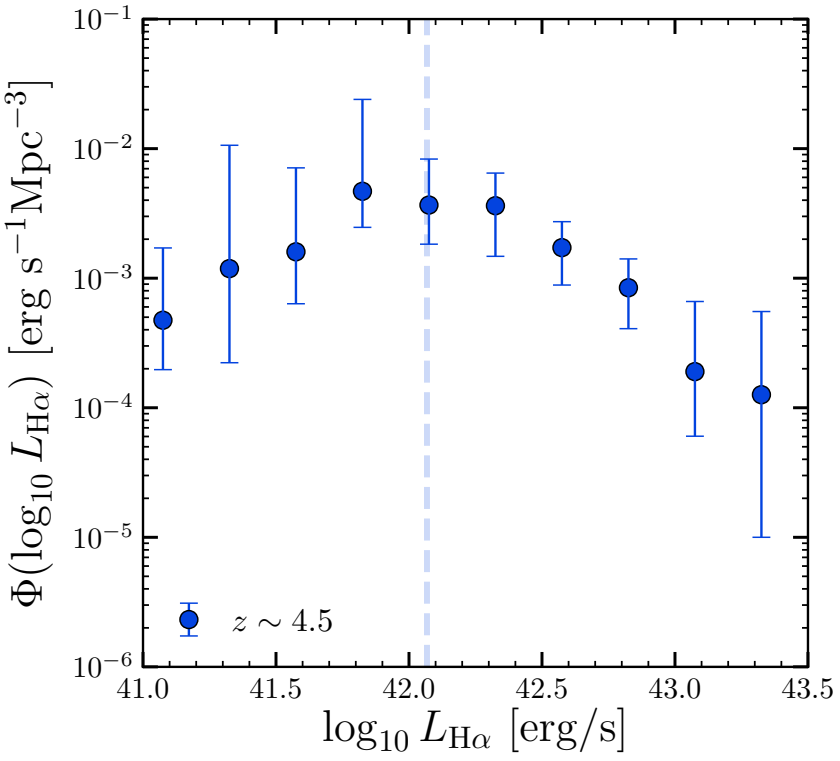

Figure 5.2: Hα Luminosity Function for the sample at $z \sim 4.5$ represented with blue points. The vertical dashed line show the detection limit derived as explained Section 4.3. It can be noticed that below the detection limit the Hα LF decreases due to the incompleteness of the measurements in the faint end. We correct this incompleteness in Section 5.1.

$$\begin{aligned}\Phi(M) \cdot \mathrm{d}M &= \sum_{i}^{\text{Full Sample}} \frac{1}{V_i} \\ &= \sum_{i}^{\text{Clean Sample}} \frac{1}{V_i} \times f_q \\ &= \sum_{i}^{z-\text{selected Sample}} \frac{1}{V_i} \times f_q \times f_z,\end{aligned} \tag{5.2}$$

where f_q represents the correction factor for the photometric quality selection explained in Section 3.1 and f_z represents the cut in redshift given by the probability that these sources have detectable Hα emission in [3.6] is greater than 80%. The final correction factors per bin of M_{UV} are shown in Table 5.1.

Figure 5.1 shows UV LF that results from our final sample at $3.96 < z < 4.94$, where B-dropouts and V-dropouts are combined, together with the Schechter parameterizations of the UV LFs at $z \sim 4$ and $z \sim 5$ by Bouwens et al. (2015). They are in very good agreement,

Table 5.1: Correction factors $f_q \times f_z$ per field [a]

$M_{\rm UV}$ [b]	GSWB	GSDB	GNWB	GNDB	ERSB	XDFB
−22.94	–	–	–	0.5	–	–
−22.44	0.5	0.1	0.1	–	–	–
−21.94	0.1	4.3	2.1	9.3	2.9	–
−21.44	3.6	3.0	1.9	3.6	2.8	–
−20.94	2.3	2.6	1.9	2.4	2.7	3.0
−20.44	3.1	2.7	2.9	2.2	2.9	3.3
−19.94	4.0	4.0	3.8	3.2	5.0	3.8
−19.44	12.4	7.1	7.3	5.9	9.2	4.8
−18.94	17.6	55.2	29.5	97.0	136.0	5.6
−18.44	–	–	–	–	–	16.0
−17.94	–	–	–	–	–	15.3
−17.44	–	–	–	–	–	67.0
$M_{\rm UV}$	GSWV	GSDV	GNWV	GNDV	ERSV	XDFV
−22.86	–	1.0	1.0	–	–	–
−22.36	–	1.0	–	–	1.0	–
−21.86	8.0	0.4	0.1	8.0	–	–
−21.36	6.0	5.0	21.9	3.7	5.0	–
−20.86	9.0	4.6	25.0	8.6	6.0	–
−20.36	5.6	7.4	16.8	9.3	7.9	–
−19.86	9.0	14.2	15.4	15.3	8.7	–
−19.36	–	12.2	34.0	20.6	44.0	5.0
−18.86	–	12.7	–	44.5	10.0	6.6
−17.86	–	–	–	–	–	64.0
−16.86	–	–	–	–	–	30.0

NOTE— [a] There are no correction factors when the final sample has no selected sources in that bin.
[b] Some factors in the $B-$dropout sample are $f_z < 1$ because we merge the photo$-z$ and spec$-z$ sample. As a result, some bins have more objects than the original LBG sample to recover the UV LF from Bouwens et al. (2015).

especially considering the slightly different redshift ranges and the reduced sample size. This same method, which reproduces the UV LFs, is the one used to estimate the Hα luminosity functions in Chapter 5.

We produce the Hα LFs by binning the estimated $\log_{10} L(\mathrm{H}\alpha)$ [erg/s] in bins of 0.25 dex and applying equation 5.1 (with the corrected V_{max} volumes) to each bin. The results are shown in Figure 5.2 and Table 5.2. The detection limits calculated in the previous section are shown as vertical dashed lines. We can see that below the detection limit there is a potential problem of completeness, where the luminosity function decays, inverting its faint-end slope.

This incompleteness could be caused by our increasing inability to measure Hα among the faintest galaxies. We attempt a correction to this incompleteness in Section 5.1.

5.1. The Faint-end of the Hα Luminosity Function

Below the detection limit, the volume corrections due to incompleteness become too large and uncertain and we do not apply them. Rather, to estimate the shape of the Hα LF below this limit, we exploit the empirical relationship between $M_{\rm UV}$ and $L_{\rm H\alpha}$ (Figure 5.3, Top). Our approach uses the UV LF at $z \sim 4$ as a probability density function (PDF) to draw a sample of $M_{\rm UV}$ values in the range $-22.7 < M_{\rm UV} < -16.8$. First, we can compute an empirical Hα luminosity function, in the same way that previous studies have done by bootstrap resampling (e.g., De Barros et al. 2019, González et al. 2011). This empirical Hα LF is very consistent with the obtained by the V_{max} method even at low luminosities, actually showing the same problem of incompleteness in the faint-end slope. Secondly, we can make use of the linear fit of the $M_{\rm UV} - L_{\rm H\alpha}$ relation by randomly choosing a source with a similar $M_{\rm UV}$ (within 0.5 mags), and taking the Hα flux estimated by the Bayesian linear regression shown in the top panel of Figure 5.3. The result of this Monte Carlo (MC) experiment is the blue histogram in the bottom panel of figure 5.3. As can be seen in the figure, this method yields a LF that is consistent with the one derived through the V_{max} method for Hα luminosities above the detection limit. Below the detection limit, these two estimates diverge, as the MC method is not affected by the measurement incompleteness at low luminosities.

In a different approach, we use the Schechter parameterization of the UV LF at $z \sim 4$ and combine it with a linear fit of the $M_{\rm UV} - L_{\rm H\alpha}$ relation. This way, we can analytically derive the faint end slope assuming a Schechter parameterization (see, e.g., González et al. 2011). For the linear fit, we follow a Bayesian approach in which we take into account the uncertainties on both variables, assume a constant intrinsic scatter, and allow for the possibility of outliers in the sample (see Hogg et al. 2010). We model the non-detections using the Kaplan-Meier non-parametric estimator. The result of this approach is shown in Figure 5.3, Bottom, with a magenta line. It can be seen that this approach results in an estimate of the faint end slope that is very consistent with the MC method described above.

This way, we derive the values of the faint-end slope, α, independently of the V_{max} method (see Table 5.3).

5.2. Schechter Parameters

The Hα luminosity function can be fitted with a Schechter function as Figure 5.4 shows, which in the logarithmic form is:

$$\Phi(L)\mathrm{d}L = \ln(10)\phi^* \left(\frac{L}{L^*}\right)^{\alpha+1} e^{-(L/L^*)} \mathrm{d}\log_{10} L \tag{5.3}$$

Table 5.2: Values of the Hα LF at $z \sim 4.5$

log $L_{H\alpha}$ (erg s^{-1})	$\Phi_{H\alpha}$ obs[a] (10^{-3} Mpc^{-3})	$\Phi_{H\alpha}$ corr[b] (10^{-3} Mpc^{-3})	N
42.075	$4.04^{+2.47}_{-1.45}$	$3.67^{+4.64}_{-1.84}$	216
42.325	$3.24^{+1.82}_{-1.36}$	$3.63^{+2.85}_{-2.15}$	235
42.575	$1.48^{+0.83}_{-0.66}$	$1.72^{+1.01}_{-0.83}$	144
42.825	$0.34^{+0.77}_{-0.26}$	$0.84^{+0.56}_{-0.43}$	83
43.075	$0.07^{+0.53}_{-0.07}$	$0.20^{+0.47}_{-0.13}$	26
43.325	$0.06^{+0.07}_{-0.04}$	$0.12^{+0.42}_{-0.11}$	9

NOTE—[a] From the observed Hα luminosity, [b] from the dust-corrected Hα luminosity

with parameters : α, ϕ^* and L^*.

During the fit, the α parameter is fixed to the value calculated according to the process explained above in Section 5.1. To find the other best-fit parameters, a Monte Carlo simulation was performed. We take 1000 random values from the simulation of the Hα LF and adjust the parameters using a least-square method. The parameters ϕ^* and L^* were allowed to vary freely. The Hα LF with its Schechter fit is shown in Figure 5.4. Each parameter with its error bar is reported in Table 5.3.

Table 5.3: Schechter parameters of the Hα LF

z	$\log_{10} L^*_{H\alpha}$ (erg s^{-1})	$\Phi^*_{H\alpha}$ ($10^3 Mpc^{-3}$)	$\alpha_{H\alpha}$
	Observed		
4.5	$43.08^{+0.17}_{-0.29}$	$0.29^{+0.69}_{-0.11}$	$-1.83^{+0.07}_{-0.09}$
	Dust Corrected		
4.5	$43.21^{+0.18}_{-0.31}$	$0.24^{+0.76}_{-0.10}$	$-1.76^{+0.07}_{-0.08}$

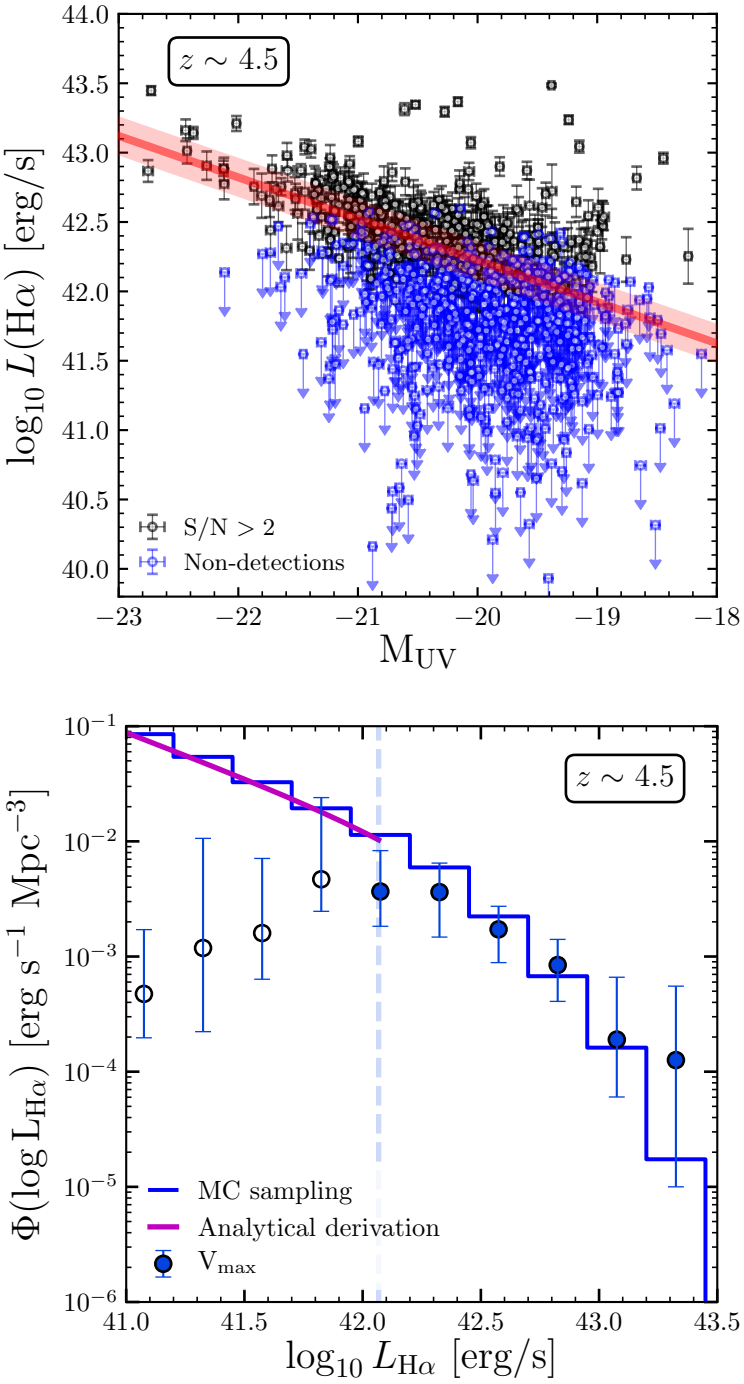

Figure 5.3: *Top*: The relationship between Hα Luminosity and M_{UV}. Black points (measurements) and blue symbols with arrows (2σ upper limits) are used to fit a Bayesian linear regression. The outliers and the intrinsic scatter were also considered in the modeling. The red line corresponds to the maximum a posteriori and the shaded region represents the intrinsic scatter. *Bottom*: The Hα LF derived from the V_{max} method (blue points), from the Monte Carlo (MC) empirical sampling (blue histogram), and from the analytical derivation of the faint-end slope using the linear regression described above (magenta solid line). The detection limit is shown by the vertical dashed line.

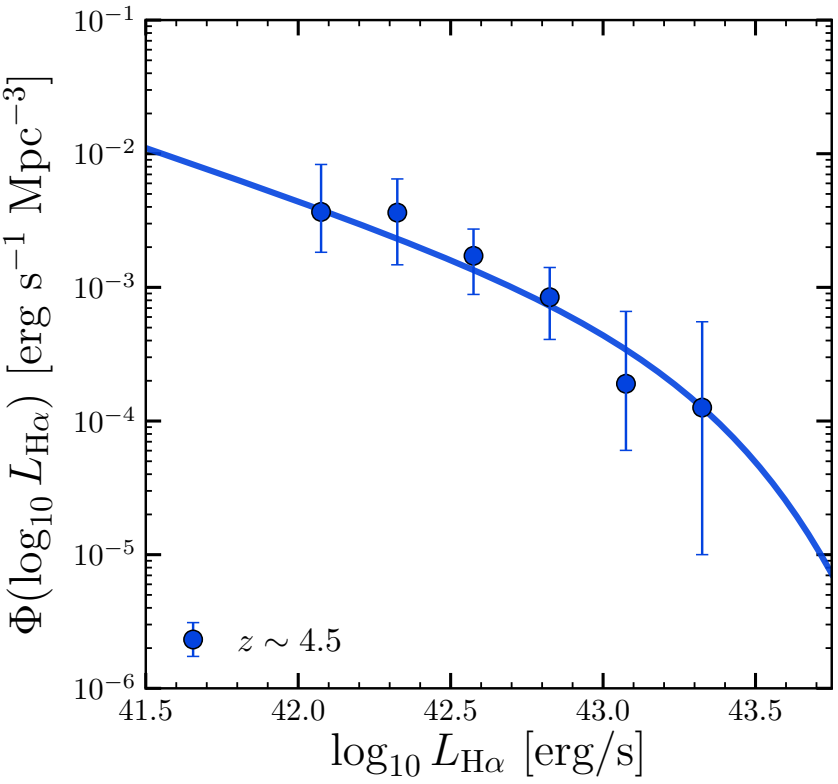

Figure 5.4: Hα LF found for the sample at $z \sim 4.5$, derived from dust-corrected luminosities (see Section 6.1 for further details about dust corrections). Schechter parameterization of the data with the α parameter fixed is done. The parameters Φ^* and L^* are allowed to vary and are shown in Table 5.3.

Chapter 6

Star Formation Rate Functions

The star formation rate (SFR) of galaxies is difficult to estimate, especially at high redshift, where the rest-frame UV is typically the only tracer readily available. UV light is strongly affected by dust extinction, which means that fairly large corrections need to be made to estimate the intrinsic UV luminosities before a conversion can be made into SFR. In this section, we will estimate SFRs from the UV luminosity of our sources and we will compare them to estimates derived from the Hα luminosities derived in previous sections. Dust extinction at the wavelength of Hα can be $\sim 3\times$ lower than in the UV (assuming, e.g., a Calzetti et al. 2000 attenuation curve), which may make these estimates less uncertain.

6.1. Dust Corrections

Both, the rest-frame UV luminosity and the Hα luminosity of a galaxy can be used to estimate its SFR. Their intrinsic values, however, are not directly observable, as dust, a key component of the interstellar medium (ISM), absorbs a significant fraction of the light emitted from the rest-UV to the near-infrared (NIR). To estimate the intrinsic UV and Hα luminosities we must first estimate the effects of dust.

During the SED fitting procedure, which was necessary to estimate the stellar continuum at the wavelength of Hα (see Section 4.1), dust extinction was already included in the modeling of the observed SEDs. In this case we assumed a Calzetti et al. (2000) attenuation curve, and allowed the color excess to vary between $E(B-V) = 0 - 0.6$. Similar to previous works we assumed that nebular lines have the same extinction as the stellar continuum, i.e., $E(B-V)_{nebular} = E(B-V)_{stellar}$ (e.g., Shim et al. 2011, Shivaei et al. 2015, Smit et al. 2016, but see also Calzetti 1997). We can use the results of the modeling to apply corrections to both the UV and Hα luminosity. While this type of correction makes use of all the SED information, it is also subject to known degeneracies intrinsic to the models, in particular, the degeneracy between the age of the main stellar population and the total extinction. This means that, sometimes, galaxies with similar SED may end up with very

different dust extinction corrections if the best-fit models prefer considerably different ages. Moreover, metallicity can also affect the shape of the continuum, but in a less pronounced way.

We used the dust extinction calibration proposed by Meurer et al. (1999a), which is a widely used method, to estimate the dust extinction at 1600 Å, in magnitudes by:

$$A_{1600} = 4.43 + 1.99 \cdot \beta \tag{6.1}$$

where β is the UV continuum slope (see Section 3.2.3). To estimate the dust extinction at all other wavelengths, we use the following expression:

$$A(\lambda) = E(B-V) \cdot \kappa(\lambda) \tag{6.2}$$

where for $\kappa(\lambda)$, we use the Calzetti attenuation curve (Calzetti et al. 2000).

For the $z \sim 4.5$ sample, using the expressions 6.1 and 6.2 the mean correction factor in the UV (1600 Å) is 1.99, and for Hα it is 1.2.

So far, we have used the UV slope β to estimate A_{1600} using the Meurer et al. (1999a) relation and the Calzetti et al. (2000) attenuation curve. Independently, we also estimate the dust correction while doing the SED modeling with CIGALE (see Section 4.1). We aim to explore the consistency between both dust correction estimates. Figure 6.1 shows the comparison between the Hα luminosities were corrected using the two different extinction values. CIGALE estimates of the dust corrections are slightly higher, resulting in intrinsic Hα luminosities that are on average 1.3× higher.

6.2. Star Formation Rates

From the intrinsic UV and Hα luminosities, we derive the star formation rates. We transform the intrinsic UV luminosity into SFR following the transformation by Kennicutt (1998a), scaled by a factor 1.8 to consider a Chabrier (2003) initial mass function (IMF):

$$\mathrm{SFR_{UV}}(\mathrm{M_\odot yr^{-1}}) = 0.77 \times 10^{-28} L_{\mathrm{UV}}(\mathrm{erg\ s^{-1}Hz}) \tag{6.3}$$

where L_{UV} is the intrinsic UV luminosity measured at 1600 Å.

Similarly, we estimate SFR from the intrinsic Hα luminosity following Kennicutt (1998a):

$$\mathrm{SFR_{H\alpha}}(\mathrm{M_\odot yr^{-1}}) = 4.4 \times 10^{-42} L_{\mathrm{H\alpha}}(\mathrm{erg\ s^{-1}}) \tag{6.4}$$

where $L_{\mathrm{H\alpha}}$ is the intrinsic Hα luminosity and the conversion also assumes a Chabrier (2003) IMF.

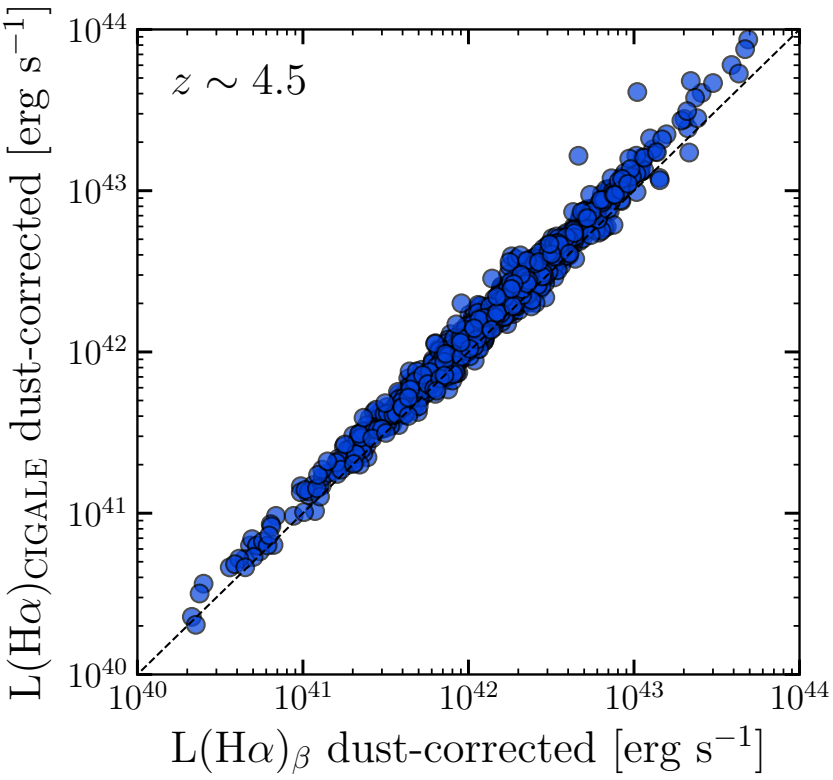

Figure 6.1: Hα luminosities dust-corrected using CIGALE best fit model compared to the fiducial Hα luminosities used throughout which are based on the (Meurer et al. 1999a) relation. CIGALE-based corrections result in Hα luminosities on average 1.3× higher.

Figure 6.2 shows the comparison between the SFR derived based on the Hα luminosity, $SFR_{H\alpha}$, and the one derived using the rest-frame UV, SFR_{UV}. The horizontal line represents our estimated completeness limit (see Section 5.1), and the same level is represented by the vertical line to avoid any potential bias. The values that are below these limits are represented as gray points, the blue solid line represents the Bayesian linear regression including possible outliers and intrinsic scatter, which results in the equation shown in the bottom right of the figure. While these SFR estimates are well correlated, there are clear systematic differences between them even ignoring the gray-out points. The origin of these differences is unclear and may stem from multiple factors such as the star formation histories (bursty star formation histories depending on mass), metallicity trends, and variations in the attenuation curves, among others that will be further discussed in Chapter 7. In the following section, we will focus on the SFRs derived using the Hα to estimate the SFR function at $z \sim 4.5$.

6.3. Star Formation Rate Function at $z \sim 4.5$

We derive the star formation rate function at $z \sim 4.5$ with the same method used to derive the Hα LF. We bin our estimates of $SFR_{H\alpha}$ in bins of $\log_{10}(SFR_{H\alpha}) = 0.25$ dex and adopt

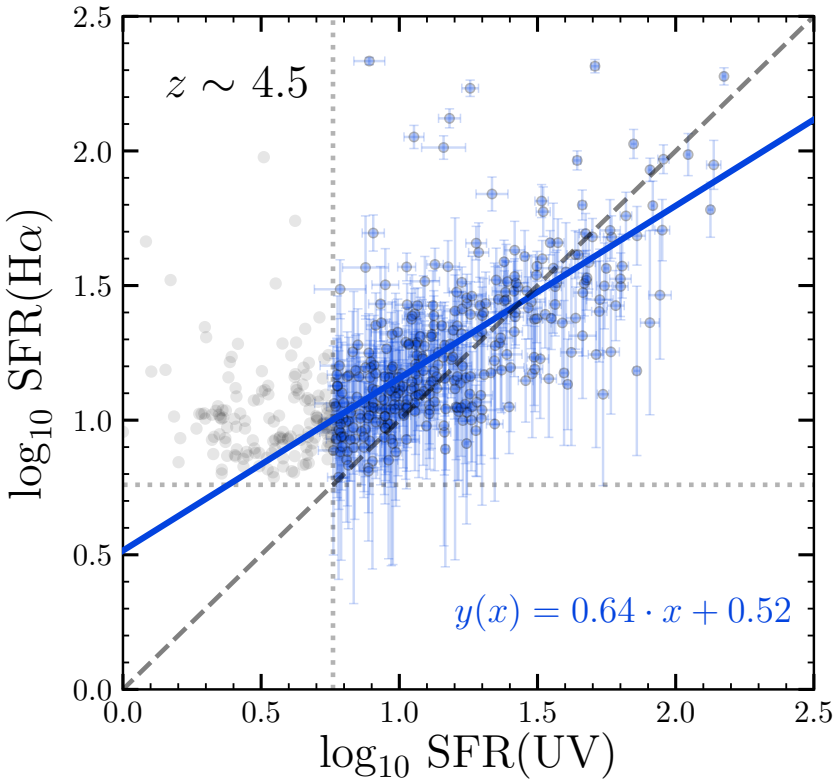

Figure 6.2: Star formation rate derived from the Hα luminosity in the y axis vs. those derived from UV luminosity in the x axis. Both luminosities were dust-corrected using the Calzetti et al. (2000) attenuation law and the IRX-β relation (Meurer et al. 1999b). The dashed black line is the one-to-one relation, and the blue solid line shows the Bayesian linear regression (including possible outliers) and intrinsic scatter (equation shown in the bottom right).

Table 6.1: Values of the SFR Function at $z \sim 4.5$

log SFR ($M_\odot$ yr^{-1})	Φ_{SFR} (10^{-3}Mpc^{-3})	N
1.125	$2.45^{+1.46}_{-1.03}$	205
1.375	$0.92^{+0.73}_{-0.53}$	89
1.625	$0.41^{+0.82}_{-0.30}$	44
1.875	$0.15^{+0.18}_{-0.15}$	13
2.125	$0.12^{+0.46}_{-0.09}$	5

the same volumes used above to build the Hα LF (see Section 5). Then, we build the SFR Function with the V_{max} method (Equation 5.1). Uncertainties were computed assuming a Poissonian error associated with the number of objects per bin.

To determine the completeness limit in SFR, we use our detection limit in $L_{H\alpha}$, apply the

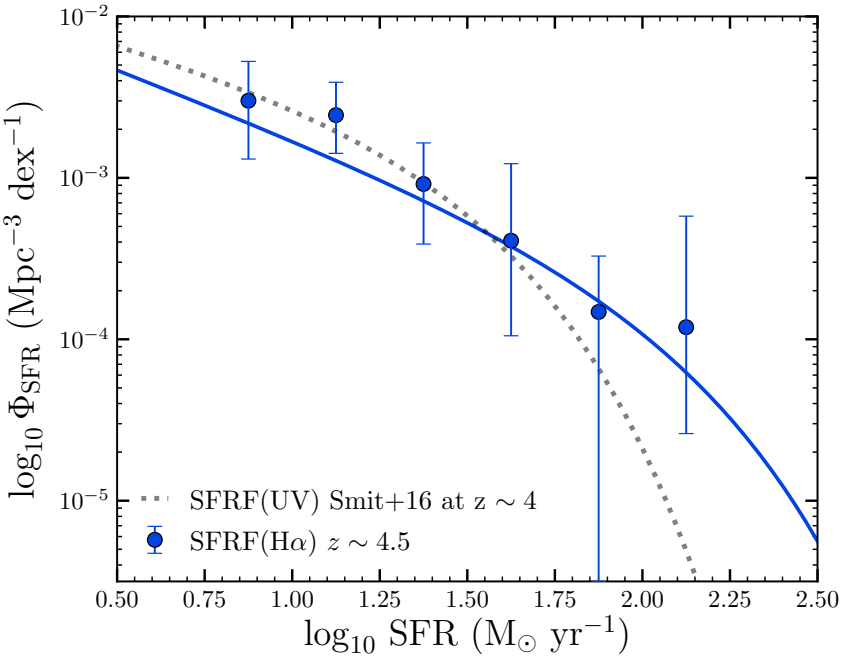

Figure 6.3: Star Formation Rate function at $z \sim 4.5$ derived following the procedure described in Section 6.3. The SFR function is based on Hα luminosity function and we assume Kennicutt (1998a) conversion from Hα to SFR with a correction for a Chabrier (2003) IMF. It was calculated from the stepwise dust-corrected SFR function with the analytical solution for the Schechter function (Smit et al. 2012). Schechter function was fitted with the least-square method considering the errors associated with each measurement and with a fixed value of the faint-end slope derived from the Hα Luminosity Function. Also, the SFR function derived from the UV at $z \sim 4$ by Smit et al. (2016) is shown as reference.

mean dust correction factor for sources of that brightness, and convert it into $\mathrm{SFR_{H\alpha}}$ using Equation 6.4. It is possible to measure SFR as low as 5.82 $\mathrm{M_\odot yr^{-1}}$, ensuring that objects are effectively detected at least with a 2σ significance 60% of the time.

To estimate the behavior of the SFR function below the completeness limit above, we use the prescription presented by Smit et al. (2012). We perform stepwise determinations to correct Hα luminosity in the same way that Smit et al. (2012) corrected the UV luminosity. An analytical Schechter-like approximation is used to represent the SFR functions derived from the dust-corrected Hα luminosity function using the relation between A_{1600} and β. We do not consider a scatter for the relationship between A_{1600} and β, then the slope in the faint-end is obtained directly from the luminosity function and the proper dust correction.

Figure 6.3 shows the Hα SFR function at $z \sim 4.5$ in the blue points. Similarly to what was done for the Hα LF, we fit the Schechter function to the SFR function with parameters $\Phi^*_{\rm SFR}$, SFR*, and α; shown in the blue solid line of Figure 6.3. We use a simple least square

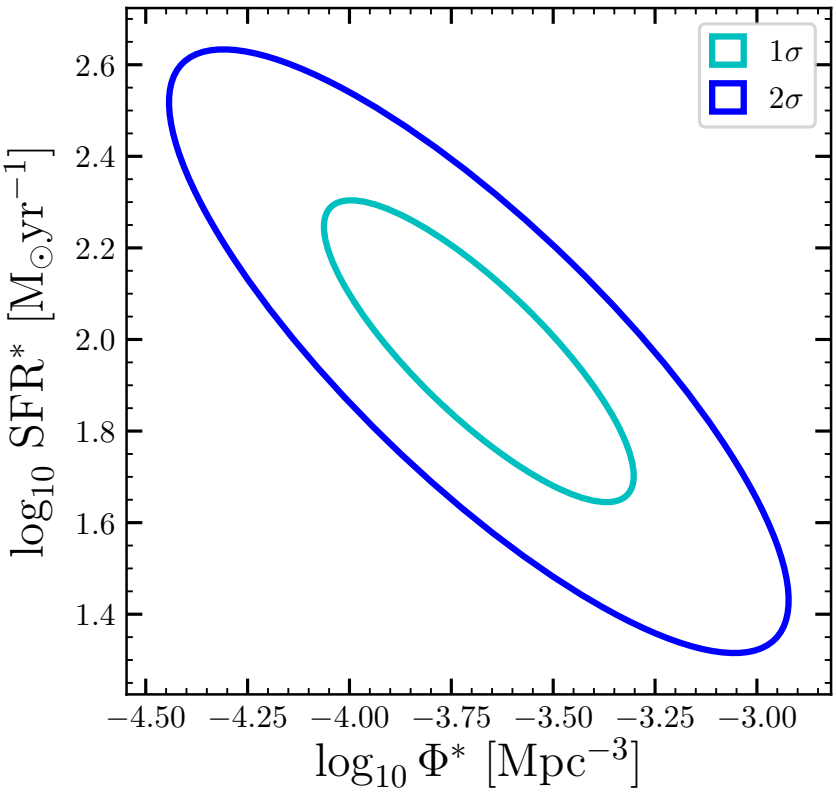

Figure 6.4: The 68% and 95% confidence intervals on the Schechter parameters Φ^* and SFR^* we derive for the SFR function at $z \sim 4.5$. As the faint-end slope α was fixed, it is not possible to build the contours with the other parameters.

method where we fix α to the value calculated as explained above. We allow for parameters Φ^*_{SFR} and SFR^* to vary freely and their 68% and 95% confidence intervals are shown in Figure 6.4. The values are also listed in Tables 6.1 and 6.2. For comparison, we added the SFR function estimated from UV luminosities from Smit et al. (2016) in Figure 6.3 shown as a dotted line.

6.4. The SFRD evolution

The cosmic SFH of the Universe shows significant scatter (Madau & Dickinson 2014) depending on the tracers used to estimate SFR. Because of observational constraints, at high redshift, most estimates rely on the rest-frame UV to estimate SFR. Here we present the SFR density based on the Hα luminosity at $z \sim 4.5$.

To compare our Hα based estimates at this redshift with previous UV-based estimates, we attempt to keep the same luminosity restrictions as in previous works. In particular, we integrate the SFR down to a magnitude limit $M_{\mathrm{UV}} = -17$ AB mag (Bouwens et al. 2015).

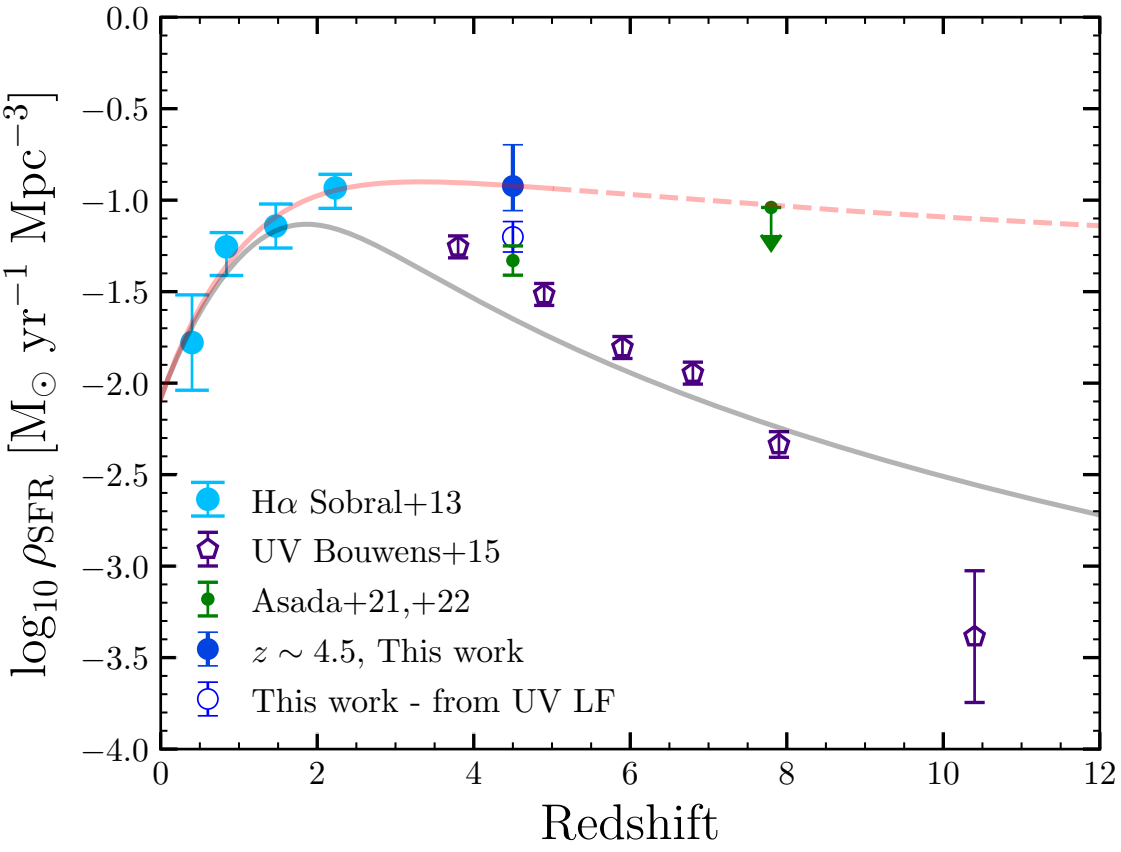

Figure 6.5: Cosmic evolution of the star formation rate density (SFRD). Our Hα-based estimate at $z\sim4.5$ is shown by the solid blue circle. For comparison, we also show rest-UV based estimates for our sample (open circles). For context, we show $z\lesssim2.5$, Hα-based SFRD estimates by Sobral et al. (2013) ($z=0.08, 0.4, 0.84, 1.47, 2.23$). At $z>2.5$ there are mainly UV-based SFRDs so here we show estimates from Bouwens et al. (2015) at $z=3.8, 4.9, 5.9, 6.8, 7.9$. Also Asada et al. (2021) present estimations based on the rest UV to optical using SED fitting at $z\sim4.5$, and at $z\sim7.8$ Asada & Ohta (2022) measure the SFRD from the Hα luminosity function. All SFRD estimates are made considering galaxies brighter than $M_{\rm UV}=-17$, except for the case of Sobral et al. (2013) the integration is consistent with $M_{\rm UV}=-18$. The figure also shows the functional fit for the cosmic evolution of the SFRD reported by Madau & Dickinson (2014) converted into the Chabrier IMF, which is primarily based on UV and IR estimates (gray solid line). Our fit to the Hα-based SFRD estimates is shown in red.

In practice, we convert this magnitude limit into a SFR limit by applying the mean dust correction for that luminosity and using Equation 6.3. This translates into limits of SFR = 5.82 $M_\odot$/yr. We integrate the Schechter functional forms presented in 6.3. Uncertainties were estimated via Monte Carlo, sampling the parameters of the Schechter functions within their uncertainties.

Our estimate of the Hα SFRD at $z\sim4.5$ is shown in Figure 6.5 (blue filled point). As a

Table 6.2: Schechter parameters of the SFR Function

z	$\log_{10}$ SFR* ($M_\odot yr^{-1}$)	Φ^*_{SFR} ($10^{-3}Mpc^{-3}$)	α_{SFR}	$\rho_{SFRH\alpha}$ ($M_\odot yr^{-1}Mpc^{-3}$)
4.5	$2.03^{+0.32}_{-0.53}$	$0.11^{+0.57}_{-0.01}$	$-1.76^{+0.07}_{-0.08}$	$0.12^{+0.18}_{-0.08}$

comparison, we also calculated the SFRD for our sample from the UV luminosity, obtaining the blue open point shown in Figure 6.5. The SFRD from Hα is 0.28 dex higher than the SFRD obtained from UV. The parameterization proposed by Madau & Dickinson (2014) of the cosmic SFH is shown by the grey curve. The values adopted by Madau & Dickinson (2014) were mainly derived from UV and IR measurements. Here we fit a new curve that only considers Hα-derived SFRDs using our new estimate at $z \sim 4.5$ combination with those by Sobral et al. (2013) at $z \lesssim 2.5$. This new fit is shown by the red solid line and the further extrapolation is shown as a red dashed line.

Chapter 7

Discussion

In this section, we discuss our findings regarding the evolution of the Hα equivalent width, and the evolution of the Hα luminosity function as a function of redshift. We also discuss the impact of different assumptions on our estimates of the star formation rate of individual galaxies and on our estimate of the star formation rate density over cosmic time.

7.1. Evolution of the Hα Equivalent Width

While there seems to be an agreement in that the specific star formation rate (sSFR = SFR/$M_{stellar}$) of galaxies declines over cosmic time, it has been difficult to reconcile theoretical estimates of this decline with observations (e.g., Damen et al. 2009, Fumagalli et al. 2012, Guo et al. 2011). At the highest redshifts, the sSFR is usually estimated through SED modeling but because Hα is a standard indicator of the SFR, the Hα equivalent width (EW(Hα)) can also be related to the sSFR. Studying the evolution of the EW(Hα) may be a good alternative to evaluating the evolution of the sSFR over redshift independent from SED modeling.

Fumagalli et al. (2012), used data from the 3D-HST survey (Brammer et al. 2012, Skelton et al. 2014) to measure the EW(Hα) from $z \sim 0$ to $z \sim 2$ and found a dramatic growth with redshift EW(Hα) $\sim (1+z)^{1.8}$ for stellar masses in the range of $10^{10-10.5}$. Mármol-Queraltó et al. (2016), however, extended the EW(Hα) measurements to $z \sim 4.5$ using the SED-fitting technique with photometry and spectroscopy of the UDS and GOODS-S fields provided by the public CANDELS and 3D-HST spectroscopic survey, and found a slower evolution EW(Hα) $\sim (1+z)^{1.0}$ for star-forming galaxies with stellar masses $\simeq 10^{10}$ $M_{\odot}$. Their estimates at $z \sim 4.5$ are significantly lower than those reported by Shim et al. (2011), which they argue is due to the improved quality of their K_s-band data. Other studies have also found estimates below those reported by Shim et al. (2011). In particular Stark et al. (2013) estimate at $z \sim 5$ is very consistent with that by Mármol-Queraltó et al. (2016) but they are both slightly lower than the estimates presented by Smit et al. 2016. This seems to be explained by the lower stellar masses (~ 0.9 dex) in the latter works. Controlling by mass seems to produce more consistent results.

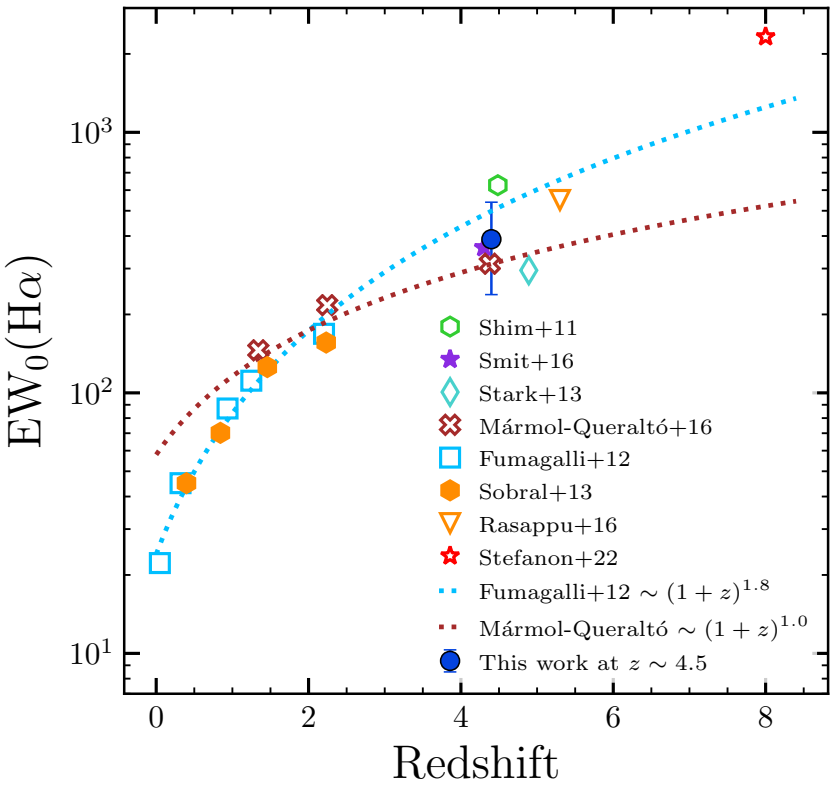

Figure 7.1: Evolution of EW(Hα) with redshift. The filled blue point represents our median EW(Hα) measurements for the sample at $z \sim 4.5$. Results from other Hα studies are shown for comparison (Fumagalli et al. 2012, Mármol-Queraltó et al. 2016, Rasappu et al. 2016, Shim et al. 2011, Smit et al. 2016, Sobral et al. 2013, Stark et al. 2013, Stefanon et al. 2022). The dotted lines show the evolution of this quantity proposed by Fumagalli et al. (2012), for the stellar masses range given by $10^{10-10.5}$ and $S/N > 3$ data of their work (light blue curve), and by Mármol-Queraltó et al. (2016) (red curve).

Our work extends the estimates of the EW(Hα) to $z \sim 4.5$ using the latest *Spitzer*/IRAC data. Figure 7.1 shows our median value of EW(Hα) in the context of previous measurements. We find an EW(Hα) value that is very consistent with those of Smit et al. (2016) and Mármol-Queraltó et al. (2016) at $z \sim 4.5$. This may be expected given the similar mass ranges considered ($\simeq 10^{8.5-9.5} M_\odot$). Our measurements, however, do not allow us to distinguish between the faster evolution estimated by Fumagalli et al. (2012) and the slower one proposed by Mármol-Queraltó et al. (2016), as they are formally consistent with both.

7.2. Evolution of the Hα Luminosity Function

Sobral et al. (2013) studied the evolution of the Hα LF using deep and wide narrow-band filters from the High-redshift (Z) Emission Line Survey (HiZELS) survey at $z = 0.4$, 0.84,

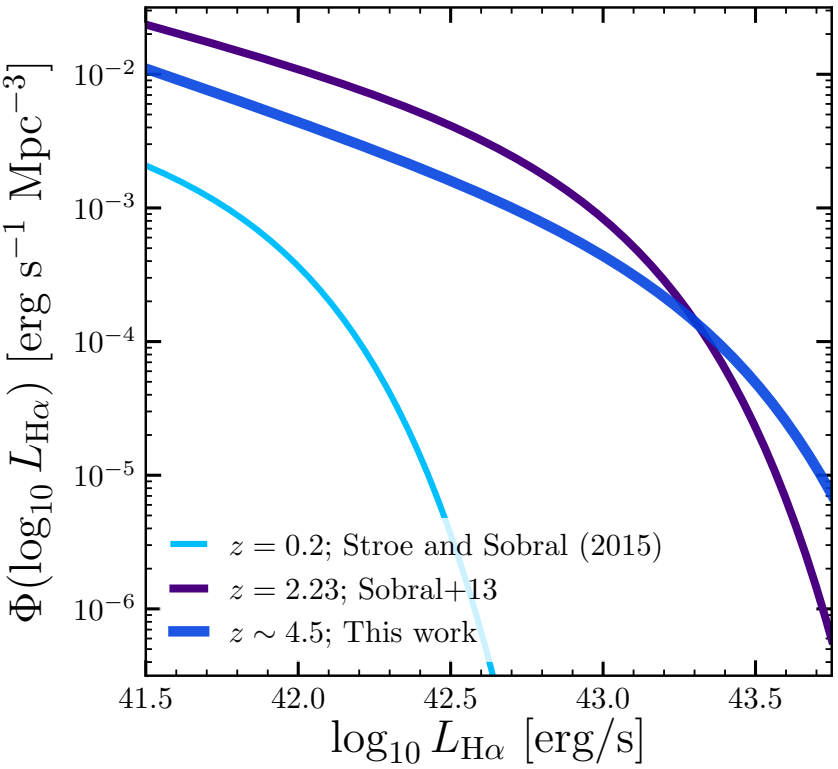

Figure 7.2: Our Hα LF (Schechter fits) at $z \sim 4.5$ compared to the Hα LF by Sobral et al. (2013) at $z \sim 2.2$. The Hα LF at $z = 0.2$ presented by Stroe & Sobral (2015) is shown as a representative reference of the local universe. There is a clear evolution of the normalization factor of the LF, also the "knee" of the function changes according to redshift, and the faint-end slope does not show a clear evolution.

1.47 and 2.23. Here we can extend the study of the Hα LF evolution to $z \sim 4.5$.

Figure 7.2 compares our best fit Schechter function at $z \sim 4.5$ with the $z = 2.23$ LF by Sobral et al. (2013). While the $z = 2.23$ Hα LF is above the others at the faint end ($< 10^{43} L_{\mathrm{H}\alpha}$), it seems that bright Hα (strong emitters and likely higher SFRs) are more common at the highest redshifts. In terms of the evolution of the best-fit Schechter parameters, Figure 7.3, we find that the normalization factor, Φ^*, continues to decrease toward higher redshift, consistent with its behavior at $z > 1$. In fact, shows a decreasing behavior from $z = 0.84$ to 4.5 by a factor ~ 14. In the case of L^*, the evolution shows a steady increase with redshift up to $z \sim 4.5$ as shown in the middle panel of Figure 7.3. Finally, the evolution of the faint-end slope, $\alpha_{\mathrm{H}\alpha}$ is shown in the bottom panel of Figure 7.3. In this case, our value does not come from a Schechter fit but a power-law fit based on our Monte Carlo method (see Section 5.1). $\alpha_{\mathrm{H}\alpha}$ shows a fairly constant value as a function of redshift, although the value at $z \sim 4.5$ may be slightly lower than all $z < 3$ estimates, implying that the Hα LF may be steeper at the highest redshifts.

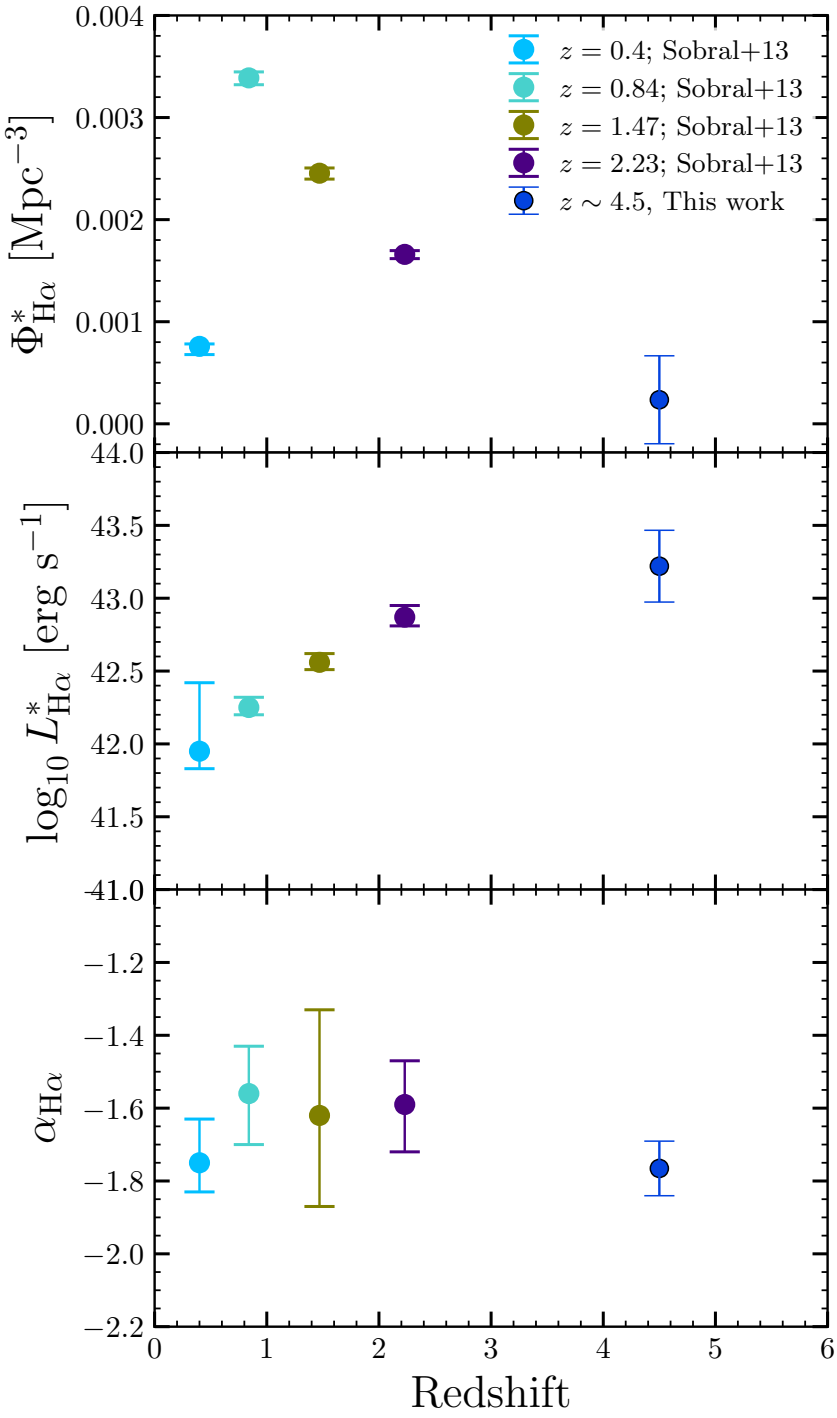

Figure 7.3: The evolution of the Schechter best-fit parameters for the Hα LF since $z \sim 4.5$. Top panel: the evolution of Φ^* shows a decrease with redshift from $z \sim 1$. Middle panel: the evolution of $L^*_{\mathrm{H}\alpha}$ shows a consistent increase up to $z \sim 4.5$. Bottom panel: the faint-end slope shows a fairly flat behavior as a function of redshift.

7.3. Differences between SFR(Hα) and SFR(UV)

In this work, we have derived SFRs both from UV luminosities and from Hα fluxes (see Section 6.2). Hα-based SFRs are sensitive to changes in the recent star formation history (SFH) and can change in relatively short timescales of 10 Myr. UV SFRs, on the other hand, depend on the luminosity of slightly lower mass stars and so they are more representative of the SFR over the past $\sim$ 100 Myr. If the SFHs are changing over timescales comparable to $\sim$ 10 Myr, we can expect these two SFR estimates to differ, and in fact, we may learn about the variability of the SFHs of galaxies based on these differences.

Previous studies have evaluated the relationship between UV-derived SFRs and Hα-derived SFRs finding differences between both indicators. Atek et al. (2022), for example, compared the SFR_{UV} with the $SFR_{H\alpha}$ in low-mass ($< 10^9$ $M_\odot$) galaxies at $0.7 < z < 1.5$. They find that these low-mass galaxies have an excess in $SFR_{H\alpha}$ compared to SFR_{UV} and that they also tend to have higher EW(Hα). They also find that the excess becomes larger toward lower masses. This could suggest that the SFHs of lower mass galaxies are more "bursty". Similarly, Faisst et al. (2019) analysed a sample of galaxies at $4 < z < 5$ and based on statistical arguments concluded that a galaxy at this redshift has experienced on average $1 - 4$ major bursts.

Smit et al. (2016) also reports excess in Hα-derived SFRs compared with UV-derived SFRs at $3.8 < z < 5.0$ but they argue that bursty SFHs may not be the best explanation for their sample. They find that a simple model that adds bursts to the SFH of galaxies may reproduce the excess in $SFR_{H\alpha}$ but it would also create a fraction of sources with low sSFR(Hα) that are not seen in their data.

Figure 7.4 shows, for our galaxies, the comparison between SFR(Hα) and SFR(UV). The horizontal line show our estimated completeness limit (see Section 5.1). Galaxies with SFR below this limit could be detected in UV but would not be detected in Hα unless they have a significant excess in SFR(Hα) compared to SFR(UV). This would bias the comparison and make the SFR(Hα) excess look particularly strong at the lowest values of SFR(UV). This can be seen in the gray points in Figure 7.4. Even ignoring these grayed-out points below the detection limit, however, there is an interesting trend in the SFR(Hα)/SFR(UV) ratio. At the highest SFRs (log(SFR(UV) > 1.5), SFR(Hα) is consistently lower than SFR(UV), indicating that their SFRs may be declining in the last 10 Myr. On the other end, for the lowest SFRs that we can measure, SFR(Hα) is enhanced compared to SFR(UV). This may indicate that they are more likely to be experiencing a burst at the time of observation, or that their SFHs are more typically rising. Because SFR is correlated with $M_{stellar}$, this could mean that lower mass systems tend to have more bursty SFHs, as suggested by Atek et al. (2022), but the rising SFHs are also consistent. This change between (on average) rising SFHs at low mass to declining SFHs at the highest masses is consistent with the behavior shown in the

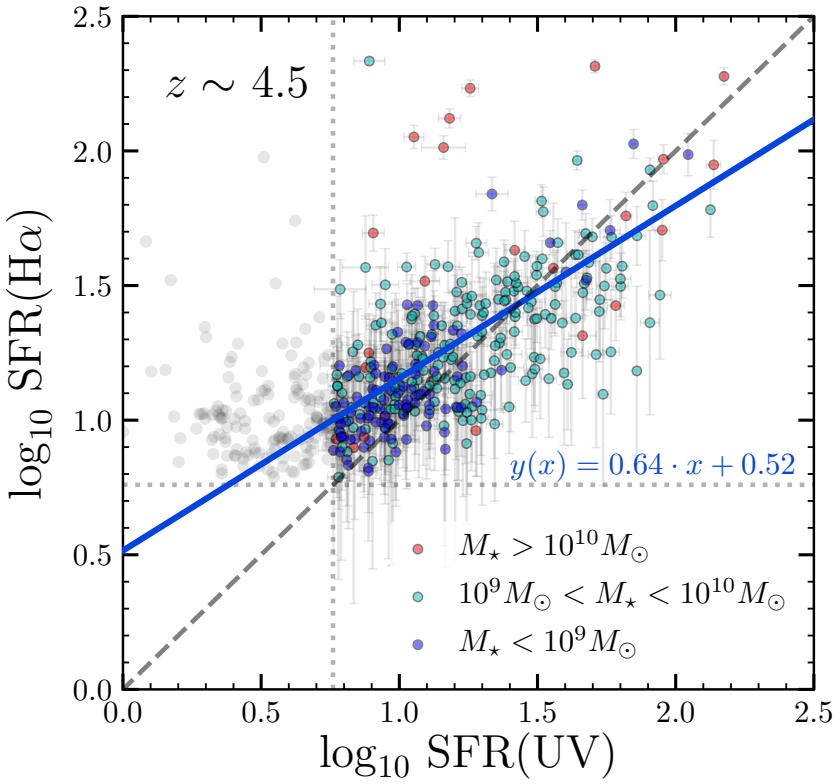

Figure 7.4: Star formation rate derived from the Hα luminosity vs. those derived from UV luminosity. Color coded by the range of stellar mass indicated in the legend. The dashed black line is the one-to-one relation, and the blue solid line shows the Bayesian linear regression (including possible outliers) and intrinsic scatter (equation shown in the bottom right). This figure is the same as the Figure6.2 but color coded by ranges of stellar mass

semi-analytic simulation by Tacchella et al. 2018. Our data, however, also show significant scatter on this trend, especially among the most massive galaxies ($M_{stellar} > 10^{10} M_\odot$). For intermediate and low mass galaxies the behavior seems more consistent.

Unfortunately, it is not so straightforward to derive conclusions regarding the SFH of galaxies is based on the differences between SFR(Hα) and SFR(UV), as there are other factors that can affect these SFR estimators. For example, Ly et al. (2016) suggests that at one-fifth solar metallicity, the conversion to SFRs from Hα is ~ 0.2 dex lower than the Kennicutt (1998a) relation that we used. We find that this factor is not enough to balance SFR_{UV} and $SFR_{H\alpha}$.

Another important factor affecting the comparison could be the differential dust attenuation factor between stellar continuum and nebular emission, which has been reported to be $A_{nebular} = 0.4 A_{continuum}$ (e.g., Calzetti et al. 2000). Other recent studies at $z \sim 2$, however, do not find a significant difference between the dust attenuation for stellar continuum and

for nebular emission (Shivaei et al. 2015) which may depend on the metallicity (Shivaei et al. 2020). Nevertheless, for this effect to explain our observed trend in SFR(Hα)/SFR(UV) ratio without the necessity to invoke changes in the SFHs, they would have to also be dependent on SFR or stellar mass. For example, differential dust attenuation between stellar continuum and nebular emission would have to become larger as a function of increasing SFR. This would bring the slope of the SFR(Hα)-SFR(UV) relation closer to 1 but it would still mean that SFR(Hα) is higher than SFR(UV) at all SFRs.

Finally, there is the possibility that the attenuation curve is different from the Calzetti et al. (2000) assumed here. For example, previous studies have explored the possibility of a steeper attenuation curve in high-z galaxies (e.g., Shivaei et al. 2020, 2015, Smit et al. 2016). Smit et al. (2016) concluded that if high-z, UV-selected galaxies had an SMC-type dust law, the Hα fluxes observed would be too high to be explained without a stronger source of ionizing radiation. We find that testing an SMC attenuation law in our galaxies (Gordon et al. 2003), does not resolve the tension between SFR(Hα) and SFR(UV) either, unless the steepness of the dust attenuation law is also dependent on SFR or stellar mass. This is also true with even steeper laws.

7.4. Cosmic Star Formation Rate Density History

By integrating the SFR functions presented in Section 6.3 we can estimate the SFR density (SFRD) of the Universe at $z \sim 4.5$ based on SFR(Hα). The limit adopted for the integral should be consistent with previous UV based estimates at $z > 3$ ($M_{UV} < -17$, see Section 6.4). As can be seen in Figure 6.5, Hα based estimates are systematically higher than the UV based estimates at all redshifts. The estimates presented at $z < 3$ are derived from the Hα LFs presented by Sobral et al. (2013) and using the same conversions used in this work at $z \sim 4.5$. At $z \sim 4.5$ Asada et al. (2021) estimate the SFRD from SED fitting showing an excess compared to that estimated from the UV LF by ~ 0.25 dex. However, our estimates from the UV LF with our selected sample are larger than the value they report.

Because we have worked with a sub-sample of the original $B-$ and $V-$dropouts from the work by Bouwens et al. (2015), we have tested if our sample is consistent with their SFRD trends. We find a very good agreement at $z \sim 4.5$ shown in the blue open point of Figure 6.5.

As discussed in the previous section, individual Hα based SFRs are lower than UV based estimates at high values of SFR but the opposite is true at the lowest SFRs. Due to the steepness of the SFR functions, the low SFR sources dominate the numbers, which explains why the integral results in SFRD(Hα) being higher than the SFRD(UV) when integrated into the ranges used in Figure 6.5.

Similar to Madau & Dickinson (2014), we have fit all the SFRD(Hα) values from $z \sim 0.4$

to $z \sim 4.5$ and found a best fit:

$$\psi(z) = 0.015 \cdot \frac{(1+z)^a}{1+[(1+z)/2.9]^b} \ \mathrm{M}_\odot \ \mathrm{yr}^{-1} \ \mathrm{Mpc}^{-3} \tag{7.1}$$

this functional form is essentially the same as the one presented by Madau & Dickinson (2014) but a and b equal to 3.0 and 3.7 instead of 2.7 and 5.6. Despite the fact that the estimate of Asada & Ohta (2022) at $z \sim 7.8$ was not considered in the fit, the extrapolation fits excellently with the upper limit reported by them.

Our SFR estimates, in particular our SFRD estimates, depend on the corrections done to account for the effects of dust. We investigate how to propagate small differences in dust correction to the results of our SFRD estimates. Using the extinction values given by the SED fitting, instead of using the Meurer et al. (1999b) relation (see Section 6.1), we obtain a consistent estimation that is 1.14× higher as shows Figure 7.5. This trend is the same found by Asada et al. (2021). The final estimate is not very sensitive to our choice between these two estimates of dust the correction.

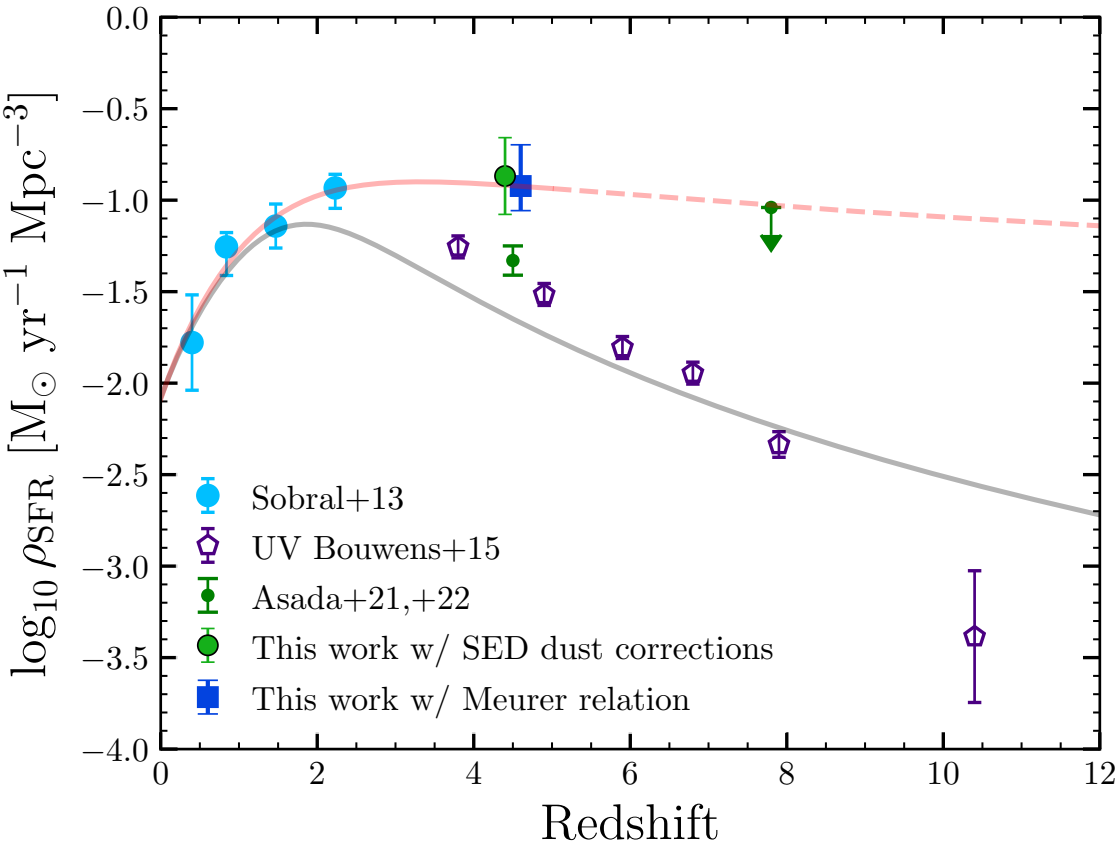

Figure 7.5: Cosmic evolution of the Star Formation Rate Density (SFRD) with the luminosities corrected by dust from the extinction derived by CIGALE instead of the fiducial result presented previously, based on the (Meurer et al. 1999a) relation. This is equivalent to Figure 6.5 but with the alternative dust corrections. The final result does not depend strongly on the choice between these two dust corrections.

Chapter 8

Summary and Conclusions

In this thesis, we investigate the Hα emission in 1299 LBG selected galaxies at $z \sim 4.5$. We have estimated Hα from the excess flux in the photometry at [3.6] μm compared to the best-fit SEDs, which was obtained with CIGALE (Boquien et al. 2019). We have used unique data represented by the deepest *Spitzer*/IRAC imaging available at [3.6] and [4.5] over the GOODS fields from the GOODS Re-ionization Era wide-Area Treasury from Spitzer (GREATS) program (Stefanon et al. 2021).

We proposed an alternative method to estimate the Hα flux, which is fully empirically based and is independent of the choice of stellar population models, that produces very consistent results as Figure 4.4 shows. While for our fiducial estimates we have run CIGALE to model the stellar continuum only, excluding the [3.6] band that may include significant nebular emission line contribution, the code also has the option to include nebular emission in the SED fitting. We have run a separate model that includes nebular emission lines and fit the SEDs including all bands. From here, we read out directly the $F_{\mathrm{H}\alpha}$ from the best fits. We find that the Hα fluxes estimated this way are comparable to the more standard method with the SED fitting adopted in the rest of the paper (but slightly biased to higher values as Figure 4.4.1 shows).

We have used our estimates of the Hα flux to estimate rest-frame EW(Hα) and the Hα luminosity function. We have also applied dust corrections based on the Meurer et al. (1999a) relation and the dust attenuation curve by Calzetti et al. (2000). Combined with standard relations (Kennicutt 1998a) we have made estimates of the SFR(Hα) and the SFR LF. We have integrated the SFR function to calculate the star formation rate density at $z > 4$ as estimated from Hα. Our main findings and conclusions are the following:

1. The rest-frame EW of Hα evolves with redshift as Figure 1.3 shows, having higher values at higher redshift. Our estimate of the EW(Hα) at $z \sim 4.5$ is in between those presented by Fumagalli et al. (2012) and the ones by Mármol-Queraltó et al. (2016). Given the uncertainties, our estimate is consistent with both previous estimates. We also find a tentative correlation such that lower-mass galaxies have higher EW(Hα).

2. The Hα Luminosity Function evolves, in terms of Schechter parameterizations shown in Figure 5.2, with redshift showing a decreasing normalization, Φ^*, from $z = 0.84$ to 4.5 by a factor ~ 14. Meanwhile, L^* increases with redshift from the local Universe to high-z, and while our bright end is not very well constrained, it shows an excess of bright Hα emitters compared to the LF at $z \sim 2$. The faint-end slope α shows no significant evidence of any changes.

3. We have estimated both the $\mathrm{SFR_{H\alpha}}$ and the $\mathrm{SFR_{UV}}$ using standard conversion factors (Kennicutt 1998a). As Figure 7.4 shows, we find that galaxies with $\log(\mathrm{SFR(UV)}) < 1.5$ tend to have a higher SFR(Hα) compared to SFR(UV). The opposite is also true for the higher SFRs. While this may be a sign of increased burstiness among the lower SFR galaxies (also the lower stellar masses), this could also show a difference in the typical SFH of galaxies as a function of mass, with lower mass galaxies having more rising SFHs, and higher mass galaxies having SFHs that are declining at later times.

4. The CSFRD derived from Hα luminosity tends to be systematically elevated compared to the CSFRD estimated from the rest-frame UV, as Figure 6.5 illustrates. This is true at $z < 2$ based on the results by Sobral et al. (2013) compared with the curve proposed by Madau & Dickinson (2014) (mainly based on UV and IR measurements), but the difference becomes more significant at higher redshift. Also, small differences in dust corrections demonstrated by Figure 7.5 do not show a significant impact on the value of the CSFRD.

Despite the lack of Hα spectroscopy at high redshift ($z \lesssim 2.8$), we take advantage of unique data using the deepest mid-IR imaging available from GREATS program (Stefanon et al. 2021) and SED fitting techniques to estimate the Hα flux of galaxies at $z \sim 4.5$. This thesis contributes to the existing knowledge of the Hα LF at lower redshift ($z \lesssim 3$) by providing new constraints at high redshift ($z \sim 4.5$) for the first time. Since this study was limited in S/N, it was not possible to estimate Hα for galaxies $\mathrm{SFR(H\alpha)} \lesssim 6\ \mathrm{M_\odot yr^{-1}}$. However, our results offer valuable insights into novel measurements of the star formation rate and the star formation rate density based on Hα at $z \sim 4.5$, almost free of significant dust attenuation issues and in advance of future Hα spectroscopic surveys.

The James Webb Space Telescope (JWST) will provide a great opportunity to explore high redshift galaxies. The observatory have four instruments: a near-infrared camera, a near-infrared multi-object spectrograph, and a tunable filter imager that covers the wavelength range $0.6 < \lambda < 5.0$ μm, while the mid-infrared instrument can do both imaging and spectroscopy from $5.0 < \lambda < 29$ μm. Thus, it will significantly improve the measurements of Hα in fainter systems and will also extend their study to higher redshift ($z \gtrsim 4$) with accuracy never before achieved. This would be a fruitful area for further work, not only to estimate the Hα LF but also to validate the methods used in this work.

The present work has been already submitted to ApJ.

Bibliography

Aihara, H., Armstrong, R., Bickerton, S., et al. 2018, Publications of the Astronomical Society of Japan, 70, S8

Anders, P. & Fritze-v. Alvensleben, U. 2003, Astronomy and Astrophysics, 401, 1063

Arnouts, S., Schiminovich, D., Ilbert, O., et al. 2005, The Astrophysical Journal, 619, L43

Asada, Y. & Ohta, K. 2022, The Astrophysical Journal, 924, 71

Asada, Y., Ohta, K., & Maeda, F. 2021, The Astrophysical Journal, 915, 47

Astier, P., Guy, J., Regnault, N., et al. 2005

Atek, H., Furtak, L. J., Oesch, P., et al. 2022, Monthly Notices of the Royal Astronomical Society

Avni, Y. & Bahcall, J. N. 1980, The Astrophysical Journal, 235, 694

Balestra, I., Mainieri, V., Popesso, P., et al. 2010, Astronomy and Astrophysics, 512, A12

Beckwith, S. V. W., Stiavelli, M., Koekemoer, A. M., et al. 2006, The Astronomical Journal, 132, 1729

Blanton, M. R., Hogg, D. W., Bahcall, N. A., et al. 2003, The Astrophysical Journal, 592, 819

Boquien, M., Buat, V., & Perret, V. 2014, A&A, 571, A72

Boquien, M., Burgarella, D., Roehlly, Y., et al. 2019, Astronomy and Astrophysics, 622, A103

Bouwens, R., González-López, J., Aravena, M., et al. 2020, ApJ, 902, 112

Bouwens, R. J., Illingworth, G. D., Blakeslee, J. P., Broadhurst, T. J., & Franx, M. 2004, The Astrophysical Journal, 611, L1

Bouwens, R. J., Illingworth, G. D., Blakeslee, J. P., & Franx, M. 2006, ApJ, 653, 53

Bouwens, R. J., Illingworth, G. D., Franx, M., et al. 2009, The Astrophysical Journal, 705, 936

Bouwens, R. J., Illingworth, G. D., Franx, M., & Ford, H. 2007, The Astrophysical Journal, 670, 928

Bouwens, R. J., Illingworth, G. D., Oesch, P. A., et al. 2010, The Astrophysical Journal, 709,

L133

Bouwens, R. J., Illingworth, G. D., Oesch, P. A., et al. 2015, The Astrophysical Journal, 803, 34

Bouwens, R. J., Oesch, P. A., Stefanon, M., et al. 2021, AJ, 162, 47

Bouwens, R. J., Smit, R., Labbé, I., et al. 2016, ApJ, 831, 176

Brammer, G. B., van Dokkum, P. G., Franx, M., et al. 2012, The Astrophysical Journal Supplement Series, 200, 13

Bruzual, G. & Charlot, S. 2003, Monthly Notices of the Royal Astronomical Society, 344, 1000

Bunker, A. J., Stanway, E. R., Ellis, R. S., & McMahon, R. G. 2004, Monthly Notices of the Royal Astronomical Society, 355, 374

Calzetti, D. 1997, The Astronomical Journal, 113, 162

Calzetti, D., Armus, L., Bohlin, R. C., et al. 2000, The Astrophysical Journal, 533, 682

Caputi, K. I., Deshmukh, S., Ashby, M. L. N., et al. 2017, arXiv:1705.06179 [astro-ph] [[arXiv]1705.06179]

Caputi, K. I., Lagache, G., Yan, L., et al. 2007, The Astrophysical Journal, 660, 97

Cardelli, J. A., Clayton, G. C., & Mathis, J. S. 1989, The Astrophysical Journal, 345, 245

Chabrier, G. 2003, Publications of the Astronomical Society of the Pacific, 115, 763

Coughlin, A., Rhoads, J. E., Malhotra, S., et al. 2018, ApJ, 858, 96

Crain, R. A., Schaye, J., Bower, R. G., et al. 2015, Monthly Notices of the Royal Astronomical Society, 450, 1937

Daddi, E., Cimatti, A., Renzini, A., et al. 2004, The Astrophysical Journal, 617, 746

Damen, M., Labbé, I., Franx, M., et al. 2009, The Astrophysical Journal, 690, 937

Davé, R., Anglés-Alcázar, D., Narayanan, D., et al. 2019, Monthly Notices of the Royal Astronomical Society, 486, 2827

Davé, R., Oppenheimer, B. D., & Finlator, K. 2011, Monthly Notices of the Royal Astronomical Society, 415, 11

Davé, R., Rafieferantsoa, M. H., Thompson, R. J., & Hopkins, P. F. 2017, Monthly Notices of the Royal Astronomical Society, 467, 115

Davies, L. J. M., Driver, S. P., Robotham, A. S. G., et al. 2016, Monthly Notices of the Royal Astronomical Society, 461, 458

Davies, L. J. M., Huynh, M. T., Hopkins, A. M., et al. 2017, Monthly Notices of the Royal Astronomical Society, 466, 2312

De Barros, S., Oesch, P. A., Labbé, I., et al. 2019, Monthly Notices of the Royal Astronomical

Society, 489, 2355

Dickinson, M. 1998, 219

Dickinson, M. 2000, 358, 2001

Emami, N., Siana, B., Weisz, D. R., et al. 2019, ApJ, 881, 71

Erb, D. K., Steidel, C. C., Shapley, A. E., et al. 2006, ApJ, 647, 128

Eyles, L. P., Bunker, A. J., Stanway, E. R., et al. 2005, Monthly Notices of the Royal Astronomical Society, 364, 443

Faisst, A. L., Capak, P. L., Emami, N., Tacchella, S., & Larson, K. L. 2019, The Astrophysical Journal, 884, 133

Faisst, A. L., Capak, P. L., Yan, L., et al. 2017, The Astrophysical Journal, 847, 21

Finkelstein, S. L., Papovich, C., Salmon, B., et al. 2012, ApJ, 756, 164

Fioc, M. & Rocca-Volmerange, B. 2019, arXiv:1902.02198 [astro-ph] [[arXiv]1902.02198]

Fontanot, F., Cristiani, S., Santini, P., et al. 2012, Monthly Notices of the Royal Astronomical Society, 421, 241

Ford, H. C., Clampin, M., Hartig, G. F., et al. 2003, 4854, 81

Förster Schreiber, N. M., Genzel, R., Bouché, N., et al. 2009, The Astrophysical Journal, 706, 1364

Franx, M., Labbé, I., Rudnick, G., et al. 2003, ApJ, 587, L79

Fumagalli, M., Labbé, I., Patel, S. G., et al. 2014, The Astrophysical Journal, 796, 35

Fumagalli, M., Patel, S. G., Franx, M., et al. 2012, The Astrophysical Journal Letters, 757, L22

García, L. A., Tescari, E., Ryan-Weber, E. V., & Wyithe, J. S. B. 2017, Monthly Notices of the Royal Astronomical Society, 470, 2494

Geach, J. E., Smail, I., Best, P. N., et al. 2008, Monthly Notices of the Royal Astronomical Society, 388, 1473

Giavalisco, M. 2002, Annu. Rev. Astron. Astrophys., 40, 579

Giavalisco, M., Ferguson, H. C., Koekemoer, A. M., et al. 2004, The Astrophysical Journal, 600, L93

González, V., Bouwens, R. J., Labbé, I., et al. 2012, The Astrophysical Journal, 755, 148

González, V., Labbé, I., Bouwens, R. J., et al. 2011, The Astrophysical Journal, 735, L34

González, V., Labbé, I., Bouwens, R. J., et al. 2010, ApJ, 713, 115

Gordon, K. D., Clayton, G. C., Misselt, K. A., Landolt, A. U., & Wolff, M. J. 2003, The Astrophysical Journal, 594, 279

Grogin, N. A., Kocevski, D. D., Faber, S. M., et al. 2011, ApJS, 197, 35

Gruppioni, C., Calura, F., Pozzi, F., et al. 2015, Monthly Notices of the Royal Astronomical Society, 451, 3419

Guo, Y., Giavalisco, M., Cassata, P., et al. 2011, ApJ, 735, 18

Guo, Y., Rafelski, M., Faber, S. M., et al. 2016, The Astrophysical Journal, 833, 37

Hanish, D. J., Meurer, G. R., Ferguson, H. C., et al. 2006, The Astrophysical Journal, 649, 150

Hasinger, G., Capak, P., Salvato, M., et al. 2018, ApJ, 858, 77

Hayes, M., Schaerer, D., & Östlin, G. 2010, Astronomy and Astrophysics, 509, L5

Herenz, E. C., Urrutia, T., Wisotzki, L., et al. 2017, Astronomy and Astrophysics, 606, A12

Hogg, D. W., Bovy, J., & Lang, D. 2010, Data Analysis Recipes: Fitting a Model to Data

Illingworth, G. D., Magee, D., Oesch, P. A., et al. 2013, The Astrophysical Journal Supplement Series, 209, 6

Jarvis, M. J., Bonfield, D. G., Bruce, V. A., et al. 2013, Monthly Notices of the Royal Astronomical Society, 428, 1281

Jiang, L., Kashikawa, N., Wang, S., et al. 2021, Nature Astronomy, 5, 256

Kashikawa, N., Shimasaku, K., Matsuda, Y., et al. 2011, ApJ, 734, 119

Katsianis, A., Blanc, G., Lagos, C. P., et al. 2017a, Monthly Notices of the Royal Astronomical Society, 472, 919

Katsianis, A., Tescari, E., Blanc, G., & Sargent, M. 2017b, Monthly Notices of the Royal Astronomical Society, 464, 4977

Katsianis, A., Tescari, E., & Wyithe, J. S. B. 2015, Monthly Notices of the Royal Astronomical Society, 448, 3001

Kennicutt, J. 1998a, Annu. Rev. Astron. Astrophys., 36, 189

Kennicutt, R. C. & Evans, N. J. 2012, Annual Review of Astronomy and Astrophysics, vol. 50, p.531-608, 50, 531

Kennicutt, Jr., R. C. 1998b, The Astrophysical Journal, 498, 541

Khusanova, Y., Bethermin, M., Le Fèvre, O., et al. 2021, A&A, 649, A152

Koekemoer, A. M., Faber, S. M., Ferguson, H. C., et al. 2011, ApJS, 197, 36

Kriek, M., Shapley, A. E., Reddy, N. A., et al. 2015, The Astrophysical Journal Supplement Series, 218, 15

Kroupa, P. 2001, Monthly Notices of the Royal Astronomical Society, 322, 231

Labbé, I., González, V., Bouwens, R. J., et al. 2010, ApJL, 716, L103

Labbé, I., Oesch, P. A., Illingworth, G. D., et al. 2015, ApJS, 221, 23

Le Floc'h, E., Papovich, C., Dole, H., et al. 2005, The Astrophysical Journal, 632, 169

Lehnert, M. D. & Bremer, M. 2003, The Astrophysical Journal, 593, 630

Lilly, S. J., Le Fevre, O., Hammer, F., & Crampton, D. 1996, The Astrophysical Journal Letters, 460, L1

Lorenzoni, S., Bunker, A. J., Wilkins, S. M., et al. 2011, Monthly Notices of the Royal Astronomical Society, 414, 1455

Ly, C., Lee, J. C., Dale, D. A., et al. 2011, ApJ, 726, 109

Ly, C., Malkan, M. A., Rigby, J. R., & Nagao, T. 2016, The Astrophysical Journal, 828, 67

Madau, P. & Dickinson, M. 2014, Annual Review of Astronomy and Astrophysics, 52, 415

Madau, P., Ferguson, H. C., Dickinson, M. E., et al. 1996, Monthly Notices of the Royal Astronomical Society, 283, 1388

Marchesini, D., van Dokkum, P., Quadri, R., et al. 2007, The Astrophysical Journal, 656, 42

Mármol-Queraltó, E., McLure, R. J., Cullen, F., et al. 2016, Monthly Notices of the Royal Astronomical Society, 460, 3587

Meurer, G. R., Heckman, T. M., & Calzetti, D. 1999a, The Astrophysical Journal, 521, 64

Meurer, G. R., Heckman, T. M., & Calzetti, D. 1999b, The Astrophysical Journal, 521, 64

Momcheva, I. G., Brammer, G. B., van Dokkum, P. G., et al. 2016, ApJS, 225, 27

Moutard, T., Sawicki, M., Arnouts, S., et al. 2020, Monthly Notices of the Royal Astronomical Society, 494, 1894

Oesch, P. A., Bouwens, R. J., Illingworth, G. D., et al. 2010, The Astrophysical Journal, 709, L16

Oesch, P. A., Bouwens, R. J., Illingworth, G. D., Labbé, I., & Stefanon, M. 2018a, ApJ, 855, 105

Oesch, P. A., Bouwens, R. J., Illingworth, G. D., Labbé, I., & Stefanon, M. 2018b, The Astrophysical Journal, 855, 105

Oesch, P. A., Brammer, G., van Dokkum, P. G., et al. 2016, ApJ, 819, 129

Oesch, P. A., van Dokkum, P. G., Illingworth, G. D., et al. 2015, ApJL, 804, L30

Oke, J. B. & Gunn, J. E. 1983, The Astrophysical Journal, 266, 713

Ono, Y., Ouchi, M., Harikane, Y., et al. 2018, Publications of the Astronomical Society of Japan, 70, S10

Ouchi, M., Shimasaku, K., Okamura, S., et al. 2004, The Astrophysical Journal, 611, 660

Oyarzún, G. A., Blanc, G. A., González, V., Mateo, M., & Bailey, III, J. I. 2017, The Astrophysical Journal, 843, 133

Oyarzún, G. A., Blanc, G. A., González, V., et al. 2016, The Astrophysical Journal, 821, L14

Partridge, R. B. & Peebles, P. J. E. 1967, The Astrophysical Journal, 147, 868

Peng, Y.-j., Lilly, S. J., Kovač, K., et al. 2010, The Astrophysical Journal, 721, 193

Pillepich, A., Springel, V., Nelson, D., et al. 2018, Monthly Notices of the Royal Astronomical Society, 473, 4077

Rasappu, N., Smit, R., Labbé, I., et al. 2016, Monthly Notices of the Royal Astronomical Society, 461, 3886

Reddy, N. A., Erb, D. K., Pettini, M., Steidel, C. C., & Shapley, A. E. 2010, ApJ, 712, 1070

Reddy, N. A., Steidel, C. C., Pettini, M., et al. 2008, The Astrophysical Journal Supplement Series, 175, 48

Salpeter, E. E. 1955, The Astrophysical Journal, 121, 161

Scalo, J. M. 1986, Fundamentals of Cosmic Physics, 11, 1

Scannapieco, E., Silk, J., & Bouwens, R. 2005, The Astrophysical Journal, 635, L13

Schaerer, D. & de Barros, S. 2009, A&A, 502, 423

Schaye, J., Crain, R. A., Bower, R. G., et al. 2015, Monthly Notices of the Royal Astronomical Society, 446, 521

Schechter, P. 1976, The Astrophysical Journal, 203, 297

Schmidt, M. 1968, The Astrophysical Journal, 151, 393

Scoville, N., Aussel, H., Brusa, M., et al. 2007, ApJS, 172, 1

Shapley, A. E. 2011, Annual Review of Astronomy and Astrophysics, 49, 525

Shapley, A. E., Steidel, C. C., Adelberger, K. L., et al. 2001, The Astrophysical Journal, 562, 95

Shim, H., Chary, R.-R., Dickinson, M., et al. 2011, The Astrophysical Journal, 738, 69

Shivaei, I., Reddy, N., Rieke, G., et al. 2020, ApJ, 899, 117

Shivaei, I., Reddy, N. A., Steidel, C. C., & Shapley, A. E. 2015, The Astrophysical Journal, 804, 149

Skelton, R. E., Whitaker, K. E., Momcheva, I. G., et al. 2014, The Astrophysical Journal Supplement Series, 214, 24

Smit, R., Bouwens, R. J., Franx, M., et al. 2012, The Astrophysical Journal, 756, 14

Smit, R., Bouwens, R. J., Labbé, I., et al. 2016, The Astrophysical Journal, 833, 254

Sobral, D., Smail, I., Best, P. N., et al. 2013, Monthly Notices of the Royal Astronomical Society, 428, 1128

Stark, D. P., Ellis, R. S., Bunker, A., et al. 2009, ApJ, 697, 1493

Stark, D. P., Schenker, M. A., Ellis, R., et al. 2013, ApJ, 763, 129

Stefanon, M., Bouwens, R. J., Illingworth, G. D., et al. 2022 [[arXiv]2204.02986]

Stefanon, M., Labbé, I., Oesch, P. A., et al. 2021 [[arXiv]2110.06226]

Steidel, C. C., Adelberger, K. L., Giavalisco, M., Dickinson, M., & Pettini, M. 1999, The Astrophysical Journal, 519, 1

Steidel, C. C., Giavalisco, M., Pettini, M., Dickinson, M., & Adelberger, K. L. 1996, The Astrophysical Journal, 462, L17

Stroe, A. & Sobral, D. 2015, Monthly Notices of the Royal Astronomical Society, 453, 242

Tacchella, S., Bose, S., Conroy, C., Eisenstein, D. J., & Johnson, B. D. 2018, The Astrophysical Journal, 868, 92

Tescari, E., Katsianis, A., Wyithe, J. S. B., et al. 2014, Monthly Notices of the Royal Astronomical Society, 438, 3490

Trenti, M., Bradley, L. D., Stiavelli, M., et al. 2011, ApJL, 727, L39

Utomo, D., Kriek, M., Labbé, I., Conroy, C., & Fumagalli, M. 2014, ApJL, 783, L30

van Dokkum, P., Brammer, G., Momcheva, I., Skelton, R. E., & Whitaker, K. E. 2013, arXiv:1305.2140 [astro-ph] [[arXiv]1305.2140]

van Dokkum, P. G., Brammer, G., Fumagalli, M., et al. 2011, The Astrophysical Journal, 743, L15

Vanzella, E., Cristiani, S., Dickinson, M., et al. 2008, A&A, 478, 83

Vanzella, E., Cristiani, S., Dickinson, M., et al. 2005, A&A, 434, 53

Vanzella, E., Cristiani, S., Dickinson, M., et al. 2006, A&A, 454, 423

Vanzella, E., Giavalisco, M., Dickinson, M., et al. 2009, ApJ, 695, 1163

Verma, A., Lehnert, M. D., Förster Schreiber, N. M., Bremer, M. N., & Douglas, L. 2007, Monthly Notices of the Royal Astronomical Society, 377, 1024

Vogelsberger, M., Genel, S., Sijacki, D., et al. 2013, Monthly Notices of the Royal Astronomical Society, 436, 3031

Weisz, D. R., Johnson, B. D., Johnson, L. C., et al. 2012, The Astrophysical Journal, 744, 44

Williams, R. E., Blacker, B., Dickinson, M., et al. 1996, The Astronomical Journal, 112, 1335

Windhorst, R. A., Cohen, S. H., Hathi, N. P., et al. 2011, ApJS, 193, 27

Wyder, T. K., Treyer, M. A., Milliard, B., et al. 2005, The Astrophysical Journal, 619, L15

Yabe, K., Ohta, K., Iwata, I., et al. 2009, ApJ, 693, 507

Yan, H. & Windhorst, R. A. 2004, The Astrophysical Journal, 612, L93